

Ozone Production in the Atmosphere Simulation Chamber SAPHIR

Cornelia Anna Richter



Forschungszentrum Jülich GmbH Institut für Chemie und Dynamik der Geosphäre (ICG) Troposphäre (ICG-2)

Ozone Production in the Atmosphere Simulation Chamber SAPHIR

Cornelia Anna Richter

Bibliographic information published by the Deutsche Nationalbibliothek. The Deutsche Nationalbibliothek lists this publication in the Deutsche Nationalbibliografie; detailed bibliographic data are available in the Internet at http://dnb.d-nb.de.

Publisher Forschungszentrum Jülich GmbH

and Distributor: Zentralbibliothek, Verlag

D-52425 Jülich

phone:+49 2461 61-5368 · fax:+49 2461 61-6103

e-mail: zb-publikation@fz-juelich.de Internet: http://www.fz-juelich.de/zb

Cover Design: Grafische Medien, Forschungszentrum Jülich GmbH

Printer: Grafische Medien, Forschungszentrum Jülich GmbH

Copyright: Forschungszentrum Jülich 2008

Cover picture: Dr. Hans-Peter Dorn. Forschungszentrum Jülich GmbH.

Institut für Chemie und Dynamik der Geosphäre (ICG),

Troposphäre (ICG-2)

Schriften des Forschungszentrums Jülich Reihe Energie & Umwelt / Energy & Environment Band / Volume 2

D 38 (Diss., Köln, Univ., 2007)

ISSN 1866-1793 ISBN 978-3-89336-513-5

The complete volume is freely available on the Internet on the Jülicher Open Access Server (JUWEL) at http://www.fz-juelich.de/zb/juwel

Neither this book nor any part may be reproduced or transmitted in any form or by any means, electronic or mechanical, including photocopying, microfilming, and recording, or by any information storage and retrieval system, without permission in writing from the publisher.

Zusammenfassung

Troposphärisches Ozon ist in hohen Konzentrationen schädlich für Mensch und Umwelt. Zudem ist es ein Treibhausgas, dessen Erhöhung durch anthropogene Emissionen der Vorläufersubstanzen zur globalen Erwärmung beiträgt. Für die atmosphärische Chemie ist Ozon entscheidend, da es selbst ein Oxidationsmittel für andere Spurengase und außerdem der Hauptvorläufer für alle anderen oxidierenden Substanzen, z.B. dem äußerst reaktiven OH Radikal, ist.

Wegen dieser umfassenden Bedeutung ist es wichtig, die chemischen Bildungsprozesse des troposphärischen Ozons zu verstehen. Nötige Vorläufer für die photochemische Bildung sind die hauptsächlich anthropogen emittierten Stickoxide $\mathrm{NO_x}$ und die sowohl biogen als auch anthropogen emittierten flüchtigen Kohlenwasserstoffe. Der prinzipielle Ablauf und die allgemeinen Zusammenhänge der photochemischen Ozonproduktion sind inzwischen recht gut verstanden. Im Speziellen bestehen aber durchaus noch große Unsicherheiten, die weiter erforscht werden müssen, um eine fundierte Vorhersage auf kurzen und langen Zeitskalen bezüglich der zu erwartenden Ozonwerte, beispielsweise für eine Warnung der Bevölkerung oder zur Klimaforschung, machen zu können.

In der Atmosphären Simulationskammer SAPHIR können chemische Prozesse der Tropsphäre frei von physikalischen Einflüssen, also Transport- oder Mischprozessen und unbekannten Quellen und Senken, unter Umgebungsbedingungen für Spurengaskonzentrationen, Beleuchtungsverhältnissen, Druck und Temperatur durchgeführt werden. Um die komplexen, die Spurengaskonzentrationen betreffenden Prozesse in der Atmosphäre zu verstehen, sind aber auch Feldmessungen unabdingbar. Für deren Interpretation müssen mittels Modellberechnungen die chemischen Umwandlungen von den physikalisch bedingten Änderungen unterschieden werden. Der Test solcher Modellansätze ist nur unter kontrollierten physikalischen Bedingungen möglich, wie sie die SAPHIR Kammer zur Verfügung stellt.

In der vorliegenden Arbeit wurden drei verschiedene Ansätze zur Vorhersage der photochemischen Ozonproduktion gegenüber SAPHIR Kammerexperimenten getestet, welche sich stark in Bezug auf die benötigten Eingangsgrößen und den rechnerischen Aufwand unterscheiden. Zunächst wurden die Vorhersagen kompletter zeitabhängiger Modellläufe auf Basis des 'Master Chemical Mechanism', einem auf dem aktuellen Wissensstand basierendem Chemiemechanismus, zum ersten Mal in atmosphärisch relevanten Spurengaskonzentrationen untersucht. Diese Modellläufe benötigen wenige Eingangsgrößen und erfordern einen hohen numerischen Aufwand. Der neu entwickelte 'Erster Abbau Schritt' Ansatz hingegen benötigt viele gemessene Eingangsgrößen, um dann mit Hilfe einfacher Arithmetik die Ozonproduktion zu bestimmen. Einen

weiteren neuen, noch einfacheren Ansatz stellt die dritte Methode dar, die basierend auf gemessenen OH Konzentrationen und OH Lebensdauern eine Abschätzung der Ozonproduktion erlaubt.

Als Ausgangskohlenwasserstoff der SAPHIR Experimente wurden Isopren und dessen Abbauprodukte Methacrolein und Methyl Vinyl Keton verwendet. Die Wahl fiel unter anderem deshalb auf das von der Vegetation emittierte Isopren, da es global gesehen der mengenmäßig meistemittierte und daher in vielen Regionen der dominierende Vorläuferkohlenwasserstoff für die Ozonproduktion ist.

Im zweiten Teil der Arbeit wurde der Methacrolein Abbau eingehender untersucht. Dabei zeigten auf dem Master Chemical Mechanism basierende Modellrechnungen starke Abweichungen zwischen gemessenem und modelliertem NO_{x} . Diese Diskrepanzen konnten teilweise erklärt und auf Fehler im Master Chemical Mechanism zurückgeführt werden.

Abstract

Tropospheric ozone in high concentrations is harmful for mankind and the environment as a whole. As it is a greenhouse gas, its rising due to anthropogenic emissions of the precursor species contributes to global warming. By being the precursor specie for all oxidizing agents in the atmosphere, e.g. the highly reactive OH radical, and being an oxidizing agent itself, ozone is very important in atmospheric chemistry.

Due to this importance, a sound understanding of the chemical ozone production processes is needed. The necessary precursors for the photochemical production are the mainly anthropogenic nitrogen oxides $\mathrm{NO_x}$ and the both anthropogenic and biogenic volatile organic compounds. In principle, the processes are fairly understood. In details huge uncertainties still exist. These have to be examined further to allow for well-founded predictions of short and long term ozone concentrations, e.g. to early warn the population off injurious values to come or for the use in climate change modelling.

In the atmosphere simulation chamber SAPHIR chemical processes of the troposphere can be examined nearly without physical caused changes, like transport, mixing, or unknown sources and sinks of trace constituents. Ambient conditions concerning trace gas concentrations, temperature, pressure and lighting conditions characterize the SAPHIR experiments. To understand the complex processes influencing trace gas concentrations in nature, field experiments are obligatory. For the interpretation of measured field data model calculations are needed to distinguish between chemical and physical influences. The test of these models is only feasible under the physically controlled conditions inside the SAPHIR chamber.

In this thesis, three different approaches, which strongly vary concerning their needed (measured) input and the computational effort, for the prediction of the photochemical ozone production were tested against SAPHIR chamber experiments. First of all model runs on the basis of the Master Chemical Mechanism, which compiles the state of the art knowledge in atmospheric chemistry in one mechanism, were tested at ambient trace gas concentrations for the first time. These model runs only need few measured input but a high computational effort. The newly developed First Degradation Step approach in contrast needs a lot of measured input, which then is combined by fundamental arithmetic to calculate the ozone production. The third, also new approach tested is an even simpler method, which estimates the ozone production by a simple combination of measured OH concentrations and OH lifetimes.

As the initial organic compound for the SAPHIR experiments isoprene and its degradation products methacrolein and methyl vinyl ketone were selected, as on a global scale isoprene is the mostly emitted volatile organic compound, which dominates photochemical ozone production in many regions.

In the second part of this thesis special attention was directed on the methacrolein degradation. The Master Chemical Mechanism model showed strong deviations concerning the measured NO_{x} concentrations. These discrepancies could partly be explained and were traced back to errors of the Master Chemical Mechanism.

Contents

1	Intro	oduction 1
	1.1	Ozone
	1.2	Ozone Precursor Species 6
	1.3	Isoprene
	1.4	Peroxyacyl Nitrates
	1.5	Chemical Weather Forecast
	1.6	Chamber Experiments
	1.7	Aim of this Thesis
2	The	orv 13
	2.1	Gas Phase Chemistry
		2.1.1 Tropospheric Ozone Production
		2.1.2 Chemical Regimes
	2.2	Chemical Mechanisms
	2.3	Numerical Solving
_	_	
3		erimentals 25
	3.1	The SAPHIR Chamber
		3.1.1 Dilution
		3.1.2 HONO Source
		3.1.3 HCHO Source
		3.1.4 Background Reactivity
		3.1.5 Other Sources
		3.1.6 Deposition at the Walls
	3.2	Instrumentation
		3.2.1 Ozone Measurements
		3.2.2 Reactive Species
		3.2.3 Volatile Organic Compounds 41
		3.2.4 NO _y Species
		3.2.5 Photolysis Frequencies
		3.2.6 Meteorological Conditions
4	Ozo	ne Production Due to Isoprene Degradation 47
	4.1	Fully Time Dependent MCM Model Runs 49
		4.1.1 Results
		4.1.2 Discussion
	4.2	First Degradation Step Approach

Contents

		4.2.1 Used Method	59
		4.2.2 Results	63
		4.2.3 Discussion	67
	4.3	OH Lifetime	69
		4.3.1 Idea	70
		4.3.2 Used Method	71
		4.3.3 Results and Discussion	74
	4.4	Conclusion	
5	Met	hacrolein Degradation Studies	81
	5.1	OH Induced MACR Degradation	81
		5.1.1 Used MCM Model	
		5.1.2 Observations	85
		5.1.3 Results	
	5.2	Photolysis and Ozonolysis of MACR	
		5.2.1 Used Models	
		5.2.2 Results	
	5.3	NO ₃ Induced MACR Degradation	
		5.3.1 Used Models	
		5.3.2 Results	
	5.4	Conclusion	
6	Rés	umé and Outlook	103
Α	Use	d Gas Phase Chemistry Mechanisms	107
	A.1	Function Definitions	107
	A.2	Default Settings and MCM Constants	108
	A.3	Inorganic Section	109
	A.4	MCM Isoprene Subset	110
		A.4.1 Chamber-Features in the Isoprene MCM Model	
В	Tab	les of Analyzed Experiments	127
C	Stat	tistics	129
_			

List of Figures

1.1 1.2 1.3	Picture of ozone injury of a Salix caprea leaf	4 7 11
2.1 2.2 2.3 2.4	Ozone null cycle	14 18 19 21
3.1 3.2 3.3 3.4	Picture of the SAPHIR chamber	25 31 34 38
4.1 4.2 4.3	O_x fitting lines at GC sampling times Fully time dependent isoprene model run Correlations of the net O_x productions between measurements	49 53
4.4	and fully time dependent model runs	54
4.5	Sep 2005 experiments	56 60
4.6 4.7	"Decision tree" for the determination of amplifying factors Time series of fitted versus first-degradation-step approach de-	62
4.8	rived O_x production on 15th of May 2006	65
4.9	periments between Sep 2005 and June 2006	66 68
4.10	Time series of defining parameters for the integrated amplifying factor	73
4.11	Correlation between the net O_x production and the OH loss rate for all experiments	74
	Averaged OH loss rate times amplifying factor over mean net O_x production	75
	Roundoff errors occurring in F_{OH} calculation	76
4.14	Dependencies of the integrated amplifying factor Fox	77

5.1	NO_x discrepancy at the OH induced MACR degradation	83
5.2	Comparison of the NO _x time series for different MCM model	
	parameters and the NO_x measurements	84
5.3	Rate coefficients used by the MCM and recommended by IU-	
	PAC for the MACR + OH reaction	87
5.4	Reaction scheme recommended by IUPAC for the $MACR + OH$	
	reaction	89
5.5	'IUPAC' model runs for the OH induced MACR degradation $. $.	91
5.6	PAN and MPAN measurements and model concentrations for	
	OH induced MACR degradation	92
5.7	Reaction scheme of the MACR photolysis 'IUPAC' implemen-	
	tation	94
5.8	Reaction scheme of the MACR ozonolysis	95
5.9	MACR photolysis and ozonolysis experiment on 12th Apr 2007 .	96
5.10	NO ₃ induced MACR degradation scheme implemented in the	
	'IUPAC' model	98
5.11	Nighttime MACR degradation experiments on 13th Nov 2006	
	and 13th Apr 2007	100

List of Tables

1.1 1.2	Selected components of the earth's atmosphere	
3.1 3.2 3.3	Technical specification of the SAPHIR chamber Fitting parameters of the HCHO source's water dependence Overview of the instrumentation at SAPHIR	33
4.1	Measurement vs. model correlation parameters of the net O_x production	52
4.2	Measurement vs. model correlation parameters for VOC measurements	57
5.1	MCM model parameters for the OH induced MACR degradation experiments	86
5.2	'IUPAC' model parameters for the OH induced MACR degradation experiments	90
5.3	Changes in the MCM EASY model to represent the IUPAC recommendation	102
	Analyzed "Standard Experiments"	

List of Abbreviations

cps counts per second

 $h\nu$ Photon, used in chemical reactions as an educt to symbolize

a photolysis

ppb <u>parts per billion</u> $\triangleq 10^{-9}$

ppm parts per million $\hat{=} 10^{-6}$

ppt parts per <u>trillion</u> $\stackrel{.}{=} 10^{-12}$

ACETOL Hydroxyacetone

 $\mathrm{AQM} \ \dots \dots \ \underline{\mathrm{Air} \ \mathrm{Quality} \ \underline{\mathrm{M}}\mathrm{odel}}$

BR Background Reactivity

C5H8 Isoprene

 ${\rm CL} \ \dots \dots {\rm Chemiluminescence}$

CTM Chemistry Transport Model

DOAS Differential Optical Absorption Spectroscopy

FDS First \underline{D} egradation \underline{S} tep

FZJ Forschungszentrum Jülich

GC Gas Chromatography

HCHO Formaldehyde

 HO_x Sum of OH and HO_2

HONO Nitrous acid

ICG Institute for Chemistry and dynamics of the Geosphere

IDL <u>Interactive Data Language</u>

IPCC Intergovernmental Panel on Climate Change

IUPAC International Union of Pure and Applied Chemistry

J Photolysis frequency

JPL Jet Propulsion Laboratory

 k_{Rx} Rate coefficient of reaction Rx

LIF Laser Induced Fluorescence

LoD Limit of Detection

M In chemical reactions: third body, normally N_2 or O_2 , which

absorbs excess energy of an intermediate product

M In rate coefficients: number density of the air molecules

 $(\approx 2.7 \cdot 10^{19} cm^{-3} \text{ at T} = 273 \text{K}, p = 1013 \text{hPa})$

MACR Methacrolein

MCM <u>M</u>aster <u>C</u>hemical <u>M</u>echanism

MGLYOX Methylglyoxal

MPAN Methacryloylperoxynitrate

MVK Methyl vinyl ketone

NMHC Non-Methane Hydro Carbon

 ${\rm NMOC} \ \dots \dots \ \underline{{\rm Non-Methane}} \ \underline{{\rm Organic}} \ \underline{{\rm Compounds}}$

 NO_x Sum of NO and NO_2

NO_y Reactive nitrogen

It denotes the sum of $\mathrm{NO_x}$ and its oxidation products. The most important components are NO , $\mathrm{NO_2}$, $\mathrm{HNO_3}$ and aerosol $\mathrm{NO_3}$, PANs and other organic nitrates, $\mathrm{NO_3}$, $\mathrm{N_2O_5}$, HONO ,

and HNO₄.

 O_x Sum of NO_2 and O_3

OVOC Oxygenated Volatile Organic Compound

PAN Peroxyacetylnitrate

PANs Peroxyacyl Nitrates

PPN Peroxypropionic nitric anhydride

RH Relative $\underline{\mathbf{H}}$ umidity

 $SAPHIR \quad \dots \quad \underline{Simulation} \text{ of } \underline{A}tmospheric \\ \underline{PH}otochemistry \\ \underline{In} \text{ a huge } \underline{R}eaction$

chamber

SR Spectral radiometer

UTC Universal time

UV <u>Ultra Violet</u>

 v_{Rx} Velocity (rate) of reaction Rx

 ${\rm VOC} \ \dots \dots \ \underline{{\rm V}} {\rm olatile} \ \underline{{\rm O}} {\rm rganic} \ \underline{{\rm C}} {\rm ompound}$

1 Introduction

Ozone (trioxygen, O₃) was the first trace constituent¹ apart from water vapor discovered by Christian Friedrich Schönbein in 1840 [1]. He named it after the Greek word for smell (ozein). At standard temperature and pressure undiluted ozone is a pale blue gas. Due to its disinfecting properties it was considered a healthy gas [2] and elevated ozone concentrations, although adverse negative effects on human health are known, are still used as an indicator for clean air of climatic spas. Since Schönbein's time a lot of other trace constituents of the earth's atmosphere have been quantified. An overview of some selected air components is given in table 1.1.

The long and short term variations, chemical reactions and other conversion processes of these components became of interest in the 20th century. Triggering events for this new scientific field were the occurrences of photochemical smog, thus smog built by chemical reactions of precursor species during sunlight exposure, in Los Angeles in the 40th of the last century. The explanation of this "Los Angeles-Smog" by Haagen-Smit [3] was an important discovery of this period. Later on the clarification of how the ozone layer develops by Sydney Chapman [4, 5] followed by the research of Gordon Dobson [6] is another noteworthy finding [7, 8].

Although the principal formation of photochemical smog is well understood since that time and technical progress has helped to reduce the emissions of precursor species, it is still of concern in many major cities. Especially during stable high pressure weather conditions and particularly when the geographical position of the cities leads to meteorological inversion effects preventing the air masses to mix with fresh, unpolluted air masses from above. Examples are Los Angeles, London, Mexico City and Beijing. As precursors and ozone as well travel with wind, this can cause even higher ozone levels downwind the emission sources.

Nowadays the role of trace gases is of interest mainly in the context of climate change, as global warming is strongly driven by changes in the atmospheric abundance of trace gases, especially so-called greenhouse gases like carbon dioxide CO₂, methane CH₄, nitrous oxide N₂O and tropospheric ozone. Changes in the atmospheric aerosol load, of solar radiation, and land surface properties are also driving forces. Except for the solar radiation, all of these changes more or less result from human activities like fossil fuel use and land use change.

¹In atmospheric chemistry all components of air with a less occurrence than nitrogen and oxygen are called *trace constituents* or *trace gases*.

Table 1.1: Selected components of the earth's atmosphere (dry air). Given are the names, empirical formulas and the relative abundances. The values are taken from $Zellner\ 1999\ [9]$ except for the values of CO₂, CH₄, and N₂O which are updates taken from the current intergovernmental panel on climate change (IPCC) report [10].

Name		Concentration	
Nitrogen	N_2	78.084 %	
Oxygen	O_2	20.946 %	
(Water vapor	H_2O	up to 7.5 %)	
Argon	Ar	0.934 %	
Carbon dioxide	CO_2	$280ppm^a$ (preindustrial)	
		379ppm (year 2005, rising with 1.9ppm	
		per year between 1995-2005)	
Neon	Ne	18.2 <i>ppm</i>	
Helium	Не	5.24ppm	
Methane	CH_4	$715ppb^b$ (preindustrial)	
		1774 <i>ppb</i> (year 2005)	
Nitrous oxide	N_2O	270ppb(preindustrial)	
		319 <i>ppb</i> (year 2005)	
Carbon monoxide	CO	200ppb northern hemisphere	
		50ppb southern hemisphere	
Ozone	O_3	15-50 <i>ppb</i>	
Nitrogen oxides	$NO + NO_2$	$30ppt^c$ (marine air)	
		300ppt (continental remote sites)	
		5ppb (continental rural)	
Isoprene	C_5H_8	0.6-2.5ppb continental surface air	

^appm stands for parts per million, meaning that the concentration of 1ppm trace gas being such that just one trace gas molecule is in between 10^6 air molecules. bppb stands for parts per billion, one trace gas molecule in between 10^9 air molecules. cppt stands for parts per trillion, one trace gas molecule in between 10^{12} air molecules.

1.1 Ozone

Ozone is one of the key constituents and is used as an indicator substance of photochemical smog. It is no primary but a secondary air pollutant, as it is not directly emitted but built through chemical reactions of precursor species in the presence of UV sunlight. Most of the atmospheric ozone is build and resides in the stratosphere² forming the so-called ozone layer. A small part of the stratospheric ozone overcomes the tropopause and is mixed down into the troposphere. This down mixed stratospheric ozone give rise to a background level of ozone in "clean" remote sites of the planetary boundary layer (PBL)³ of about 15-40 ppb^4 [12, 13], decreasing with closeness to the ground as dry deposition takes place there. These small amounts are enough to initialize a chemical reaction cycle, which can lead to a intense production of more ozone, if the necessary precursors

- nitrogen oxides $(NO_x = NO_2 + NO)$ as a catalyst and
- volatile organic compounds (VOCs) and/or CO

and sunlight are present (c.v. chapter 1.2). The ozone levels reached in photochemical smog episodes exceed the background levels by more than an order of magnitude. The peak concentration reached in Los Angeles during the 50th of the last century was about 580ppb [8]. Early suggestions that these high ground level values just came from mixing down of stratospheric air masses could not explain these high values in contrast to the explanation via photochemical production. This tropospheric photochemical ozone creation mechanism is explained in detail in chapter 2.

As an oxidizing agent in high concentrations ozone affects human health, especially it can perturb lung function, irritates the respiratory system and causes eye irritation ([14, 15]). It harms the flora, see e.g. picture 1.1 of a injured Salix caprea leaf, which is just one picture out of numerous assembled at the Ozone Injury Database ([16]). Reductions of crop yields are also attributed to high ozone levels ([17, 18]), and corrosion of material like rubber or leather.

To ensure effective protection against harmful effects on human health from exposure to ozone and to reduce the adverse effects of ozone on vegetation, ecosystems and the environment as a whole, the European Parliament and the Council of the European Union have adopted a directive in march 2002 which updated an older directive from 1996. Among other things this directive

²The air layer between round 10 to 50km altitude is called *stratosphere*, as the air masses are stratified in temperature and no adiabatic convection takes place. Below, starting at ground level, lies the *troposphere*. The border between troposphere and stratosphere is called *tropogause*. Above the stratosphere the *mesosphere* is located. [11]

³ Planetary boundary layer denotes the lowest part of the troposphere, where turbulent mixing causes rapid fluctuations and turbulence through interactions of the wind field with the surface. The thickness of the PBL depends on many factors, for example surface structure, temperature and wind field, yielding from 50 up to 2000m. The air above is called free troposphere, where the wind blows nearly geostrophic (parallel to the isobars).

⁴Beside ppb (parts per billion) another common unit for the tropospheric concentration of ozone is $\mu g/m^3$. One ppb corresponds to $2\mu g/m^3$ at standard temperature and pressure.



Figure 1.1: Severe red stippling and pigmentation of the upper leaf surface of Salix caprea (picture taken from the 'Ozone Injury Database' [16]).

gives long-term objectives⁵, target values⁶, alert⁷, and information thresholds⁸ for ozone concentrations, quoted in table 1.2. These values are also valid for Germany [20].

Additionally to the harming effects, ozone is the precursor of all oxidizing agents like the hydroxyl radical OH or nitrate radicals NO₃ in the troposphere and is therefore essential for a huge part of the chemical gas phase reactions taking place in the troposphere (q.v. chapter 2).

As mentioned above, tropospheric O_3 is also an important greenhouse gas. The current state of knowledge is, that the elevated tropospheric ozone level due to anthropogenic emissions of the precursor species, cause a radiative

^{5&}quot; long-term objective means an ozone concentration in the ambient air below which, according to current scientific knowledge, direct adverse effects on human health and/or the environment as a whole are unlikely. This objective is to be attained in the long term, save where not achievable through proportionate measures, with the aim of providing effective protection of human health and the environment." [19]

^{6&}quot; target value means a level fixed with the aim, in the long term, of avoiding harmful effects on human health and/or the environment as a whole, to be attained where possible over a given period." [19]

^{7&}quot; alert threshold means a level beyond which there is a risk to human health from brief exposure for the general population and at which immediate steps shall be taken by the Member States" [19]

^{8&}quot; information threshold means a level beyond which there is a risk to human health from brief exposure for particularly sensitive sections of the population and at which up-todate information is necessary." [19]

Table 1.2: Ozone threshold values for the European Union [19].

Target values for the year 2010

	, , , , , , , , , , , , , , , , , , , ,	
Target value for the protection of	Parameter	Target value
protection of		
human health	Maximum daily 8-hour mean	$120\mu g/m^3$ not to be exceeded on more than 25 days per calender year averaged over three years
vegetation	AOT40 ^a , calculated from 1 hour values from May to July	,

Long-term objectives

Long-term objective for the protection of	Parameter	Long-term objective
human health	Maximum daily 8-hour mean within a calender year	$120\mu g/m^3$
vegetation	AOT40, calculated from 1 h values from May to July	$6000\mu g/m^3 \cdot h$

Alert and information threshold

	Parameter	Threshold
Information threshold	1 hour average	$180 \mu g/m^3$
Alert threshold	1 hour average	$240 \mu g/m^3$

 $[^]aAOT40$ (expressed in $(\mu g/m^3 \cdot hours)$ means the sum of the difference between hourly concentrations greater than $80\mu g/m^3$ (= 40 parts per billion) over a given time period.

forcing⁹ of about $0.35\pm_{0.1}^{0.3}Wm^{-2}$ in 2005 compared to pre-industrial conditions defined at 1750. This is nearly a quarter of the net anthropogenic forcing of $1.6\pm_{1.0}^{0.8}Wm^{-2}$ [10]. For expample in the Oporto Metropolitan Area in Portugal Alvim-Ferraz et al. 2006 [2] found, that the ground level ozone concentrations nowadays are 147% higher (252% in May) than in the 19th century.

1.2 Ozone Precursor Species

Nitrogen Oxides

To a major part NO_x is an anthropogenic trace gas which is built during the fossil fuel combustion of automotive vehicles or power plants [21], building approximately 60% of the estimated global, annual 45±7 Tg N nitrogen oxides emissions [9]. Rough estimations made by Lee et al. 1997 [22] of the main biogenic sources amount microbial soil sources to about 4 Tg N yr⁻¹ and lightning to 5 Tg N yr⁻¹. A recent evaluation by Beirle et al. 2006 [23] estimates the lightning NO_x production to be just 1.7 Tg N yr⁻¹, but, nevertheless, being an important source especially in the upper troposphere where background levels of NO_x are low and ground based soil or anthropogenic sources are far away. The classification of biomass burning, whose source strength is given as circa 5.3 Tg N yr⁻¹ by Lee et al. 1997 [22], as being an anthropogenic or biogenic source is not consitent in literature, reaching from 100% anthropogenic (e.g. in [24], [25], and [26]), via 50% for scaling purposes in future emission scenarios or just 10% anthropogenic in 19th century as input in climate model calculation [27], to being excluded from anthropogenic sources [28] or not being classified at all and rather treated separately [29].

During the photochemical ozone production, NO_x is not entirely consumed but, depending on its concentration, in large part recycled (compare further chapter 2).

 NO_2 is a toxic gas which is dangerous for the respiratory system. It is also a precursor for a number of harmful secondary air pollutants. This includes nitric acid, the nitrate part of secondary inorganic aerosols and not only ozone but also other photo oxidants like peroxy acetyl nitrates [14] (c.v. page 8).

Volatile Organic Compounds

Like NO_{x} volatile organic compounds have both, anthropogenic and biogenic origin. Depending on the vegetation and industrial influence the mix of VOCs varies a lot. Anthropogenic non methane hydro carbons (NMHCs) mainly consist of alkanes, alkenes and aromatic compounds [30], which are for example byproducts of fossil fuel combustion in vehicle exhausts, leakage losses of fuel storage and transport, or solvent usage [24].

Volatile organic compounds that are emitted by plants are called biogenic VOCs. Prominent examples for biogenic non-methane organic compounds

⁹Radiative forcing is a measure of a factor's influence on the incoming (solar) and outgoing (reflected solar and thermal) radiation. Positive forcing tends to warm, negative forcing tends to cool the surface [10].

(NMOC) are isoprene (C_5H_8), mono- ($C_{10}H_{16}$) and sesquiterpenes ($C_{15}H_{24}$), oxygenated VOCs, e.g. methanol (CH₃OH), and hexene derivatives [31, 32, 33, 34, 21]. Graphic formula of some of these compounds are shown in figure 1.2. Although large uncertainties still exist in biogenic hydrocarbon emission inventories [35], it is assumed, that global biogenic NMOC emissions estimated to be around 1150 Tg carbon yr⁻¹ exceed the anthropogenic emissions (estimate: 60-140 Tg carbon yr⁻¹) by an order of magnitude [31, 36].

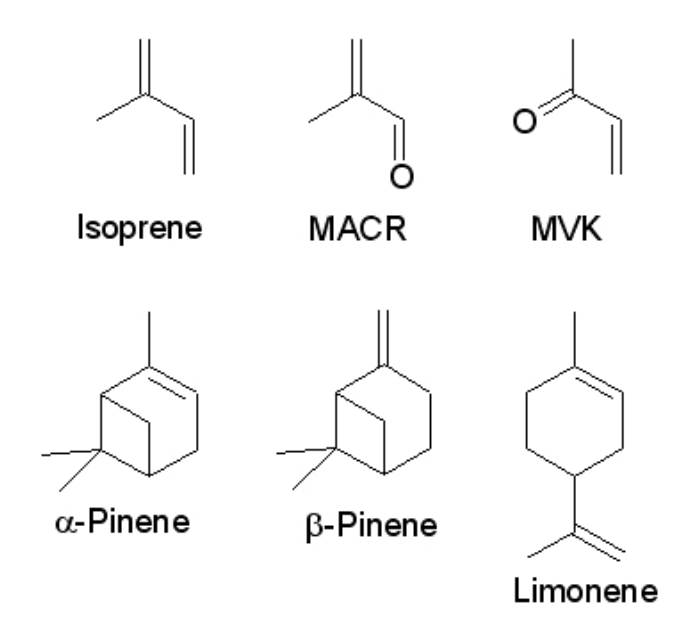


Figure 1.2: Graphic formulas of some important biogenic volatile organic compounds: Isoprene and its degradation products methacrolein (MACR) and methyl vinyl ketone (MVK) and the monoterpenes α -, β -pinene and limonene.

Every emitted VOC that is fully degraded in the gas phase will, after a sufficient amount of degradation steps, which are initialized by the reactions with an OH, O_3 , NO_3 or by photolysis, end up in as many carbon dioxide CO_2 molecules as carbon atoms the VOC initially consisted of. During the degradation it is also possible, that intermediate oxygenated compounds (OVOCs), which are water soluble, are taken up by rain drops and are washed out, or that they become less volatile and can form secondary organic aerosols.

The amounts of the other photochemical products, e.g. ozone, nitric acid ($\rm HNO_3$), nitrates or intermediate peroxyacyl nitrates (see below chapter 1.4), in contrast to the $\rm CO_2$ yield, depend on the chemical (e.g. $\rm NO_x$ concentration) and meteorological (temperature, pressure and solar radiation intensity) environment. According to this, every VOC contributes differently to photochemical ozone production in a polluted atmosphere. This has led to the development of so called "reactivity" or "ozone formation potential" scales for

VOCs. The two widest published and applied of these are the "maximum incremental reactivity" and the "photochemical ozone creation potential" (POCP). The former one has been developed by Carter and co-workers to evaluate the ozone formation for urban environments in the USA for up to two days [37, 38]. The POCP measure has been developed by Derwent and co-workers to assess the ozone formation of up to 5 days for an air parcel travelling over Austria and Germany towards the United Kingdom [39, 40].

1.3 Isoprene

Isoprene (2-methyl-1,3-butadiene, CH₂=C(CH₃)CH=CH₂) is the most important biogenic volatile organic compound concerning photochemical ozone production. It makes up 44% of the global biogenic NMOCs carbon emissions [31]. Deciduous trees are large emitters at daytime [41, 42]. Thus about one ppb isoprene was found over the tropical rain forest of Surinam in the free troposphere [43] and over four ppb were measured directly above the forest canopy of mid-latitudes [44]. Like for all biogenic VOCs, the intensity of the emissions of isoprene strongly depend on temperature (nearly exponentially) and solar radiation, making them highly sensitive to climate change [45]. Additionally isoprene is more reactive towards hydroxyl radicals OH, ozone O₃, and (more important for night time chemistry) nitrate radicals NO₃, than most anthropogenic VOCs [21, 46]. Due to its abundance and reactivity it dominates PBL chemistry in most forested regions and even in some urban environments [47, 48, 49, 50, 51].

When isoprene is chemically degraded in the atmosphere the two main products after the "first degradation step" (the meaning of this term is explained in detail in chapter 4.2) are methacrolein (MACR) and methyl vinyl ketone (MVK). These degradation products are still very reactive and also intensely contribute to tropospheric ozone production provided that NO_x is present.

1.4 Peroxyacyl Nitrates

Like ozone peroxyacyl nitrates (PANs) are secondary air pollutants, built from the same precursor species, and are important contributors to photochemical smog episodes. They are toxic, too, highly water-soluble, therefore cause eye irritations and are said to give rise to skin cancer [52].

For atmospheric chemistry PANs are of importance, cause they are comparatively stable adducts of NO_2 and peroxy radicals, which are intermediates of the VOC degradation and thereby ozone precursors (compare further chapter 2). Due to their stability they can be transported further than NO_2 and the radicals on their own, possibly reaching remote sites with negligible direct anthropogenic impact. By the time the PANs thermally or otherwise initiated decompose, they release NO_2 and the peroxy radicals again, provoking photochemical ozone production there.

Peroxyacetyl nitrate (PAN, CH₃C(=O)OONO₂) is one prominent member

of the PANs. Measured peak concentrations of this compound were 45ppb in Los Angeles in the 2nd half of the 20th century [53]. PAN has a lot of precursor VOCs, the simplest being acetaldehyde (CH₃CHO). More complex ones are isoprene or α -pinene.

Methacryloylperoxynitrate (MPAN, $\mathrm{CH_2} = \mathrm{C}(\mathrm{CH_3})\mathrm{C}(=\mathrm{O})\mathrm{OONO_2}$) is another example for a peroxyacyl nitrate. It exclusively descends from MACR, the degradation product of isoprene. Thanks to this exclusiveness and assuming that MACR solely stems from isoprene, which is, however, doubted by Hakola et al. [54], MPAN has been used as an indicator for photochemical ozone production from biogenic in contrast to anthropogenic volatile organic compounds [55, 56].

1.5 Chemical Weather Forecast

Recapitulating the facts above, one should come to the conclusion, that atmospheric chemistry influences life on earth a lot. For example:

- Building of an ozone layer, which prevents parts of energy rich ultraviolet light from reaching ground level. UVC¹⁰ light is filtered out completely, UVB is screened out in large part. The little UVB light reaching the surface is enough to cause sunburn or even genetic damage.
- Photochemical formation of oxidizing agents, which induce a degradation
 of anthropogenic and biogenic air pollutants allowing the more polar
 (oxidized) species to be washed out by rain or to deposit on the ground.
 Therefore the atmosphere is called to have a self cleaning capacity.
- Composition, transformation and degradation of greenhouse gases, which in the first place making life on earth possible thanks to rising the mean surface temperatures from -18°C to about 15°C. Nowadays climate change due to the anthropogenic rise of greenhouse gas levels since the industrial revolution threatens future generations, as it has extensive impacts on the environment: Droughts, rising sea levels, more severe storms, melting greenland, glacier and polar ice, unfreezing of permafrost areas, intense rains, and acidify of sea water, to name a few [57].
- Photochemically production of secondary air pollutants, e.g. ozone or nitric acid, in the atmosphere, especially the troposphere and PBL. As the precursor species they reside in the air we are continuously exposed to and they are possibly harmful for humans and the environment as a hole

Keeping these points in mind, a sound knowledge of atmospheric chemistry should be established and applied for short term chemical weather forecasts and long term (chemical) climate predictions. This is already done with so-called chemistry transport models (CTMs) or air quality models (AQMs).

 $^{^{10} \}rm When$ considering the effects of UV light on human health and environment, it is separated into three fractions: UVA (400 - 315 nm), UVB (315 - 280 nm), and UVC (< 280 nm).

An example for short term forecast is the 'Regional Atmospheric Chemistry Mechanism' RACM [58], with its update for isoprene degradation [59]. Models of this kind are necessary to develop mitigation strategies for local photochemical smog episodes and to predict ozone levels that exceed the information or alert threshold.

With the aid of the 'Model of Ozone and Related Chemical Tracers' MOZART [60, 61, 62] long term predictions of the atmosphere's abundance of several trace gases can be obtained. Not only the impact of greenhouse gas concentrations on the climate but also vice versa the influence of climate change on trace gas concentrations has been investigated with this model [29].

Essentially CTMs need to deal with a couple of components, as different aspects of the existence of a trace gas have to be considered and modelled. These are for instance:

emissions deviated from numerous emission inventories

giving the strength of anthropogenic and bio-

genic sources

transport directed from the wind field, which is extracted

from meteorological weather forecast and cli-

mate models, respectively

chemical conversion derived from chemical reaction mechanisms,

giving the possible reactions and their velocities depending on trace gas concentrations and

rate coefficients

dry and wet deposition depends on the wind field directed towards the

ground, the solubility of the trace constituent and the cloud and rain occurrence, thus meteorological conditions and trace gas properties

Due to this complexity CTMs have to be evaluated appropriately. This is done by comparing model predictions with ongoing in-situ measurements or field campaigns. In case of climate models it is usual to run them backward in time and adjust them to fit climate history. The history is known for the recent years from former measurements and from palaeoclimatology studies of e.g. sediments, ice cores or tree rings for the far past. Whenever the model results match the measurements within the error margins, it is not granted, that every aspect is represented correctly in the model, but cancelling out of different errors can release good agreement of the examined parameters, too. For example many of the CTMs originally were intended to especially predict ozone concentrations correctly and were "tuned" according to this. The performance of other trace gases were of minor importance.

1.6 Chamber Experiments

To reduce the possible sources of errors, the different aspects of CTMs should be evaluated separately as well. To study atmospheric gas phase chemistry or heterogenous chemistry of aerosols, different environmental chambers have been developed [63]. The central role of environmental chamber experiments is illustrated in figure 1.3. They are a tool to determine the fundamental parameters of chemical gas phase reactions, are used for validation of single reaction aspects or to validate chemical mechanism. More information about these detailed and condensed mechanism is provided in chapter 2.2. They can then be used in CTMs and AQMs.

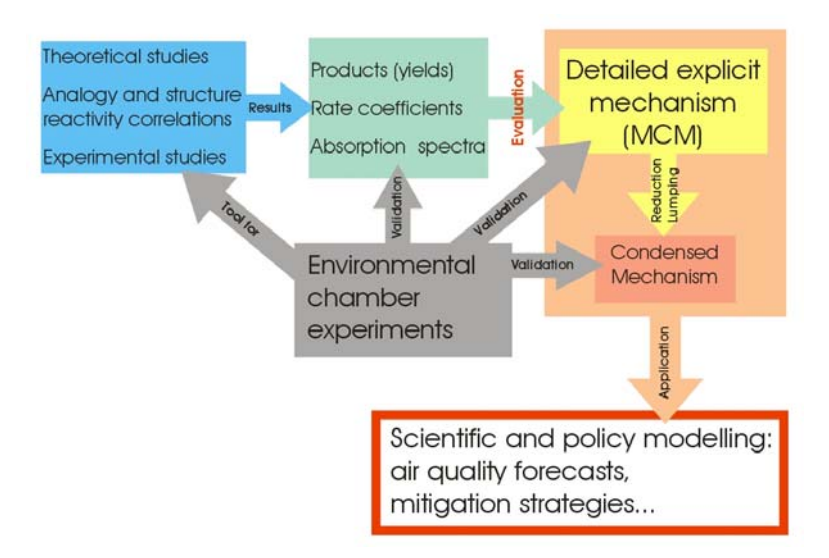


Figure 1.3: Environmental Chamber Experiments play a central role in atmospheric chemistry as a tool for studying fundamental parameters as well as for validating derived gas phase chemical mechanisms.

The two European Photoreactor (EUPHORE) chambers at the Fundación Centro de Estudios Ambientales del Mediterráneo (CEAM) in Spain and the SAPHIR chamber at the Forschungszentrum Jülich (FZJ) in Germany are the two biggest European outdoor chambers, built up to explore gas phase photochemistry with the sun as the natural light source. The AIDA chamber at the Forschungszentrum Karlsruhe (FZK) in Germany is an example for a dark chamber, where research on aerosol physics and chemistry is done [64].

The main principle of these chambers is to provide a preferable air-tight cavity, which can be filled with selected air and aerosol mixtures, where required. No transport takes place and no unknown sources and sinks of the gases should exist in there. Thus the concentration changes of the constituents, which are watched with the help of sophisticated measuring instruments, can be traced back to chemical processes within the gas phase or to interactions with aerosols. The atmosphere simulation chamber SAPHIR (Simulation of Atmospheric PHotochemistry In a huge Reaction chamber), where the experiments of this thesis took place, is described in detail in champter 3.1.

Without chamber facilities special field sites have to be found with the chemical composition and conditions of interest. Preferably these field sites should

be provided with special geographical surroundings, to get rid of at least some of the unwished influences when examining chemistry. For example, such a special site can be a ship some miles away from the coastline. When air masses travel with wind from land over sea to the ship, at least intermediate sources can be neglected. Concentration changes compared to the coast thus mainly will be caused by chemical processing [30].

1.7 Aim of this Thesis

Within the scope of this thesis, special aspects of the current understanding of atmospheric chemistry, described in chapter 2.1, and its implementation into chemical mechanisms (chapter 2.2) have been tested against chamber experiments. The interest was primarily directed towards the Master Chemical Mechanism (MCM) predictions concerning ozone production.

In chapter 3 first of all the SAPHIR chamber, where the experiments took place, is described with all it's features, followed by short descriptions of the entire measuring devices used.

Special attention on the photochemical ozone production during the photochemical degradation of isoprene and its degradation products methacrolein and methyl vinyl ketone, is turned on in chapter 4. Three different approaches to determine the net photochemical O_x production, which are partly applicable to field campaigns, were tested against SAPHIR chamber experiment. In a final conclusion to this chapter, the approaches are compared, and advantages and disadvantages of each of them are discussed.

Problems concerning MCM model representations of $\mathrm{NO_x}$ for the MACR degradation are in detail dealt with in chapter 5. By looking at the $\mathrm{NO_x}$ budget, it is figured out, that the PAN yield of the MCM methacrolein daytime degradation and the MPAN yield of the nighttime degradation is most likely incorrect.

The thesis concludes with a résumé and outlook.

2 Theory

2.1 Gas Phase Chemistry

As already pointed out in the introduction, a lot of chemical processes take place in the troposphere. When dealing with the tropospheric gas phase, not with heterogenous processes on surfaces, only four different kinds of reactions have to be considered: The low density in air just allows at most two reaction partners to meet and react with each other, possibly needing a third body to give up excess energy.

The common notation for reactions, also used in this thesis

$$A + B \longrightarrow cC + dD$$
 (R2.1)

says, that molecule A and B, the educts, react with each other forming the c products C and d products D. The rate coefficient of such a bimolecular reaction is $k_{R2.1}$, normally given in units cm^3sec^{-1} . The reaction rate $v_{R2.1}$, thus the number of this particular reaction happening per volume and time (unit $cm^{-3}sec^{-1}$) can be calculated from the rate coefficient and the concentrations of the educts A and B ([A] and [B] given in number of molecules per cubic centimeter: cm^{-3}):

$$v_{R2.1} = k_{R2.1} \cdot [A] \cdot [B] \tag{2.1}$$

The second kind of reaction is the so called *termolecular reaction*, where a intermediate adduct in an excited state (AB*) is built from the educts. If no third body is present to take up the excess energy, this adduct decomposes back to its initial educts again. If the excited adduct however hits any air molecule M as the third body, which takes up the excess energy, then it decomposes into different products:

$$A + B \longrightarrow AB^*$$
 (R2.2)

$$AB^* \longrightarrow A + B$$
 (R2.3)

$$AB^* + M \longrightarrow cC + dD + M$$
 (R2.4)

Reactions R2.2 and R2.4 are usually summarized as a quasi bimolecular reaction $\,$

$$A + B \xrightarrow{M} cC + dD$$
 (R2.5)

with the concentration of the third body included into the rate coefficient $k_{R2.5}$:

$$v_{R2.5} = k'_{R2.5} \cdot [M] \cdot [A] \cdot [B] = k_{R2.5} \cdot [A] \cdot [B]$$
 (2.2)

Thermal decomposition is another kind of reaction. A single, meta stable educt decays into two or more products cause of its thermal energy, e.g.:

$$A \longrightarrow cC + dD$$
 (R2.6)

The rate coefficient of such a reaction has the unit sec^{-1} . The reaction rate is given by $v_{R2.6} = k_{R2.6} \cdot [A]$.

If the decomposition is induced by a energy rich UV photon, the reaction is called *photolysis*:

$$A + h\nu \longrightarrow cC + dD$$
 (R2.7)

The photolysis frequency J, unit sec^{-1} , replaces the rate coefficient k (compare further chapter 3.2.5). The rate of reaction R2.7 is calculated by $v_{R2.7} = J \cdot [A]$.

2.1.1 Tropospheric Ozone Production

Photochemical tropospheric ozone production does not proceed in a single, but in a whole set of successive, repeating reactions. The precursor species NO_x , acting as a catalyst, and VOCs or CO, being the fuels, light and ozone itself are needed. Without these species, in clean air, no ozone production takes place in the troposphere, but a background level exists from downward mixing of stratospheric ozone. The production cycle steps, which are fairly understood [65], will be described in the following.

Null Cycle

When just NO_2 is added to the clean air, this can be photolyzed by near UV light¹ yielding nitric oxide NO and ground state atomic oxygen $O(^3P)$:

$$NO_2 + h\nu \longrightarrow NO + O(^3P)$$
(R2.8)

The oxygen atom combines with

a oxygen molecule and builds an ozone: Figure 2.1: Ozone null cycle.

$$O(^{3}P) + O_{2} \xrightarrow{M} O_{3}$$
 (R2.9)

As reaction R2.9 takes place nearly instantaneously, reaction R2.8 and

R2.9 are often regarded as a single reaction,

Ozone null cycle. No ozone is produced but a photostationary state between NO,
$$NO_2$$
 and O_3 is reached.

$$NO_2 + h\nu \xrightarrow{O_2, M} NO + O_3$$
 (R2.10)

with the combined rate coefficient, although it is not only a photolysis, still named after the rate limiting photolysis as J(NO₂).

¹The spectrum of ultraviolet light is subdivided into near UV light (NUV) with a wavelength λ of 400-200nm, far or vacuum UV light (FUV or VUV), 200-10nm, and extreme or deep UV (EUV or XUV), 31-1nm [66]. The ozone layer filters out UV light with $\lambda < 290$ nm.

In turn, the O_3 reacts with NO rebuilding NO_2 and releasing the oxygen molecule (see figure 2.1).

$$O_3 + NO \longrightarrow NO_2 + O_2$$
 (R2.11)

Adding up reactions R2.8, R2.9, and R2.11, except for the photon $h\nu$, both sides are identical, thus no ozone is produced. Therefore, the three reactions together are termed null cycle. A photostationary state (PSS) between NO, NO₂, and ozone establishes, which is chiefly controlled by the fluctuating $J(NO_2)$:

$$\frac{[\text{NO}][\text{O}_3]}{[\text{NO}_2]}\bigg|_{PSS} = \frac{\text{J}(\text{NO}_2)}{\text{k}_{\text{R2.11}}} \tag{2.3}$$

This high, contrary $J(NO_2)$ dependence of NO_2 and O_3 lead to the introduction of the less variable combined quantity O_x , which even is a constant of the null cycle defined as:

$$O_{x} \equiv NO_{2} + O_{3} \tag{2.4}$$

Initialization, Creation of OH

Not only NO_2 , but also tropospheric ozone can be photolyzed by UV light. At wavelength longer than 320nm, beside an oxygen molecule once more ground state atomic oxygen $O(^3P)$ is produced. At shorter wavelength, with the photolysis frequency of reaction R2.13 being denoted as $J(O^1D)$, electronically excited $O(^1D)$ atoms are built:

$$O_3 + h\nu \longrightarrow O_2 + O(^3P)$$
 (320nm < λ) (R2.12)

$$O_3 + h\nu \longrightarrow O_2 + O(^1D)$$
 (290nm < λ < 320nm) (R2.13)

Even though reaction R2.12 is the much more frequent one of these two photolysis reactions, as the photon density in this wavelength region is much higher, it is not that important for photochemistry, as nearly all $O(^3P)$ rapidly recombines with oxygen rebuilding ozone (compare reaction R2.9). Photolysis and recombination result in a steady state concentration of about 10^3 $O(^3P)$ atoms per cubic centimeter.

The excited $O(^{1}D)$ atom however, if not quenched to $O(^{3}P)$ by collision with oxygen or nitrogen,

$$O(^{1}D) + O_{2} \longrightarrow O(^{3}P) + O_{2}$$
 (R2.14)

$$O(^{1}D) + N_{2} \longrightarrow O(^{3}P) + N_{2}$$
 (R2.15)

reacts with water vapor and forms two highly reactive hydroxyl radicals OH:

$$O(^{1}D) + H_{2}O \longrightarrow 2 OH$$
 (R2.16)

Photochemical Ozone Production Cycle

In short, the OH radicals react with CO or VOCs building hydroperoxy (HO₂) and organic peroxy radicals (RO₂). The peroxy radicals oxidize NO to NO₂. That corresponds to a disturbance of the null cycle described above, as NO₂ is produced without a compensatory consumption of O₃. The subsequent photolysis of NO₂ (reaction R2.10) thus means a net production of ozone. Other possible initializations of the cycle than by OH attack, that will not be presented here, are ozonolysis, reaction with NO₃ in particular during nighttime, and photolysis of aldehydes.

In case of CO as the fuel in the oxygen containing atmosphere, the starting reaction of the ozone production cycle is the attack of OH on CO, yielding the hydroperoxy radical and carbon dioxide:

$$OH + CO \xrightarrow{O_2} HO_2 + CO_2$$
 (R2.17)

The CO_2 is an end product which will not react any further. The HO_2 however oxidizes nitrogen monoxide to nitrogen dioxide and OH is rebuilt.

$$NO + HO_2 \longrightarrow NO_2 + OH$$
 (R2.18)

As above mentioned, the NO_2 can be photolyzed with ozone being produced (reactions R2.8 and R2.9) and NO being rebuilt. As OH and NO are regained during this cycle, and if no terminating processes (see below) destroyed OH and HO_2 radicals, ozone would be produced as long as the fuel CO is present, with each processed CO yielding one O_3 :

$$CO + 2O_2 \xrightarrow{M, h\nu} CO_2 + O_3$$
 (R2.19)

If a VOC is the fuel, the idealized, simplified cycle is a little more complex. The first step is once again the attack of an OH radical in the oxygen containing atmosphere. Depending on the kind of VOC, the OH radical can abstract a hydrogen atom from a C-H bond, with the freed bond occupied by an oxygen molecule, e.g.:

$$R-CH_3 + OH \xrightarrow{O_2} R-CH_2O_2 + H_2O$$
 (R2.20)

or can break a double bond and add on one of the neighboring C atoms, and oxygen adds on the other, e.g.:

$$R=R' + OH \xrightarrow{O_2} RO_2 - R'OH$$
 (R2.21)

Like in reaction R2.18 the RO_2 (R– CH_2O_2 and RO_2 –R'OH in the example reactions R2.20 and R2.21 respectively) reacts with NO to build NO₂ and thus O_3 via reaction R2.10. No OH atom is rebuilt in this reaction step, but an alkoxy radical RO emerges.

$$RO_2 + NO \longrightarrow RO + NO_2$$
 (R2.22)

In the presence of oxygen the RO (= R'CH₂O) gives off one more H-atom to form a double bond with the O-atom:

$$RO \xrightarrow{O_2} R'CHO + HO_2$$
 (R2.23)

It can isomerize or decompose, with $\rm HO_2$ as a product among others, too. The $\rm HO_2$ radical does the same as before, namely oxidizing NO to $\rm NO_2$ (reaction R2.18) and rebuilding OH. The R'CHO is an intermediate product, which will not degrade further, unless a second initialization takes place. Summing up the simplified VOC degradation schematically shown in figure 2.2, two ozone molecules are built when two H-atoms of the VOC or one H-atom and a C-C (double) bond are replaced by one double bonded O atom in the first generation degradation products of the initial VOC:

$$R-CH_3 + 4O_2 \longrightarrow R-CHO + H_2O + 2O_3$$
 (R2.24a)

$$RCH=R' + 4O_2 \longrightarrow RC(=O)-R'OH + 2O_3$$
 (R2.24b)

These first generation products are oxidized in the same way again, restarting the ozone production cycle. The degradation continues, until the initial VOC is totally degraded towards $\rm CO_2$ and $\rm H_2O$ molecules. In theory, the maximum possible number of ozone molecules produced during the complete photochemical OH induced degradation of a VOC corresponds to the number of C–H and C–C bonds of the initial VOC, which are called reactive bonds [67]. A C=C double bond counts as two C–C single bonds. If the degradation is induced by photolysis, this balance can even be exceeded. An example is the radical photolysis path of formaldehyde R3.6 in chapter 3.1.3, where the production of three ozone molecules is enabled although formaldehyde has only two reactive C–H bonds.

Chain Terminating Reactions, By-Products

The theoretically possible number of ozone molecules per VOC is never reached in reality due to the fact, that not all $\rm HO_2$ and $\rm RO_2$ react with NO to form $\rm NO_2$, and not all $\rm NO_2$ are photolysed to form $\rm O_3$. These branching reactions, where radicals are consumed and do not produce ersatz radicals, are called radical or chain terminating reactions. They also compensate for the production of new radicals, like the OH production described above, and hinder the radical concentration to rise without letup. They are summarized and schematically shown in figure 2.3.

The most important terminating reactions just concerning inorganic species are the formation of nitric acid, a main component of acid rain:

$$OH + NO_2 \longrightarrow HNO_3$$
 (R2.25)

and the production of hydrogen peroxide, where even two peroxy radicals are destructed:

$$HO_2 + HO_2 \longrightarrow H_2O_2 + O_2$$
 (R2.26)

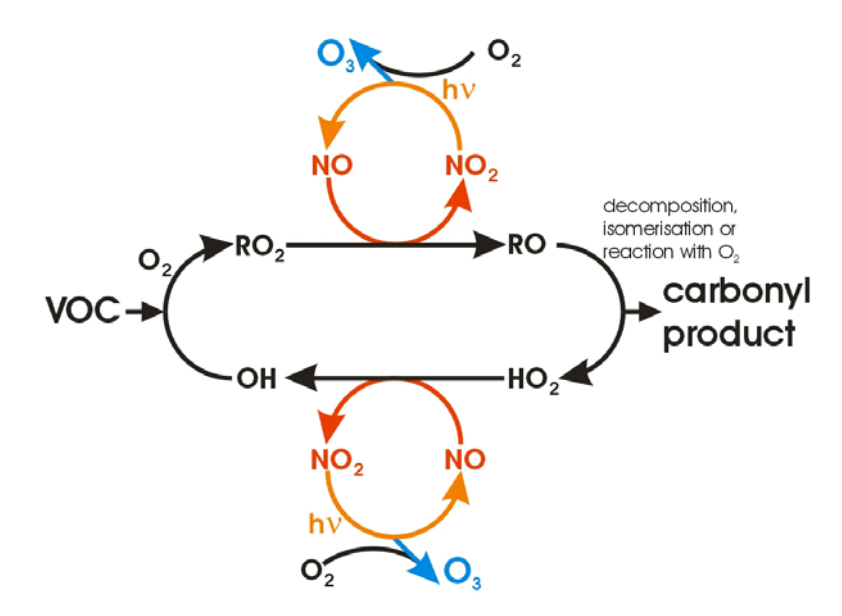


Figure 2.2: Idealized schema of the OH induced VOC degradation. In one degradation step, leading from the original VOC towards a carbonyl product, two NO_2 , thus O_3 molecules are produced. OH radicals are rebuilt.

This is also the case, when organic peroxy radicals react with HO_2 :

$$RO_2 + HO_2 \longrightarrow ROOH + O_2$$
 (R2.27)

or two organic peroxy radicals reacting with each other:

$$RO_2 + R'O_2 \longrightarrow ROH + R'_{-H}O + O_2$$
 (R2.28)

An important sink not only for radicals, but also for NO_x , is the formation of organic nitrates. They are formed as a byproduct of reaction R2.22 when the intermediate ROONO* instead of decomposing into RO and NO_2 stabilizes [68]:

$$RO_2 + NO \longrightarrow ROONO^* \longrightarrow RONO_2$$
 (R2.29)

Although the ratio between the production velocities of reaction R2.29 and R2.22:

$$\frac{v_{R2.29}}{v_{R2.22}} = \frac{k_{R2.29} \cdot [RO_2][NO]}{k_{R2.22} \cdot [RO_2][NO]} = \frac{k_{R2.29}}{k_{R2.22}} < 15\%$$
 (2.5)

is quite low, it is reported, that organic nitrates can make up 15-20% of the reactive $nitrogen^2 NO_v$ in forested environments [69].

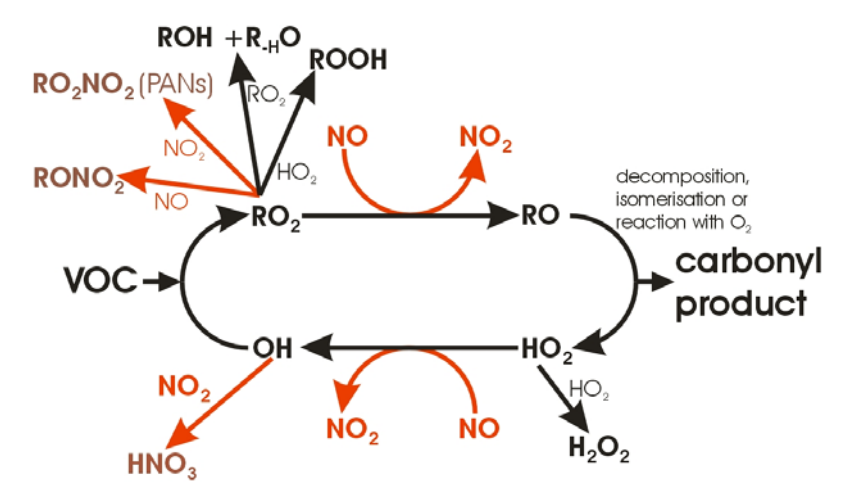
 $[\]overline{^2}$ Reactive nitrogen (NO_y) is the sum of NO_x and its oxidation products. The most important components are NO, NO2, HNO3 and aerosol NO3, PANs and other organic nitrates, NO3, N2O5, HONO, and HNO4.

A temporary sink for peroxy radicals and NO_x is the formation of peroxyacyl nitrates PANs, which is balanced by their thermal decomposition:

$$RO_2 + NO_2 \longrightarrow RO_2NO_2$$
 (R2.30f)

$$RO_2 + NO_2 \leftarrow RO_2NO_2$$
 (R2.30b)

Especially the backward reaction R2.30b is strongly temperature dependent. Therefor the PANs (RO₂NO₂), if they reach cool air masses in higher altitudes or latitudes, can travel far away from the place they formed. If the polluted air masses warm up again, the PANs decompose and act as a source for RO₂ and NO_x, and therewith can induce ozone production in remote areas.



 $\begin{tabular}{ll} Figure~2.3:~Chain~terminating~Reactions.~The~most~important~radical~and~NO_x~consuming~reactions~are~schematically~shown.~Reactions~with~NO_x~are~marked~with~reddish~arrows. \end{tabular}$

2.1.2 Chemical Regimes

The termination processes cause the ozone production cycle to be dependent on the NO_x concentration heavily. In remote areas, with NO_x levels below $\approx 0.1 ppb$, nearly no NO is present as a partner for HO₂ and RO₂ in reactions R2.18 and R2.22. Thus, the radical termination of reactions R2.26, R2.27 and R2.28 get more importance. Even the reaction of HO₂ and ozone

$$HO_2 + O_3 \longrightarrow OH + 2O_2$$
 (R2.31)

becomes relevant, so that instead of an ozone production an ozone reduction takes place.

In highly (above around 10ppb) NO_x polluted, called urban areas, the produced OH mainly reacts with NO₂ directly (reaction R2.25). Thereby less OH is available for attacking the CO or VOC, the cycle throughput, thus ozone production, is reduced.

The maximum ozone production takes place in rural areas with about one $ppb \text{ NO}_x$. The OH concentration is relatively high to induce the degradation and enough NO is present to react with the formed HO_2 and RO_2 .

Of course, the ozone production rate depends on the CO and VOC concentration, too. As for the NO_x , the dependence is by no means linear. Reduction of VOC and CO always result in less ozone production, but in some regimes, a huge reduction of VOC just lead to a slight decrease of the ozone production.

The dependencies on the $\mathrm{NO_x}$ and VOC (CO) concentrations are graphically illustrated in figure 2.4. It shows the color coded isopleths (not linearly scaled) of the ozone production dependent on the $\mathrm{NO_x}$ (logarithmic x-axis) and CO concentration (logarithmic y-axis) for a simple model case, which mainly contains the inorganic part of the reactions described above. (Details of the model mechanism can be found in the appendix A.3.) Bluish colors represent slight ozone destruction, green to red slight to high ozone production. Two points of the isopleths plot are marked with big black symbols, representing points of different chemical regions:

 NO_x limited The diamond \spadesuit is placed in the so-called NO_x limited region: A reduction of NO_x , e.g by a factor of three (horizontally shifted small symbol of the same shape) results in a considerable lowering of the ozone production (from near 5ppb/h towards nearly 1ppb/h). Starting at the same point and reducing the CO concentration by the factor three (vertically shifted small diamond) effectuates nearly no reduction. An indication for this region is a high VOC/NO_x ratio.

VOC limited The star \star is placed in the VOC (in this model case just CO) limited region: Now a reduction of CO by the factor three results in a clear lowering of the ozone production rate, a reduction of NO_x, contrary to naive expectations, leads to an increase of the ozone production. This chemical regime is indicated by a lower VOC/NO_x ratio.

2.2 Chemical Mechanisms

To give an overview of the ozone production cycle in chapter R2.16, generalized reactions with R representing any VOC where given. To really understand atmospheric chemistry, as much of the multitudinous individual VOCs reactions as possible have to be analyzed regarding rate coefficients or branching ratios. For the most abundant and thus important VOCs, such studies have been done. The partially diverging results are made available in numerous publication. For a single person it is a vain endeavor trying to get a global overview and keep up to date with every new finding.

For this purpose, two competitively committees were established, which have gathered and evaluated previous and new findings on environmental gas phase chemical reactions, and periodically give out recommendations. One board is the NASA Panel for Data Evaluation of the Jet Propulsion Laboratory (JPL), California Institute of Technology. The JPL Panel was established by the

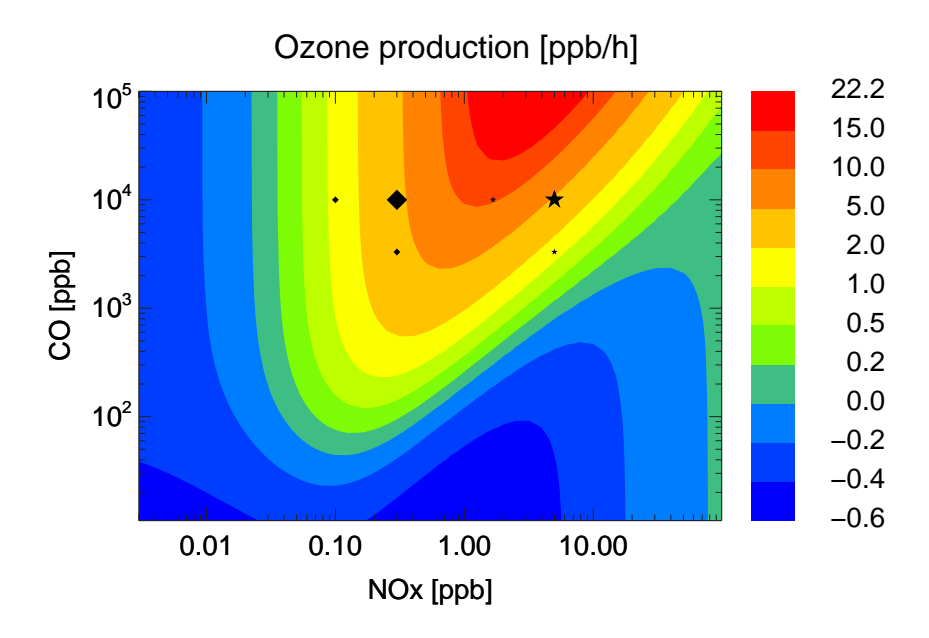


Figure 2.4: NO_x and VOC dependence of the ozone production demonstrated with a simple model case. Shown are the color coded isopleths of the O_3 production rate. The diamond \spadesuit is placed in the NO_x limited, the star \star in the VOC limited regime. Reductions of VOC or NO_x by a factor three (small symbols) have crucially different effects on the particular parent rate, even an increase in one case.

NASA Upper Atmospheric Research Program Office in the year 1977. Its aim is to "provide a critical tabulation of the latest kinetic and photochemical data for use by modelers in computer simulation of atmospheric chemistry" [70]. The JPL data are constantly updated and published on the panel's web page [71]. The current *Evaluation Number 15* contains about 700 bi-, termolecular and equilibrium gas phase reactions and about 200 absorption cross sections of photolysis reactions.

The second board is the *IUPAC Subcommittee for Gas Kinetic Data Eval-* uation, which superseded the CODATA (Committee on Data for Science and Technology [72]) Task Group on Chemical Kinetics in 1986. This CODATA task group itself constituted in the same year as the NASA panel under the auspices of the International Council of Scientific Unions. The present report out of the year 2004 is *Supplement VIII*, which contains approximately 600 gas phase reactions [73, 46, 74]. This evaluation is updated continuously and made public on the committees web page [75], too. In the meantime even around 70 heterogeneous reactions are evaluated and published on the internet.

The IUPAC data additionally provide a basis for the *Master Chemical Mechanism* (MCM). The wrights of the MCM try to provide an explicit represen-

tation of the elementary reactions relevant to VOC degradation. Where available, evaluated parameters, e.g. rate coefficients or branching ratios, are applied. Gaps of experimental (evaluated) data are filled by using analogy and 'structure-reactivity correlations'. Details of the construction can be found in the Mechanism Development Protocol [76]. The first version out of the year 1996 (the website launched in March 1997) contained the degradation of methane and 119 NMHCs, forming round 2500 chemical species and round 7000 chemical reactions. Nowadays the MCM v3.1 contains 125 initial VOCs: 104 non-aromatic anthropogenic species, 18 aromatics, and with isoprene, α pinene, and β -pinene three biogenic compounds. This adds up to round 4400 species and 12700 reactions [77, 78]. In contrast to the JPL and IUPAC web sites, where the chemical data are provided in conventional hard copy form with a focus on the documentation of the data origin, the Master Chemical Mechanism is stored in a database with a web interface [79, 80]. The user can browse through the mechanism, mark species, and download the whole, or extract and download a subset of the mechanism. Such a subset contains all reactions, which are possible with the marked initial specie, all its degradation products, and inorganic species. Different formats for the download can be selected, e.g. HTML, FORTRAN or FACSIMILE. Subsets for isoprene (C5H8), methacrolein (MACR), and methyl vinyl ketone (MVK) in FACSIMILE format were the fundament of the simulations done in this thesis.

Currently the ongoing "Knowledge Transfer Project: MCM - IUPAC integration" tries to improve the integration and collaboration between the MCM and the IUPAC Subcommittee for Gas Kinetic Data Evaluation. Aims of this project are the enhancement of the IUPAC database, development of common web-based tools, integration of both databases and provision of online tools for communication and exchange of data [81].

The huge number of species and reactions makes the MCM unfeasible to apply in chemistry transport models. Instead of using such a nearly explicit mechanism, condensed mechanisms have been developed. Different lumping approaches were used, especially to reduce the isoprene degradation mechanism. Compared to the MCM, the number of isoprene related reactions and species in such a lumped mechanisms is reduced by at least an order of magnitude. For lumping species and reactions, different approaches, e.g. accounting for functional groups, carbon bonds, or chemical lifetimes, are followed. Example mechanisms are the Carbon Bond IV mechanism CBM-IV [82], the Regional Atmospheric Chemistry Mechanism RACM [58], the Model of Ozone and Related Chemical Tracers MOZART [60, 61], the Mainzer Isopren Mechanismus MIM [83], or the condensed version of the Statewide Air Pollution Research Center SAPRC-99 mechanism [84]. Intercomparisons between condensed photochemical mechanisms can be found in *Pöschl 2000* [83] and *Russell 2000* [85].

2.3 Numerical Solving

Due to their complexity, realistic photochemical reaction mechanisms, in contrast to strongly simplified model studies, can only be solved numerically. The first step in the process is the translation of the chemical mechanism into a system of first order differential equations. For every variable specie V, a balance equation is set up, giving its concentration change d[V]/dt subject to its production P and destruction D:

$$\frac{d[V]}{dt} = P - D = \sum_{i=1}^{n} p_i \cdot v_i - \sum_{j=1}^{m} d_j \cdot v_j$$
 (2.6)

The overall production P is the sum of the reaction rates v_i of the n reactions, where the specie V is produced p_i times. The overall destruction D is the sum of the reaction rates of the m reactions, where d_i molecules of specie V are consumed, with this destruction rate depending on the concentration of V (see page 13). If measured concentrations are used as input for the model, no balance equations has to be set up for this specie, cause it will act as a prescribed boundary condition. Which measured species to read in strongly depends on the scientific objective examined. In some cases, e.g. study of a rate coefficient, prescribing the determining, reaction inducing radical, whose concentration is most likely not only influenced by the researched reaction, is the means to an end. If fundamental changes in the mechanism are done, prescribing of species concentration may wipe out shortcomings of the mechanism. Not prescribing species influenced by the model changes is mandatory then [86].

The numerical solver FACSIMILE (AEA Technology) was used for the model runs of this thesis. As chamber experiments with the trace constituents being uniformly mixed (see next chapter, especially table 3.1) were modelled, just the chemistry, sources and sinks, and no transport have to be considered, making a photochemical box model the adequate choice. The set up of the FACSIMILE input file is simplified by the IDL (Interactive Data Language, Reseach Systems Inc. [87]) based EASY (Easy AtmoSpheric chemistry) package developed by Brauers and Rohrer 1999 [88]. In a first step, this pre- and postprocessing tool translates special EASY input files, particularly containing reactions, rate coefficients, constants, function definitions, the name of an experimental data set to be used as boundary conditions, and initial concentrations of the trace constituents, into an FACSIMIE input file. Examples for EASY input files can be found in appendix A. To make such files more concise, it is possible to save information into separate files and call these by the main file via an include routine.

The FACSIMILE program, which is automatically started by EASY in a second step, is forced to write three output files in .ENZ format, which is a plain ASCII file with a well defined header and column separated data for each time step [89]. One FACSIMILE output file contains the species' concentrations and settings, the second the rate coefficients and reaction rates, and the third one production and destruction terms for each variable specie. The FACSIMILE output files are optionally postprocessed by the EASY programm, which may

write different output formats or produce graphical output. Numerous routines also exist in the ICG IDL library [90] to do postprocessing and create graphical output suitable for the scientific objective of interest easily.

To simply use the MCM or a subset of the MCM the IDL based converter tool mcmcv has been developed further and provided with a graphical user interface during this thesis. It translates a downloaded MCM file (FACSIMILE format) into a SAPHIR chamber specific EASY input file, already accounting for the chamber features described in chapter 3. Additionally, the mechanism is reduced by checking for valid reactions being possible at all with the prescribable initial species.

3 Experimentals

3.1 The SAPHIR Chamber



Figure 3.1: Picture of the atmosphere simulation chamber SAPHIR situated at the Forschungszentrum Jülich.

The atmosphere simulation chamber SAPHIR (figure 3.1) at the Forschungszentrum Jülich is operated by the Institute for Chemistry and Dynamics of the Geosphere ICG-2: Troposphere. It was constructed to enable research on atmospheric chemistry at natural trace gas concentration, independent of transport processes or unknown sources and sinks of air pollutants. It consists of a double walled near cylindrical Teflon tube, which is fixed at four steel girders. The FEP foil (DuPont, per-fluoro-ethylenepropylen) has a thickness of $125\mu m$ for the inner tube except for the bottom, which is only a single layer of $500\mu m$ thickness. The outer tube consists of a $250\mu m$ FEP film. The foil was chosen due to its chemical inertness and the permeability for UV light. Their transmission properties and the shadowing effects of the girders are well characterized. On a clear sky day in summer 0.65 - 0.86 and 0.60 - 0.73, of outside J(NO₂) and J(O¹D), respectively, are measured inside the chamber

[91, 92]. In addition, a shutter system is provided for darkening the chamber and enable research on nighttime atmospheric chemistry. This shutter also serves as a protection from bad weather conditions like storms or hail. The opening and closing time is 60 seconds. A second shutter system provides a filter setup to cull light below 370nm wavelength.

The chamber is about 20 meters long and 5 meters in diameter, with the long axis aligned in north-south direction. The effective volume is around $270m^3$. The foil surface towards the reaction chamber is $324m^2$. Compared to smaller chambers, the volume to surface ratio of 0.83m is very big, making surface effects less important. The chamber volume and the space between the double walls is filled and constantly flushed with synthetic air generated from high purity liquid nitrogen N_2 and oxygen O_2 (Linde AG, purity 6.0). The N_2 : O_2 mixing ratio is nearly the one of ambient air, 80: 20. A replenishment is necessary to retain a slight overpressure of 40Pa above ambient level to prevent pollutants from diffusing into the chamber, as inside air is lost through small foil leakages and because of the sampling by some measuring devices. The replenishment flow, also called experimental flow, lies between 3 and $15m^3/h$. When the chamber is prepared for a new experiment, a purge flow with $500m^3/h$ at maximum can be used to dilute remainder of trace gases inside SAPHIR as much as needed, in the majority of cases below the detection limits of the measuring instruments. The purge flow is also used, when the chamber air is humidified with high purity water (Milli-Q Gradient A10, Millipore Corporation) to up to 80% relative humidity. When the chamber is flushed more then ten times its volume, a minimum humidity of 0.08mbar is reachable. The purge and the replenishment flow are operated each with an appropriate flow controller. A temperature control is not provided for the SAPHIR chamber, hence it is operated at ambient temperature or, as in a greenhouse, slightly above when sunlit.

Trace gases are injected using the experimental flow. Ozone is in situ produced by a ozonizer (Ozonia) via a silent discharge. It is dosed via the injection time. Gaseous constituents, e.g. CO, CH_4 , NO or NO_2 are provided in gas bottles in pure form or as a mixtures with inert gases like N_2 . The gas bottles can be connected with the injection system via inlet pipes. Different flow controllers enable a precise input. VOCs that are liquid at room temperature and pressure are added with an injection via a septum into a heated inlet pipe. The trace gases mix within 10 minutes, when the chamber is sunlit, and within 30 minutes in the dark chamber. To accelerate the mixing, a van can be operated inside the chamber, reducing the mixing time to about one minute [93].

Technical specifications of the SAPHIR chamber noted above are summarized in table 3.1. A more detailed description can be found in *Rodriguez Bares* 2003[94].

The SAPHIR chamber provides the unique feature of being operated with high purity synthetic air. This enables kinetic studies to determine rate coefficients [95] and product yields [96] of selected reactions at near ambient conditions and gives the opportunity to make up the balance for dedicated atoms or molecule groups [86]. As the experiments can be performed at am-

Table 3.1: Technical specification of the SAPHIR chamber.

Table 5.1. Technical specification of t	ne om mine.
Shape	cylindrical
Length	$\approx 20m$
Diameter	$\approx 5m$
Effective Volume	$270m^{3}$
Surface towards reaction chamber	$324m^2$
Wall material	FEP teflon
Wall thickness	$125 - 500 \mu m$
Shutter system closing/opening time	60sec
Gas supply	$N_2: O_2 = 80:20$, purity 6.0
Experimental flow	$3 - 15m^3/h$
Purge flow	up to $500m^3/h$
Humidity	0.08mbar partial pressure
	to 80% relative humidity
Mixing time	$\approx 10min$ (lit)
	$\approx 30min \text{ (dark)}$
	$\approx 1min \text{ (fan)}$
Pressure	ambient pressure $+$ 40Pa
Temperature	ambient conditions $+$ small ΔT

bient trace gas concentrations, almost no up or down scaling of the achieved results is necessary for the application to tropospheric conditions. This is of big advantage, as atmospheric chemistry processes by no means linearly, which makes extrapolations potentially difficult.

The SAPHIR chamber is also constructed to offer an experimental site for measuring instrument intercomparisons (e.g. during the HOxComp campaign in summer 2005, when different instruments for OH and $\rm HO_2$ measurements were compared [97]).

Despite the sophisticated concept of the SAPHIR chamber and the wished difference concerning transport and unknown sources and sinks for trace gases, some characteristics, both, foreseen and discovered during the operation, are making the chemical conditions inside decisive unequal to normal ambient conditions. These characteristics are monitored and quantified with the help of so-called standard experiments. Therefor, the chamber with dry or humidified "clean" air is illuminated, and the development of at least the trace gases NO, $\rm NO_2$, and $\rm O_3$ beside the meteorological condition pressure and temperature and the photolysis frequencies $\rm J(NO_2)$ and $\rm J(O^1D)$ are measured. A list of the standard experiments carried out between Jun 2004 and Sept 2006 is provided in appendix B, table B.1. The important SAPHIR characteristics are described

 $^{^1\}mathrm{In}$ this context clean means, that no trace gases, except for water, are above the limit of detection (LoD) of the operated measuring instruments. In the circumstances, that not all instruments are running, which is the normal case, at least $\mathrm{O_3}$ and $\mathrm{NO_x}$ are brought below LoD. The concentrations of other trace gases can be estimated from the volume of air flushed through the chamber with the replenishment or purge flow since the time, they or their precursors were injected.

in the following.

3.1.1 Dilution

As mentioned above, a replenishment flow of some m^3/h of synthetic air is necessary to maintain a slight overpressure inside the reactor. This flow causes a permanent dilution of each trace constituent. The decay of a trace gas due to dilution can be described by the following differential equation:

$$-\frac{dC(t)}{dt} = \frac{F_R(t)}{V_{eff}} \cdot C(t) = k_{Dil}(t) \cdot C(t)$$
(3.1)

Here C(t) is the concentration of the trace constituent depending on time t, F_R is the replenishment flow and V_{eff} is the effective volume of the SAPHIR chamber. F_R/V_{eff} are summarized in the constant k_{Dil} , which corresponds to a rate coefficient of a first order reaction. Separation of the variables and integration yields:

$$C(t) = C_0 \cdot \exp\left(-\int_0^t k_{Dil}(t)dt'\right)$$
(3.2)

The concentration at t=0 is denoted C_0 here. If the replenishment flow is constant and thus $k_{Dil}(t) = k_{Dil}$, equation 3.2 can be simplified to $C(t) = C_0 \cdot e^{-k_{Dil}t}$. With a mean replenishment flow of $8m^3/h$ and the stated effective volume of $270m^3$, the concentration of each trace constituent exponentially decreases by nearly 3% per hour just owing to the dilution, and without any chemical reaction or deposition taking place.

3.1.2 HONO Source

Nitrous acid (HONO or HNO₂) is known as an important radical source in the atmosphere as well as in simulation chambers [98, 99]. Its photolysis

$$HONO+h\nu \longrightarrow NO+OH$$
 (R3.1)

produces OH radicals. In the SAPHIR chamber, the HONO source is the most important primary radical source. The formation of HONO in smog chambers has been detected more than a quarter of a century ago [100]. For these kind of chambers, which are much smaller than the SAPHIR chamber and that are operated at much higher (at least two orders of magnitude) trace gas concentrations, two processes for the HONO formation were postulated. The first one is a heterogenous dark reaction of NO₂ plus water:

$$2NO_2+H_2O \longrightarrow HONO+HNO_3$$
 (R3.2)

dealt with in numerous articles [101, 102, 103, 104, 105]. This kind of reaction can be excluded as being important for the SAPHIR chamber, as not enough NO_2 is present to explain the HONO formation rate detected.

The second kind of process postulated is a photoenhanced HONO formation,

$$S_{HONO} + h\nu \longrightarrow HONO$$
 (R3.3)

where S_{HONO} stands for a unknown source [105]. A HONO formation of the second kind has been expected and detected during standard experiments in the SAPHIR chamber as well. The chemical or physical process behind the formation is still unclear, but a heterogenous process at the chamber walls is expected. The source strength showed a dependence on relative humidity RH, temperature T, and NO_2 photolysis frequency $J(NO_2)$. An empirical formula to describe the HONO source strength S_{HONO} in $[cm^{-3}sec^{-1}]$, RH in %, T in Kelvin and $J(NO_2)$ in sec^{-1} has been found [106]:

$$S_{HONO}(J(NO_2), RH, T) = K \cdot J(NO_2) \cdot \left(1 + \left(\frac{RH}{RH_0}\right)^2\right) \cdot \exp\left(-\frac{T_0}{T}\right)$$
(3.3)

Here K is an adjustable scaling factor which changes with time. The values for RH_0 and T_0 are 11.6% and $3950\mathrm{K}$, respectively. Between Jul 2001 and Jul 2002 the scaling factor grew from round $4.7 \cdot 10^{13} cm^{-3}$ to $8.5 \cdot 10^{13} cm^{-3}$ having quite constant periods in between. During the experiments dealt with in this thesis, a bigger variance occurred. The standard experiments on the 20th and 28th Sep 2005, for example, showed a HONO source with K being $7.1 \cdot 10^{13} cm^{-3}$ and $20.7 \cdot 10^{13} cm^{-3}$ respectively (c.f. chapter 4.1), a changing by almost a factor three within nine days. Hence, the HONO source strength had to be adapted for each experiment separately. This was done by adjusting the modelled HONO concentration to measurements, or, if HONO was not measured itself, by adjusting the modelled to the measured NO_x concentration. This can be challenging in cases, where the NO_x budget of the studied trace gas mix is not represented exactly enough in the chemical mechanism.

3.1.3 HCHO Source

When irradiated, also the formaldehyde (HCHO) level in the chamber air rises. As for the HONO source, the exact chemical and physical process is unknown. Photolytic sources of HCHO have also been observed in field campaigns. For example, the arctic ice and snow surface has shown to emit HCHO [107, 108]. For the SAPHIR chamber it is suggested, that organic compounds deposit at the chamber walls during former experiments, which are photolytical fragmented and result in some volatile HCHO. Looking at the fate of the built HCHO given later in reactions R3.4 to R3.6, it is obvious, that the HCHO source has a relevant influence on the radical and ozone building capacity of the SAPHIR chamber and thus has to be quantified as good as possible.

For the dry chamber (RH < 1%) between Aug 2002 and Sep 2003 an empirical formula for the HCHO source strength S_{HCHO} in $[cm^{-3}s^{-1}]$ has been found by Karl~2004~[109]:

$$S_{HCHO}(J(NO_2), T) = B \cdot J(NO_2) \cdot \exp\left(-\frac{T_0}{T}\right)$$
 (3.4)

The scaling factor B was identified to be $3.29 \cdot 10^{17} cm^{-3}$ and T_0 to be 6142K.

The water dependance of the SAPHIR HCHO source has not been examined so far, but exists, as e.g. can be seen clearly by analyzing the experiment carried out on the 17th of July 2005, shown in figure 3.2. This has been a standard experiment with four illuminating periods (orange hatched areas in the upper and middle panel of figure 3.2) of one hour each followed by one hour darkness. During the three meanwhile dark spaces of time, the relative humidity has been elevated stepwise from 0.3% up to nearly 48%. The formaldehyde concentration measured with the Hantzsch monitor (blue crosses in the top panel, left axis; the instrument is described in chapter 3.2.3) after four hours of elucidation exceeds three ppb, although huge parts of it were flushed out especially during the humidification process done with the help of the purge flow. The HCHO increase is not uniform, but is getting steeper each consecutive lit period. To deduce the production rate of HCHO during the lighting, the balance equation for HCHO has to be solved for the HCHO chamber source term S(HCHO):

$$S_{HCHO} = \frac{d[HCHO]}{dt} + (k_{OH}[OH] + J(HCHO, r) + J(HCHO, m) + k_{dil})[HCHO]$$
(3.5)

The net HCHO change rate d[HCHO]/dt can be approximated by the difference quotient $\Delta[HCHO]/\Delta t$ of the concentration-time profile or by a linear least square fit of the time series.

The first method has been used for the small time step of two minutes after interpolating the HCHO profile onto a equidistant time pattern t_i denoted as $[HCHO]_{sync}$ with $\Delta t = 60sec$. The interpolation limit was two minutes. Then, the mean value of the forward and backward differences is calculated following equation 3.6, where the abbreviation C is used for $[HCHO]_{sync}$.

$$\frac{dC}{dt}(t) \approx \frac{\Delta C}{\Delta t} \Big|_{t=t_i} \stackrel{\text{def}}{=} \frac{C_i - C_{i-1} + C_{i+1} - C_i}{(t_i - t_{i-1} + t_{i+1} - t_i)} = \frac{C_{i+1} + C_{i-1}}{2\Delta t}$$
(3.6)

For the first and last point of a continuous $[HCHO]_{sync}$ lit period, the forward and backward difference is used respectively.

The second method was used, when looking at the 20 minutes average values. The line of best fit is defined as the one, with the sum of the squared differences between itself and the measurement being minimal. The gradient of the fitting line corresponds to the approximated HCHO change rate at the mid point of the 20 minutes fitting interval. For each point of time t_i , with $t_i \pm 10min$ lying within the valid space of time (lit, $[HCHO]_{sync}$ existent), the gradient has been calculated.

Three destruction processes have to be considered during these valid periods. The most important is the reaction with OH,

$$HCHO + OH \longrightarrow HO_2 + CO + H_2O$$
 (R3.4)

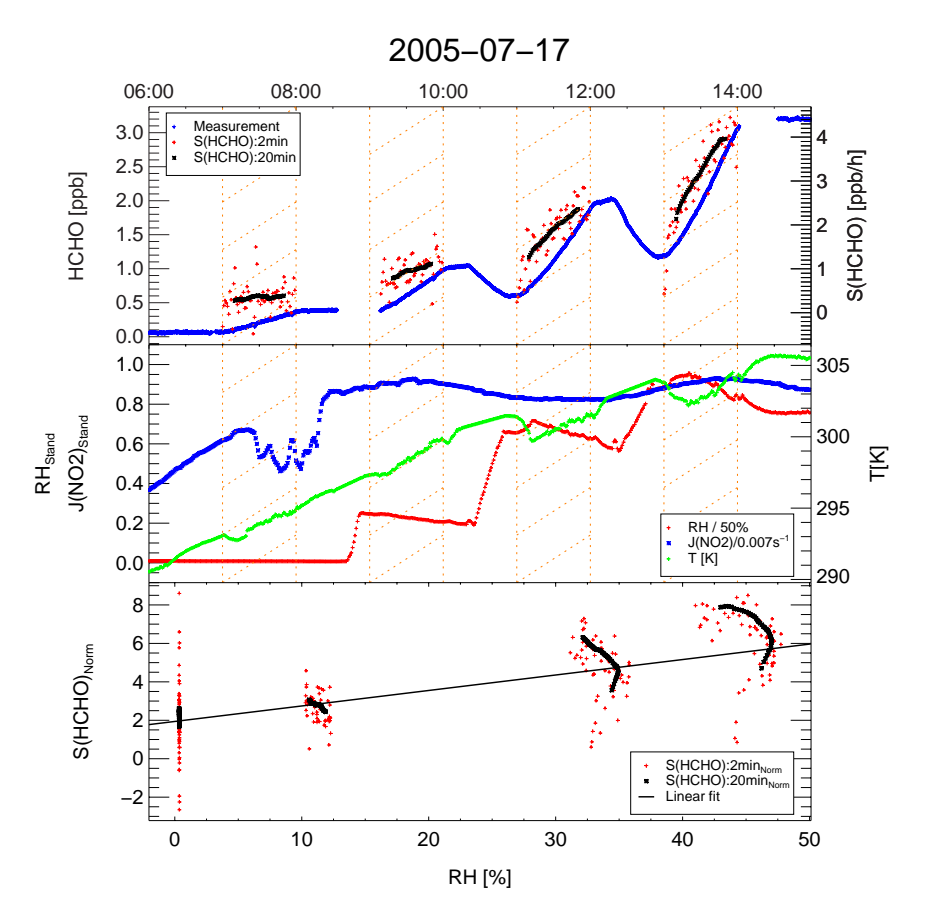


Figure 3.2: Water dependence of the SAPHIR HCHO source. In the upper panel, the measured concentration-time profile of HCHO and the production rate of HCHO, approximated by difference quotients for time step $\Delta t=2$ and by linear least square fit for $\Delta t=20min$, respectively, plus correction of the destruction processes (compare text), are plotted. The panel in the middle shows the three assumed influencing parameters relative humidity RH, NO₂ photolysis frequency $J(NO_2)$, and temperature T over time. The periods, when the chamber was lit, lie within the orange hatched areas. In the lowest panel, the two HCHO production rates, now normalized with the dry source strength of equation 3.4, are shown over RH. A clear correlation exists, which is outlined by the Pearson least square linear fit line of the 20min data also plotted in this panel.

followed by the two different photolysis reactions denoted as the molecular photolysis path, which makes up round 55% of the whole photolysis, and where molecules and no radicals are built,

$$\mathrm{HCHO} + h\nu \longrightarrow \mathrm{H}_2 + \mathrm{CO}$$
 (R3.5)

and the radical photolysis path, where two HO₂ radicals are built:

The third destruction process is the dilution by the replenishment flow. The velocities of the three destruction processes can be calculated from the measured quantities OH and formaldehyde concentration, photolysis frequencies, and replenishment flow, respectively. For the two minutes interval, the measured values were linearly interpolated to the t_i time pattern and were directly used. For the twenty minutes interval, the arithmetic means of the measured values were taken. Due to the temperature dependence of the rate coefficient $k_{R3.4}$, the same synchronizing and averaging process was done for the measured temperature.

The derived HCHO source strength is plotted in the upper panel (right axis) of figure 3.2. The red crosses show the two minutes values. They scatter a lot. The black stars, showing the 20 minutes averages, don't scatter that much, as expected. The source strength rises up to 4ppb/h, when the temperature is highest and the relative humidity is high. The temperature T, relative humidity RH, and NO_2 photolysis frequency $J(NO_2)$ variation in time is plotted in the second panel of figure 3.2, where all parameters are grouped, which are guessed to influence the source strength. The photolysis frequency is nearly constant in the last three lit periods, thus can not explain the huge variation of the source strength. Air temperature and relative humidity show the same trend from period to period, but do not describe a big rise within each period, as the source strength does. Quite the contrary is the case for the relative humidity, which declines due to the dilution within each period. Obviously, an hitherto unknown factor influences the HCHO source strength additionally. It is supposable, that the unmeasured foil temperature plays an important role, which most likely had a steeper temperature gradient than the measured inside air temperature, due to the special discontinuous way, this experiment was carried out. It also has to be pointed out, that the HCHO formation does not totally stop, when the roof is closed. Especially after the second and third illumination period, the HCHO continues to increase. The HCHO, which is built during the illumination, seems not to evaporate immediately into the chamber air, but needs some time. This memory effect of the foil is not analyzed further during this thesis.

To distinguish between the temperature and humidity dependence of the source strength, it was divided by the dry source strength given in equation 3.4. This normalized source is plotted against relative humidity in the lowest panel of figure 3.2. The red crosses once again represent the two minutes values scattering a lot, and the black stars show the 20 minutes averages. A clear positive correlation between the source strength and the relative humidity exists. The correlation line derived from the 20min averages is also plotted. The correlation line for the 2min values nearly yield the same axis intercept and slope and is not plotted for clarity reasons. The fitting and correlation parameters for both derivations are given in table 3.2. The definitions of the values given there can be found in appendix C.

The dry chamber source is nearly 1.9 times higher (axis intercept b of the fitting line) than the one of Karl 2004 [109], given in equation 3.4, derived from an experiment on 12th of June 2003. A dry source strength of this amplitude has been observed before (26th of May 2003), but was attributed to changes in the flushing of flaps around the steel girders inside the chamber. This is not the case for the experiment examined here. Thus, the long term stability observed between Aug 2002 and Sep 2003 seems not to continue till July 2005. That is not amazing, as a lot of experiments with different VOCs had been performed in the meantime. The correlation between the relative humidity and the source strength is rather high, as the high correlation coefficient r of 0.712 and even 0.927 for the two minutes and the twenty minutes averaging shows, respectively. The χ^2 goodness-of-fit test indicates, that the taken linear dependence is an acceptable choice: the values are the same order of magnitude or even smaller than the number of data points, although an unknown impact causes the source strength to rise within each illuminating period (as mentioned above).

Table 3.2: Fitting line and correlation parameters of the assumed linear HCHO source's water dependence: $S(HCHO) = m \cdot RH + b$. Given is the averaging time Δt , the standard deviation σ , the axis intercept b and the standard deviation of b: $\sigma(b)$, the slope m with its standard deviation $\sigma(m)$, the number of data points N, the correlation coefficient r, and the measure for the fitting quality χ^2 .

Δt	σ	$b \pm \sigma(b)$	$m \pm \sigma(m)$	N	r	$ \chi^2 $
2min	1.74	1.86 ± 0.5	0.066 ± 0.02	231	0.712	21.6
20min	0.78	1.84 ± 0.04	0.080 ± 0.003	155	0.927	117.8

Due to the fact, that the dry chamber source nearly doubled within two years, a change of the temperature and photolysis frequency dependence can not be ruled out. Thus, in the following, a closer look is taken at the standard experiments between June 2004 and Apr 2006, with at least HCHO Hantzsch, photolysis frequencies, relative humidity, temperature, pressure, replenishment flow, and OH (or $\rm NO_x$ and $\rm O_3$ to model the OH concentration) measurements were available.

The data were synchronized, averaged, and the source strength was calculated in the same manner, as described for the 17th of July 2005 experiment.

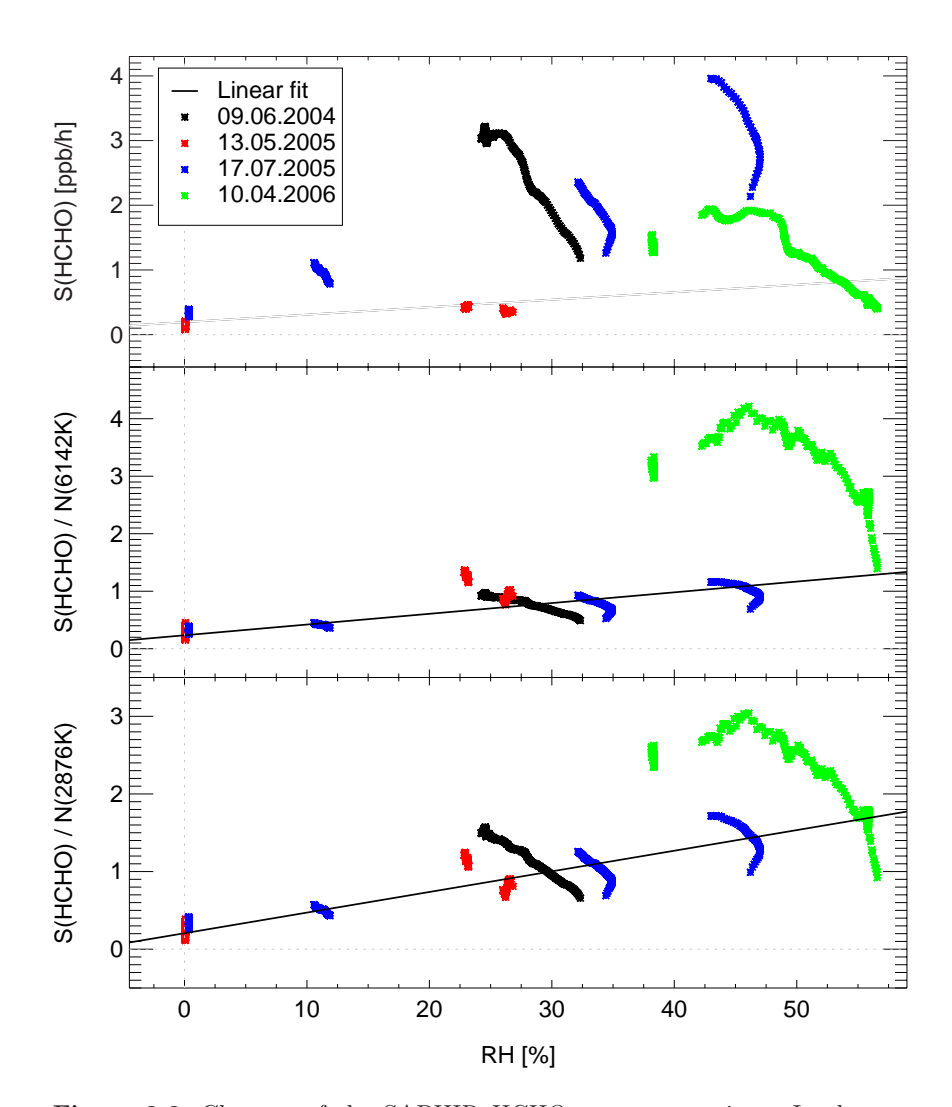


Figure 3.3: Changes of the SAPHIR HCHO source over time. In the uppermost panel, the unaltered HCHO source strength, calculated for four experiment days between Jun 2004 and Apr 2006, is shown over the relative humidity. There is no evidence for a linear correlation. In the two following panels, a normalization of this source strength via division by factor $N(T_0)$ of equation 3.7 is done. Now a correlation is observable, which is highest for $T_0 = 2876K$. Still unknown effects cause a remaining huge variance around the regression line.

The results for the 20 minutes averaging, yielding 649 data points, are shown in figure 3.3. In the uppermost panel, the unaltered source strength is plotted over the relative humidity. The different experiment days are well-defined by the different colors. The weighted linear least square fit line is also shown. This figure stresses the necessity, to deduct the temperature and photolysis frequency dependencies, to examine the influence of the relative humidity, as no correlation can be seen (r=0.39) in this plot. In the second panel, the source strength is divided by a normalized dry source strength deduced from equation 3.4. The normalization is done, to make the dimensions in this and the bottom panel concise. It corresponds to a division by the factor

$$N(T_0) = \frac{J(NO_2) \cdot \exp(-T_0/T)}{\overline{J(NO_2)} \cdot \exp(-T_0/\overline{T})},$$
(3.7)

where \overline{T} stands for the mean temperature over the four experiment days, which was 293K, and $\overline{J(NO_2)}$ for the mean NO₂ photolysis frequency (4.13 · $10^{-3}sec^{-1}$). Three of the four days seem to show a correlation now, but the last experiment carried out in Apr 2006 seems to be an outlier with elevated values. Hence, with r = 0.77 only a slight correlation for all days is found. A maximal correlation of 0.82 can be achieved with the choice of $T_0 = 2876K$, shown in the bottom panel. The goodness of fit test $\chi^2 = 2424$ indicates, however, that a linear dependence of the source strength from the relative humidity, together with the already known temperature and photolysis frequency dependence, do not fully describes the real source. An underestimation of the measure errors and their propagation can be precluded, as the identically obtained error estimates for the single day 17th July 2005 yield an even smaller χ^2 as the number of data points, which can among other things be traced back to inflated error estimates.

Discussion

The analysis of the SAPHIR HCHO source above shows, that in addition to the temperature and NO₂ photolysis frequency dependence, also a water dependence of the source strength exists. In opposition to the period between Aug 2002 and Sep 2003, a high variability of the source strength occurred between Jun 2004 and Apr 2006, resulting in an up to nearly a factor four higher dry source compared to the experiment on 16th of Sep 2003. Secondary, the temperature dependence seems to have changed, but this could not be confirmed by a correlation analysis, as not enough data with a great enough temperature range were available for the dry chamber within this period. It only could be shown for the combination of dry and humid experiments, but with no good fitting result, as the high χ^2 showed. This indicates, that not only statistical errors cause the deviations from the fitted regression line, but that yet uninvestigated processes dominate the differences. Hence, giving an empirical formula for the humid HCHO source strength is done, just to provide a more sophisticated estimation (factor 2 uncertainty) for the humid chamber between 2004 and 2006, as an improvement compared to taking the dry HCHO chamber source only:

$$S_{HCHO}(J(NO_2), T, RH) \approx 3.1 \cdot 10^{13} cm^{-3} \cdot J(NO_2) \cdot \exp\left(\frac{-2876K}{T}\right) \cdot (0.21 + 2.6 \cdot 10^{-2} \cdot RH)$$
 (3.8)

The units for the input parameter are sec^{-1} for the photolysis frequency $J(NO_2)$, K for the temperature T and % for the relative humidity RH. The source strength S_{HCHO} is given in $cm^{-3} \cdot sec^{-1}$, then.

As the building process in general, the reason for the found long term changes of the source strength are unclear. According to this, the results stress the imperative to constantly carry out standard experiments and monitor the HCHO source. Especially when the SAPHIR foil is exchanged in Nov - Dec 2007, new and ongoing examinations of VOC wall sources have to be done.

3.1.4 Background Reactivity

Beside the known trace gases HONO and HCHO, which are emitted from the illuminated walls, and despite the fact, that the chamber is constantly flushed with high purity synthetic air, still unknown trace constituents reside inside it. Their existence become manifest in the elevated ozone production compared to the ozone production just caused by the formaldehyde. As described in chapter 2.1, ozone is produced, when $\rm HO_2$ or $\rm RO_2$ reacts with NO to build $\rm NO_2$, which is photolyzed, and the separated oxygen radical combines with an oxygen. The elevated ozone production therefore requires the creation of $\rm HO_2$ or $\rm RO_2$ radicals. On their part, these radicals are mostly built during the reaction of an OH radical with any VOC or CO. That's where the term "background reactivity" (BR) comes from, as it is supposed, that unknown background compounds show an reactivity towards OH.

In chemical models describing the gas phase chemistry inside the chamber, the simplest way to represent this background reactivity is to introduce an additional reaction of an unknown substance Y with OH yielding HO₂:

$$Y+OH \longrightarrow HO_2$$
 (R3.7)

To make the influence of this reaction comparable to other reactions, the rate coefficient of this reaction is equated with the rate coefficient of CO with OH, so that the strength of the background reactivity is given in CO equivalents. A notional Y of 200ppb, a quit normal value for the SAPHIR chamber, denotes, that unknown background species inside cause the same ozone production, as 200ppb additional CO would cause.

3.1.5 Other Sources

During a standard experiment at the 31st of Aug 2006 also formic acid (HCOOH), acetaldehyde (CH3CHO), a precursor of PAN, which has been detected, too, were found to form inside the chamber. The chamber was illuminated for

about 6 hours. The experiment was started with dry air. After about 2.5 hours, with the SAPHIR roof left open, the chamber air was humidified to about 50% relative humidity. The measured concentrations of HCOOH and CH3CHO by the PTR-MS instrument, of PAN by the GC-ECD system, and of NO_x by the CL detector (the instruments are described in chapter 3.2) are shown in figure 3.4. The formic acid reaches up to 4ppb and the acetaldehyde up to 2ppb at the end of the illumination phase. NO_x , which is an indicator for the chamber HONO source, reaches around 2ppb, too. With its precursors acetaldehyde and NO_x present, the secondary trace gas PAN is photochemically built inside the chamber and reaches up to 300ppt. This was the first time, PAN was detected during a standard experiment at SAPHIR.

Although the humidification was done with a purge flow of around $270m^3/h$ for 46 minutes, which normally causes each trace constituent to be diluted to about half of its former concentration, HCOOH, CH3CHO, and NO_x do not show any decrease. In contrast, their concentrations are rising. Just assigning this rise to the water dependent source strengths is not sufficient, as during the humidification the sources have to compensate for the strong dilution additionally. When the purge flow stops and the humidity is comparatively constant, the net production, visible in the concentration time profile gradient, is not elevated compared to the phase with the strong dilution. The only plausible explanation for the rising HCOOH, CH3CHO, and NO_x levels are hence, that the injected water vapor contained impurities of the detected organic species and HONO, which immediately photolyzes inside the chamber (reaction R3.1) and rises the NO_x level. HONO impurities of several hundred *ppt* introduced by the humidification have also been measured directly in the dark chamber [110].

3.1.6 Deposition at the Walls

Although the surface to volume ratio of the SAPHIR chamber is rather small, some water soluble species like N_2O_5 , HNO₃, HONO, H_2O_2 , HO₂, and O₃ can deposit at the chamber walls [109]. The lifetime against wall deposition is about three days. In a chemical mechanism, the wall deposition of a specie X is represented by a simple first order loss:

$$X \longrightarrow (R3.8)$$

The rate coefficient for these reactions k_{dep} is about $3.9 \cdot 10^{-6} sec^{-1}$.

3.2 Instrumentation

A simulation chamber like SAPHIR would be worthless, if no extensive set of instrumentation is operated to measure trace gas concentrations and the driving force solar radiation. A comprehensive compilation of these and other measuring techniques in atmospheric chemistry can be found in *Clemitshaw* 2004 [111]. The instruments, which were involved in the experiments dealt

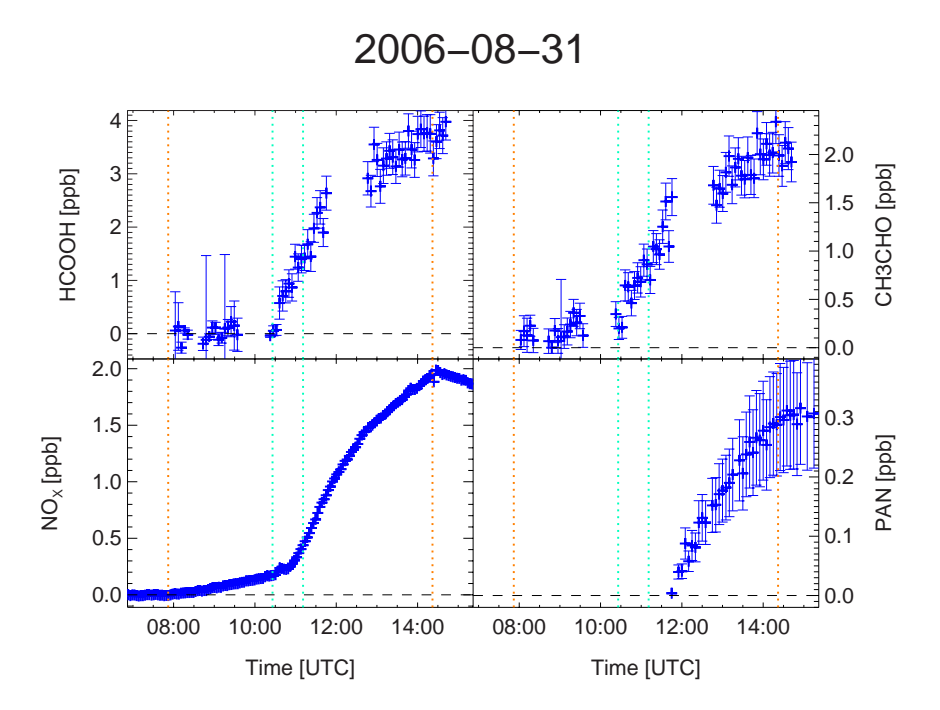


Figure 3.4: Other trace gases found during the standard experiments at the 31st Aug 2006. Shown are the concentration time profiles of formic acid (upper left), acetaldehyde (upper right), both measured by the PTR-MS instrument, NO_x, measured by the CL detector, and PAN, measured by the GC-ECD. The chamber roof was open between the times marked with orange hatched lines. A humidification took place during illumination between the both bright blue hatched lines. Acetaldehyde reaches up to 2ppb, formic acid even 4ppb. The rising NO_x serves as the indicator for the chamber HONO source. From the precursors NO_x and acetaldehyde, also the secondary trace gas PAN is photochemically built, which reaches up to 300ppt. Although the purge flow with round $270m^3/h$ was used for the humidification, all shown primary trace gases show now dilution at all, but rather an increase. Impurities of the introduced water are hold responsible for that. Additionally, the production rates of the primary gases are increased in the humid compared to the dry chamber air.

with in this thesis, are briefly described in the following. An overview, including sampling and repetition time, precision² and accuracy³ specifications is provided in table 3.3 at the end of this chapter.

3.2.1 Ozone Measurements

Since Feb 2006 ozone measurements at the SAPHIR chamber are performed with two different methods, by ultraviolet absorption and, newly established, by chemiluminescence. Both methods perfectly correlate.

Ultraviolet Absorption Detector (UV-A)

The ultraviolet absorption device is a standard commercial instrument (Ansyco, ozone analyzer 41M). It uses the ultraviolet absorption of ozone at 254nm. Therefor a mercury emission lamp is used as a light source and two evacuated photo-tubes as detectors. One just monitors the emission intensity of the mercury lamp as a reference, the other one is located behind the sample cell to measure its transmission coefficient. This transmission coefficient is measured for the original sampled air and for sampled air, where the ozone is eliminated by an ozone scrubber. Every ten seconds it is switched between these two ways, and the ozone concentration can be calculated from their transmission ratio using the Beer-Lambert law, given e.g. in Bossmeyer 2006 [93].

Chemiluminescence (CL) Ozone Detector

The chemiluminescence ozone detector works just as the NO, NO₂ CL detector described below (chapter 3.2.4), with the chief difference, that excess NO is added to the ozone containing sample air to produce excited NO₂* molecules [112]. The signal of the photomultiplier tube, where the photons emitted during the relaxation of the exited molecules are detected, is about s=1000cps per ppb ozone. The sampling interval Δt is 20sec. The CL ozone detector has to be calibrated with the help of an independent ozone measurement, which is provided by the UV-A detector [110].

3.2.2 Reactive Species

Due to their very low concentration of some 10^6 radicals per cm^3 during daytime, hydroxyl radicals are hardly to detect. Two physical techniques, which utilize the strong absorption lines of the OH radicals e.g. at 308nm, are installed at the SAPHIR chamber. An intercomparison between these two instruments was carried out in 2003, and the results are published by *Schlosser* et al. 2007 [113].

²Precision, also called reproducibility or repeatability is a measure for the probability, that the iteration of the same measurement yields the same or similar results. It is given by the standard deviation σ of repeated measurements.

³Accuracy is a degree of conformity of the measurement to the true value. It is mainly influenced by systematic errors.

Differential Optical Absorption Spectroscopy (DOAS)

The main principle of DOAS instruments is, to send laser pulses of known intensity and with a fixed matching wave length (308nm) for the detection of OH radicals) along a path through the air of interest. At the end of this optical path, the intensity of the laser pulse, which is not absorbed or scattered along the way, but travels through the air, is detected. Simply spoken, the ratio between send and received laser pulse intensities allows the calculation of the trace gas density following Beer-Lambert law. To get a high enough signal to noise ratio, a long optical path is required. In the limited SAPHIR chamber this is obtained by a modified multiple reflection cell with a base length of 20m, which is traveled 112 times, making a path length of 2.240km. The advantage of the DOAS technique is its good accuracy, as it depends on the absorption cross sections of OH and the given errors for this values only.

Not only OH can be measured by the SAPHIR DOAS instrument, but also formaldehyde, naphthalene, and SO₂. A detailed description of the DOAS instrument can be found in *Hausmann et al.* 1997 [114] and *Dorn et al.* 1995 [115], with some specifications updated by *Schlosser et al.* 2007 [113].

Laser Induced Fluorescence (LIF)

The LIF detection scheme, also called Fluorescence Assay by Gas Expansion (FAGE), is widely accepted on account of its higher precision, better time resolution, and compact construction (no long optical path length is needed) compared to the DOAS technique. In contrast to the DOAS instrument, which measures the mean value of a long path length, the LIF instruments detects rather small regional air samples. This difference however does not concern measurements in the well mixed SAPHIR chamber. One main disadvantage is the high effort of calibration.

To measure OH with the LIF technique, ambient air is expanded through a small nozzle into a low-pressure (3.5hPa) detection chamber called fluorescence cell. The resulting gas beam is irradiated rectangularly by 308nm laser light, which excites the OH radicals. The OH resonance fluorescence light between 307 and 311nm is detected by a gated photon counter perpendicular to the laser and gas beam. Scattered laser and solar stray light cause a background radiation inside the fluorescence cell. Hence, an on- and off-resonance tuning cycle is performed, and the background can be subtracted from the measurements. A detailed description of the first FZJ LIF instrument is given by Holland et al. 1995 [116]. Since the 1990s the instrument has been further improved, including the addition of a second detection cell for the simultaneous measurement of HO₂ radicals after conversion to OH via the reaction R2.18 with added excess NO [117]. The latest progress of the FZJ LIF instrument is the development of a system with an additional reactor cell, where RO₂ radicals are converted to HO₂ radicals via reactions R2.22 and R2.23. The HO₂ radicals are subsequently converted to detectable hydroxyl radicals [97]. Thus, the LIF technique is used to detect RO₂ radicals.

3.2.3 Volatile Organic Compounds

For the detection of selected species out of the huge family of VOCs and OVOCs, a couple of instruments are used at the SAPHIR chamber. Gas chromatography and proton-transfer-reaction mass spectrometry (PTR-MS) are two quite common techniques, which are, among others, operated at SAPHIR. A comparison of advantages and disadvantages of instruments of this kind can be found in *Warneke et al. 2004* [30].

Gas Chromatograph (GC), VOCs up to C₁₀

Two different gas chromatographs are operated at the SAPHIR chamber. Air samples for both GCs are taken one meter above the chamber floor using a stainless steel inlet line covered with FEP. The supply of air is done via a heated (330 K) stainless steel sampling line (8mm inner diameter, $\approx 10 \text{m}$ length).

One GC is a commercially available system with a flame ionization detector (FID) and a cryo focus module by Chrompack International BV. Various rebuilding and improvements of the Chrompack GC were realized to enhance the separation and detection of "simple" NMHCs like alkanes and alkenes. These improvements are described in detail by *Rodriguez Bares 2003* [94]. Before the sample air can be transferred to the capillary column (fused silica, Al_2O_3 , KCl deactivated), it has to pass couple of preconditioning steps, e.g. to remove water and CO_2 , and perform a pre-concentration. This is achieved by a elaborate combination of cooling traps and absorption tubes, temporarily flushed with ultra pure helium, which can be cooled and heated and thus can follow a well adjusted temperature time profile. Finally, at the capillary column, the VOC peaks are temporally separated and, when they elute from the GC's column, are detected with the FID. As the name already indicates, this kind of detector burns the VOCs and measures the current induced by the produced ions.

The second GC in use is designed for the separation and detection of OVOCs, e.g. alcohols and aldehydes. It's a dual-column (DB5 and Porabond Q column) gas-chromatograph with cryo focus module and two flame ionization detectors (Perkin-Elmer). The sample air has to pass some preconditioning steps comparable to the ones for the Chrompack GC. Additionally, O₃ in the sample air is depleted by added NO. The first column serves to separate species of interest, e.g. aldehydes, which are directed to the second column for further separation and analysis.

Proton Transfer Reaction - Mass Spectrometry (PTR-MS)

As the Chrompack GC, the PTR-MS instrument is a commercially available instrument (Ionicon Analytic, Austria). It consists of three main components. Within a (1) hollow cathode ion source, H_3O^+ ions are produced from pure water vapor. These primary ions pass into the (2) drift tube via a venturi type inlet. There the protons transfer to the VOCs that are to be detected. Only VOCs which have a higher proton affinity than water (7.22eV) take up a proton and can be detected with a (3) quadrupole mass spectrometer finally

[118]. During the proton transfer process, the VOCs are partly fractured into specific fragment pattern, which are also detected. These fragments have to be traced back to their source VOCs, which is not unique in all cases.

Hantzsch Monitor, HCHO

With the Hantzsch Monitor formaldehyde can be detected via a wet chemical analysis. Therefor the HCHO of the sampling air is transferred into the aqueous phase via a stripping process as a first step. Then the Hanztsch reagent is added, which contains acetylacetone, acetic acid and ammonium acetate. The reagent reacts with HCHO building a fluorescent dye, which is excited by 410nm radiation. The resulting fluorescent light is detected in the yellow spectral range at 510nm [119].

3.2.4 NO_y Species

Chemiluminescence NO, NO₂ Detector (CL)

The NO_x CL instrument at SAPHIR [120] detects NO and NO_2 separately. NO is detected photometrically with the help of the chemiluminescent reaction with added excess O_3 producing excited NO_2^* and NO_2 (reaction R3.9 and R3.10) within a reaction vessel. The excited NO_2^* emits a photon in the given wavelength band or is quenched to the ground electronic state by other species M_i (reactions R3.11 or R3.12 respectively):

$$NO + O_3 \longrightarrow NO_2^* + O_2 \tag{R3.9}$$

$$\longrightarrow NO_2 + O_2$$
 (R3.10)

$$NO_2^* \xrightarrow{M} NO_2 + h\nu \text{ (600nm} < \lambda < 2800\text{nm})$$
 (R3.11)

$$NO_2^* + M_i \longrightarrow NO_2 + M_i$$
 (R3.12)

The number of the resultant photons, which are detected by a photomultiplier tube, is proportional to the concentration of NO. About s=2000cps per ppb NO are detected. The zero mode (noise) Z of the photomultiplier makes about z=100cps. The sampling interval Δt is 20 seconds.

 NO_2 is measured in the same way after it is photolyzed to NO with a broadband arc lamp. The conversion efficiency amounts to c=50%. Thus, in the "light" mode L, the signal of the ambient NO plus $c \cdot NO_2$ is detected. Calibrations are performed on a gas mixture standard regularly.

Long Path Absorption Photometer (LOPAP), HONO

The LOPAP instrument is a commercially available instrument, which combines wet chemical sampling and photometric detection for the measurement of nitrous acid [121]. In a first step, gaseous HONO is stripped from the sample air into the liquid phase, originally consisting of hydrochloric acid and sulfanilamide. With HONO this sulfanilamide immediately forms a special salt. After debubbling, the solution is pumped into a second cell called azo dye

unit, where a chloride solution is added to form the final dye. The mixture is pumped into the detection unit, a so-called liquid core waveguide. It consists of a teflon tubing, where visible light is focused into. At the end of the tube, the absorption spectrum is detected. The instrument is operated with two identical, serial channels, one to analyze the air sample, the other one, driven with almost HONO freed air, serves as a reference to check for interferences. The instrument is calibrated with a liquid nitrite standard regularly.

Gas Chromatography with Electron Capture Detector (GC-ECD), PANs

To establish a permanent detection of peroxyacyl nitrates at the SAPHIR chamber was provoked by the research done during this thesis. Due to the thermal instability of the PANs, a special gas chromatograph is used for the separation of the trace gases. An electron capture detector [122], which is sensitive for compounds with a high electron affinity like nitrates, halogenated and sulfurous compounds, is used for the identification. The system has been used in field campaigns before [123]. The instability of the PANs complicates the calibration of the instrument, as no gas standards out of a gas bottle can be used, but an in situ production of a well defined amount is necessary. For example, PAN is made by photolyzing acetone to get peroxyacetyl radicals and mixing it with a known amount of NO, which are oxidized to NO_2 by the peroxy radicals. Remaining peroxyacetyl radicals and the built NO_2 form PAN subsequently:

$$CH_3C(O)CH_3 + h\nu \xrightarrow{O_2} CH_3C(O)OO + CH_3OO$$
 (R3.13)

$$CH_3C(O)OO + NO \longrightarrow CH_3C(O)O + NO_2$$
 (R3.14)

$$CH_3OO + NO \longrightarrow CH_3O + NO_2$$
 (R3.15)

$$CH_3C(O)OO + NO_2 \longleftrightarrow CH_3C(O)OONO_2$$
 (PAN) (R3.16)

In the case of MPAN, no calibration of this kind is possible. Hence the calibration factor for PAN, adjusted according to the detection ratio given in *Flocke* et al. [124], is used.

3.2.5 Photolysis Frequencies

Photolysis frequencies inside the SAPHIR chamber are derived from spectral-radiometer (SR) measurements of the solar actinic UV flux (scalar intensity) outside the chamber on the roof of the neighboring building. The scalar intensity $F_{\lambda}(\lambda)$ is defined as the integrated spectral photon radiance $L_{\lambda}(\lambda)$ over all angles of incidence $(0 \le \vartheta \le 180^{\circ})$ and $0 \le \varphi \le 360^{\circ}$:

$$F_{\lambda}(\lambda) = \int_{\vartheta'} \int_{\varphi'} L_{\lambda}(\lambda, \vartheta, \varphi) d\varphi' d\vartheta'$$
(3.9)

The spectral radiometry instrument is based on a scanning double monochromator. The entrance optics, a special quartz diffuser connected to the entrance slit by a flexible optical quartz fiber bundle, exhibits an isotropic angular response over a solid angle of 2π sr. The spectra are measured between 280 and 420nm, the relevant range for most of the tropospheric photolysis processes, with an 1nm resolution [125]. The sprectralradiometers are also used in field campaigns, e.g. described in Kraus and Hofzumahaus 1998 [126] and Bohn 2006 [127].

With the help of a complex model, which factors the transmission properties of the teflon foil and the shadows of the steel construction in, the actinic flux inside the SAPHIR chamber is calculated [91]. The model has been tested against chemical actinometry, where the whole SAPHIR chamber was used as the photo reactor cell for NO_2 [92].

If the spectral actinic flux $F_{\lambda}(\lambda)$ is known from the measurements, the photolysis frequency $J_{i,j}$ of a specie i can be calculated following equation 3.10, if its absorption cross section σ_i and the quantum yield ϕ_j of its photoproducts j are known:

$$J_{i,j} = \int \sigma_i(\lambda)\phi_j(\lambda)F_\lambda(\lambda)d\lambda \tag{3.10}$$

3.2.6 Meteorological Conditions

The meteorological conditions relative humidity and temperature are measured inside the SAPHIR chamber with standard instruments, a dewpoint hygrometer and an ultrasonic anemometer, respectively. The pressure is derived from outside measurements conducted by the meteorological office of the Forschungszentrum Jülich.

Table 3.3: Overview of the instrumentation at the SAPHIR chamber. Only the instruments which contributed data to this work are listed. The values given for the accuracy and precision may only be used for a rough estimation. They can vary from specie to specie, if more than one can be detected with the instrument, on the demand interval, and due to changes in e.g. the quality of used standards for the calibration or the laser performance. The real precision and accuracy values, which have to be used in the analysis of the experiments, are calculated and provided by the operators separately for each single data point.

Instrument	Species	Measurement Acquisition Accuracy Precision	Acquisition	Accuracy	Precision	Operators
		interval	time			
UV-A	O_3	40sec	80sec	<3%	1ppb	F. Rohrer, M. Müsgen
O ₃ CL	O_3	30sec	60sec	<2%	10ppt+0.5%	
NO_x CL	NO, NO_2	40sec	160sec	5%	3ppt+0.5%	
DOAS	НО	135sec	3min	< 6.5%	$1.25 \cdot 10^6 \text{cm}^{-3} \text{ at LoD}$	$1.25 \cdot 10^6 \text{cm}^{-3}$ at LoD HP. Dorn, E. Schlosser, R.
						Häseler, T. Brauers
	HCHO	135sec	3min		$10^{10} cm^{-1}$	
Chrompack GC	NMHCs	30min	50min	10%	4ppt+5%	R. Wegener
Perkin-Elmer GC	OVOCs	30min	50min	10%	20ppt+5%	
PTR-MS	VOCs		1min	3%	300ppt	R. Tillmann
Hantzsch	HCHO		2min	2%	10ppt	
LOPAP	HONO	30-60sec	5min	10%	3ppt	R. Häseler
GC-ECD	PANs	10sec	10min	20%	20ppt	A. Volz-Thomas, N. Houben,
						M. Berg, HW. Pätz
SR	J	120sec	120sec	13%	< 0.1%	B. Bohn

4 Ozone Production Due to Isoprene Degradation

In the introduction it has already been mentioned, that environmental chamber experiments are essential for atmospheric chemistry research. To really understand the complex processes influencing the chemical composition of the atmosphere, field campaigns in different regions with, for example, dominant anthropogenic or biogenic sources or different climatological conditions, are obligatory, too. To distinguish between the physical (meteorological) influences, which can be transport, mixing, sources or sinks of trace gases, and the photochemical conversions, a sophisticated set of measuring instruments is necessary. The data derived by these instruments act as input variables for different model and simulation approaches to calculate the in situ photochemical processes. Differences between the calculated photochemical and measured trace gas progresses can be attributed to the physical factors, then.

In this chapter, three different approaches to determine the net photochemical $O_x = O_3 + NO_2$ production $d[O_x]/dt$ were tested against SAPHIR chamber experiments with ambient concentrations of NO_x and isoprene and its degradation products MACR and MVK, respectively. Due to the chamber features of SAPHIR, the studies were restricted to a NO_x regime of above about one ppb. Lower NO_x concentrations could only be reached in a short time period at the beginning of the kind of experiments, where no extra NO_x was intentionally added. In the course of these experiments, the chamber HONO source quickly causes the NO_x concentration inside the chamber to rise in the order of some 10th of a ppb/h, until the NO_x production is balanced by dilution and other NO_x loss processes. The upper limit of the studied NO_x regime was about 20ppb. The study of higher NO_x levels up to the highest levels observed in field experiment (about a hundred ppb in big cities) would be possible in the SAPHIR chamber, too, but no other chemical effects are expected than already dominating the chemistry at the 20ppb level.

No transport processes take place in the chamber, and the sources and sinks are very well characterized compared to field campaigns. Due to the ambient conditions, only chemical reactions, which are relevant in the natural tropospheric atmosphere, are of importance during the chamber experiments. Presuming the studied approaches to be correct, hence simple corrections accounting for the chamber features, described in the previous chapter, should suffice to bring the calculated $d[O_x]/dt$ in correspondence with the measured O_x progress. In short, the approaches, which highly vary in the computational effort, needed measured input, and produced output, are:

Fully time dependent MCM model run Beside continuously prescribing the

meteorological conditions (temperature, pressure, relative humidity and photolysis frequencies), only initial concentrations of the trace gases are used as an input. The further course of all trace gas concentrations are computed completely. In principle, the time resolution of the output is restricted just by memory and accuracy limitations of the used computer.

First degradation step approach For each measured VOC and CO, the degradation velocity is calculated with the help of OH and photolysis frequency measurements. Amplifying factors deduced from the MCM are multiplied with the degradation rates to gain the O_x progress. Production rates can only be calculated for points of time, where at least measurements of the most important trace constituents are available. For biogenic dominated air masses, isoprene and its degradation products MACR, MVK, and HCHO count as being of importance. In the case of VOC measurements by GC instruments, the time resolution of one to two data points within an hour is quite poor.

OH lifetime approach Measurements of the OH lifetime and the OH concentration are combined with an integrated amplifying factor to approximate the photochemical O_x production. The demand interval of this approach matches the one of the OH lifetime instrument.

In the following subsections 4.1 - 4.3, first of all the approaches are described in detail and are individually tested. To finally compare the chemical forecasting capabilities of each approach in subsection 4.4 independent of the different time resolutions, the measured and calculated data were preprocessed in the same way to make them conform with the first degradation step (FDS) approach. As indicated above, the FDS approach uses GC measurements as input and therefore has the lowest time resolution of all three approaches presented, as the GC needs a half an hour GC's sampling time and hence provides half an hour mean values as measuring points. All the values compared, in particular the net O_x progress, were averaged on these half an hour sampling periods given by the GC measurements. To derive the experimental net O_x production dO_x/dt of a day, therefore first of all the NO₂ and O₃ measurements were interpolated upon a common 60sec equidistant time pattern to built the sum of both interpolated series to get O_x. Then, a weighted linear least square fit (compare chapter 3.1.3) was used to get the mean O_x production within the half an hour GC sampling time from the gradient of the fitting line. Although the O_x production is by no means a linear process, the straight fitting lines represent the O_x concentrations quite well, which is demonstrated in figure 4.1. A correction concerning the dilution of all trace gases was done by using the arithmetic means of the O_x concentration and the replenishment flow during the GC sampling period to calculate a mean dilution rate.

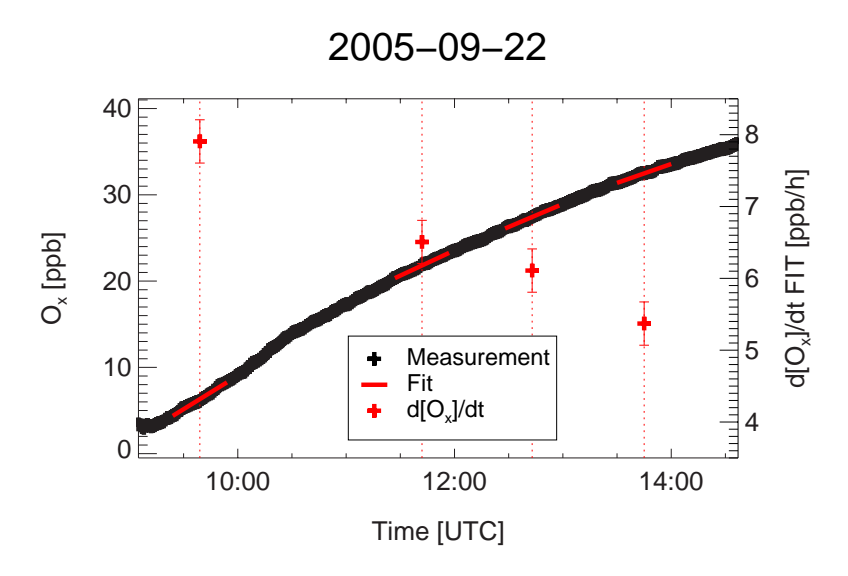


Figure 4.1: O_x fitting lines at GC sampling times shown for the illumination phase of the isoprene degradation experiment from the 22nd Sep 2005 at SAPHIR. The half an hour (red) fitting lines represent the measured O_x course (black crosses) very well, although the processes dominating the O_x production are by no means linear. The times with GC measurements present are marked with hatched lines. The net production rates derived from the gradient of the fitting lines are given with red crosses referring to the right y-axis.

4.1 Fully Time Dependent MCM Model Runs

The Master Chemical Mechanism MCM is a nearly explicit mechanism, which compiles the current understanding of the tropospheric gas phase chemistry. Not all of the used reactions, e.g. their product yields or rate coefficients, have been derived experimentally, but a lot of theoretical and analogy assumptions are applied. Experimentally as well as otherwise obtained parts of the mechanism are subject to errors. Simply presuming the "correctness" without questioning the modelled data would hence be credulous. Tests of the whole compilation as well as of subsets are necessary, therefore, to evaluate the accuracy of the MCM and especially its $O_{\rm x}$ production prediction capabilities. As the definition of initial concentrations and of a starting point of time for the modelling are not unique anyway for field campaigns, the presented study only elucidates the MCM model performance if all boundary conditions for the model are known accurately, what nearly is the case for the SAPHIR chamber.

The entire MCM has already been tested in atmospheric models and through intercomparison with the results of chamber validated mechanisms [128, 39], but only a few studies exist, where parts of the MCM were directly tested against experimental chamber data: photo-oxidation of α -pinene:NO_x mix-

tures [77], different aromatics: NO_x mixtures [129, 130] in the European Photoreactor EUPHORE, and NO_3 induced degradation of aldehydes in the SAPHIR chamber [86]. The MCM v3 isoprene mechanism was as well tested against experimental environmental chamber data

- of the SAPRC indoor chambers [131] concerning precursor decay rate, ozone production, PAN and carbonyl product formation by *Pinho et al.* 2005 [63] and
- 2. of the SAPHIR chamber concerning the yield of the isoprene oxidation products MACR and MVK by *Karl et al. 2006* [96].

The VOC and NO_x concentrations in the study of $Pinho\ et\ al.$ were high above ambient levels (starting conditions: 270-1000ppb isoprene, 150-600ppb NO_x). Due to these high concentrations it was supposed, that reactions with the ground state oxygen atom $O(^3P)$ became relevant and were introduced into the mechanism. Additionally, photolysis parameters for HCHO, MVK and MACR were adjusted to enhance the agreement with the SAPRC chamber data. In the second study by $Karl\ et\ al.$, the isoprene degradation yields of MACR and MVK showed to be underestimated by the MCM for ambient conditions (isoprene: 2-5ppb, NO_x : 0.3-3.6ppb, ozone: 40-42ppb).

Consequently, the MCM isoprene degradation has not been tested concerning ozone production against chamber experiments with ambient conditions until now. Moreover, the previous studies mentioned above already showed inadequacies of the MCM model in some aspects.

In a first series of four experiments during Sep 2005 (experiment parameters are listed in appendix B, table B.2), the MCM isoprene model O_x production predictions were tested against photochemistry experiments in the SAPHIR chamber. In principle, all experiments were carried out in the same manner. Over night, the chamber was flushed with synthetic air, until the NO_x concentration was diluted below the LoD. With the roof still closed, first of all the chamber air was humidified. Then, the trace gases NO_2 and isoprene were added. One sampling period of the GC was awaited (30 - 50min), and thereafter the roof was opened.

The realization of the first experiment differed in the point of time, the isoprene was added. This happened within the illuminating period, after the humid and $\mathrm{NO_x}$ containing air in the chamber already had processed for 3.5 hours. The fourth experiment also was realized slightly different. The humidification and the adding of $\mathrm{NO_2}$ were done with the roof of the chamber opened. About 20 minutes later, the roof was closed, and isoprene was added. After the first sampling period of the GC, the chamber was illuminated again.

The starting values for isoprene laid between 3.5 to 10.4ppb, thus within the same order of magnitude as the upper limit of values measured in field experiments. NO_x concentrations varied between 2.5 and 6.8ppb, representing rural to slightly polluted areas. Standard experiments were carried out before and after the isoprene campaign.

4.1.1 Results

Contrary to previous experiences, the SAPHIR chamber showed a high variance in the HONO source, which had been adjusted to the measured NO_x trend. In the standard experiments before (20th Sep) and after (28th Sep 2005) the isoprene campaign, its scaling factor K of equation 3.3 changed from 7.1 to $20.7 \cdot 10^{13} cm^{-3}$, a factor three so.

The background reactivity (BR) showed an uncommonly high variability, too, but with the contrary trend, namely decreasing from 500 to 120ppb CO equivalents. No common explanation (flushing out versus intrusion of any impurity) for the HONO source and background reactivity hence is reasonable.

For the MCM-isoprene-model runs (the isoprene subset of the MCM is given in appendix A.4) therefore, the HONO source was scaled manually to best fit the measured $\mathrm{NO_x}$ developing. A manual fitting was regarded sufficient, as due to the huge variance from day to day no constant HONO source within one day could be presumed anyway. The scaling factors K of equation 3.3 found were 2.4, 3.3, 9.4, and 8.5 $\cdot 10^{13} cm^{-3}$ for the experiments on 21st, 22nd, 23rd, and 26th Sep 2005, respectively. No intrusion of HONO with the humidification of the chamber air, which had been observed in former experiments some times [132], was assumed. The HCHO source for the humid chamber was used as identified in chapter 3.1.3 (equation 3.8).

When testing the ozone prediction capability of the MCM, a tuning of the model background reactivity would result in the best possible modelexperiment conformance. Most probably, this conformance outmatches the pure MCM model run with the real background reactivity. For this reason, two "extreme case" model runs were performed for each day, one with zero background reactivity, hence the lowest possible value at all, and one with 600ppb CO equivalents, which exceeds the maximum value found during the standard experiments by 100ppb. Exemplarily, the results of the experiment of the 22nd Sep for some selected species during the illuminating phase are shown in figure 4.2. The O_x (combined UV-A ozone and CL NO₂ measurements), NO_x (CL), and OH (DOAS) measurements (black crosses) are quite well represented by both "extreme case" model runs (red line: no background reactivity, green line: 600ppb CO equivalents background reactivity). Even with no background reactivity applied, the total O_x yield is slightly overestimated at the end of the experiment. The gradient of the O_x time series, however, is shortly underestimated in the beginning, which soon is overcompensated by a following small overestimation of the production rate and a nearly parallel course of measurements and model runs in the following. Although the isoprene model concentration, whose initial value has been adjusted to the amount of liquid isoprene injected (see below), is overestimated by the model, the GC measurements of the first generation degradation products MACR and MVK are strongly underestimated. A difference between both model runs becomes evident not until the second half of the experiment. The isoprene is degraded in large part, then, and the OH concentration is no more dependent on the isoprene concentration, but on the background reactivity, as the rate of reaction $Y + OH \longrightarrow HO_2$ reaches and later on outreaches the order of magnitude of the C5H8 + OH \longrightarrow products reaction.

The impression received by just analyzing a single experiment proves true, when studying all four experiments. In figure 4.3, the zero and 600ppb BR model derived net O_x production rates in the left and right panel, respectively, are compared to measured rates. Therefore the measured and modelled time series of NO_2 and O_3 were preprocessed as described in the introduction of this chapter. (The interpolation onto a common equidistant time pattern is not necessary for the model data, of course). The data of the four days are color coded. The model runs show to underestimate low production rates, which mainly appear at the end of each experiment and to overestimate high production rates mainly emerging at the beginning. As expected, the model runs with the higher background reactivity yield higher O_x production rates. In the figure, this is evident by the up shift of all data points by data point specific values. This up shift is highest for the 23rd Sep 2005 experiment (green dots), which was the experiment with the lowest initial isoprene concentration and therefore the highest sensitivity towards the BR model parameter.

To allow for a weighted linear least square fit of the data set, error estimates were defined for the modelled data. Due to the uncertainty in adjusting the HCHO and HONO chamber source strength and thus the primary OH production, and due to the precision of the meteorological conditions used as an input, a relative error of 20% is applied. As a HONO impurity of the humidification water can not be excluded and initial errors may accumulate over the experimental course, a bias of 1ppb/h is assumed. The correlation parameters for the zero and 600ppb BR model runs are summarized in table 4.1. A quite high correlation r of 0.9 and 0.85, respectively, exists. The slope of the fitting line does not differ from one significantly, which lies within the 2σ confidence interval of the fitted slope. The axis intercept heavily varies with the changed background reactivity, which is the expected behavior, as the BR model parameter influences low O_x production rates near the axis intercept mainly. The χ^2 goodness of fit parameter remains under the number of data points by nearly a factor of 2, which can be interpreted as the model errors being overestimated possibly by about a factor of $\sqrt{2}$.

Table 4.1: Net O_x production correlation parameters for the measurement visual the zero and 600ppb CO equivalents background reactivity (BR) model runs. Given is the standard deviation σ in ppb/h, the axis intercept b in ppb/h and slope m of the fitting line $C_{mod} = m \cdot C_{meas} + b$, the number of data points N, the correlation coefficient r and the goodness of fit measure χ^2 .

BR	σ	$b \pm \sigma(b)$	$m \pm \sigma(m)$	N	r	χ^2
0	1.6	-2.2 ± 0.9 -0.9 ± 1.0	1.3 ± 0.2	18	0.90	9.8
600	1.9	-0.9 ± 1.0	1.3 ± 0.2	18	0.85	8.4

The MCM model not only yields O_x production rates, but also provides concentrations of the whole set of known trace constituent participating in

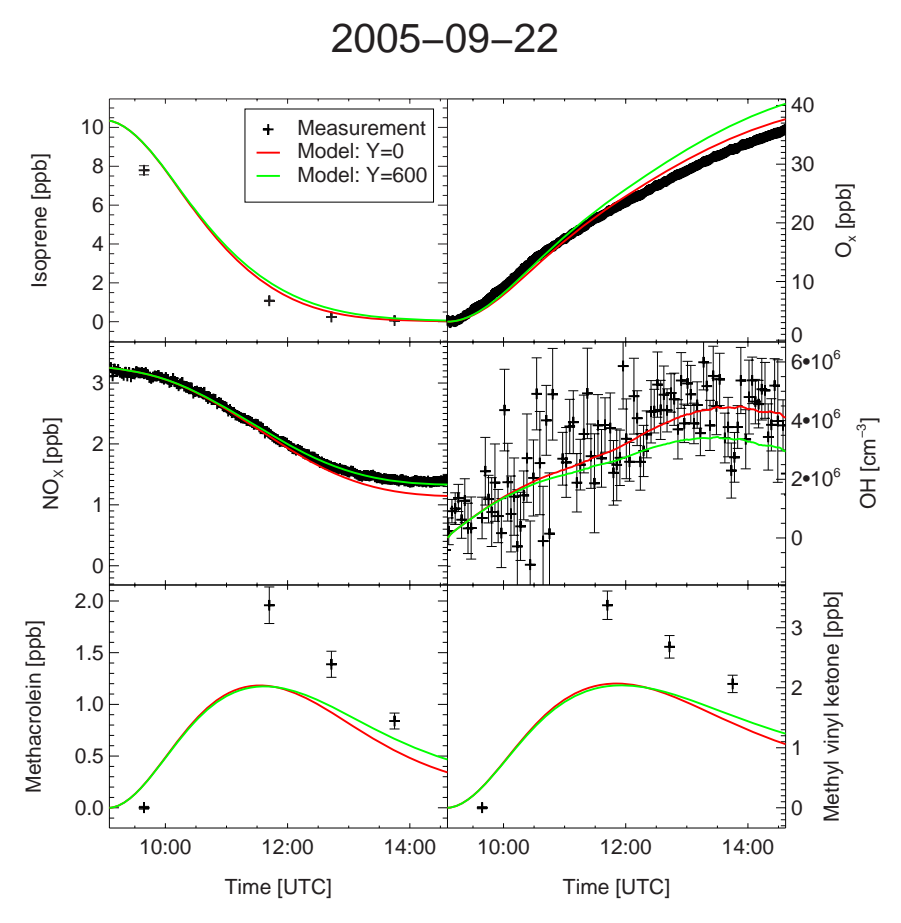


Figure 4.2: Fully time dependent MCM isoprene model run of the 22nd Sep 2005 experiment compared to the Perkin Elmer GC (isoprene, methacrolein and methyl vinyl ketone), UV-A ozone combined with CL NO₂ measurements combined to yield O_x, CL NO_x, and DOAS OH measurements (black crosses). Apart from the MACR and MVK yields, which are greatly underestimated, both "extrem case" model runs with zero (red line) and 600ppb CO equivalents background reactivity (green line) are in quite good agreement with the measurements. During approximately the first two hours, the OH concentration is dominated by the isoprene concentration. The model runs differ only slightly. Later on, with nearly no isoprene left in the chamber, the background reactivity becomes a determining factor.

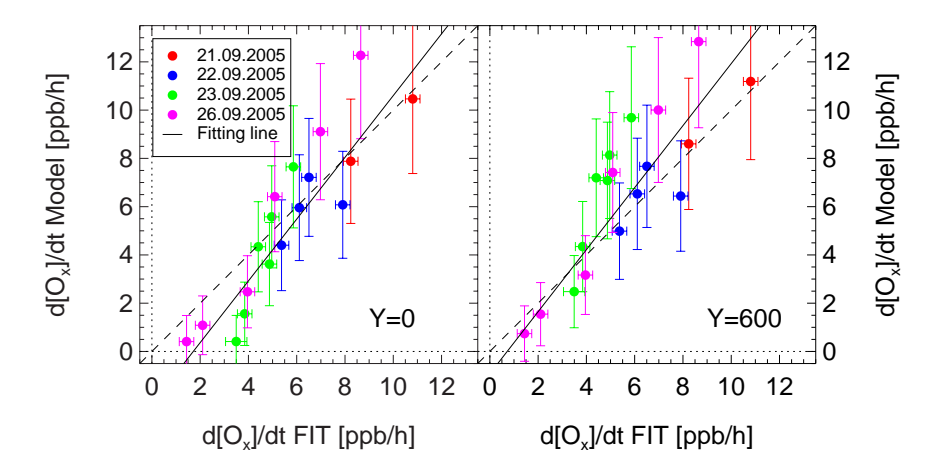


Figure 4.3: Correlations of the net O_x productions between measurements and fully time dependent model runs. On the left hand side the measurements (x-axis) are compared to the zero ppb background reactivity model runs (y-axis), on the right hand side they are compared to the 600ppb model runs. The preprocessing of the data is described in the text. The four different experiment days are color coded. The data points scatter around the dashed line indicating the 1:1 ratio for orientation. A tendency of overestimating high production rates and underestimating low values exists. The lower production rates appearing to the end of the experiments, are influenced mostly by the different background reactivities. Trend lines for each data set are provided as black solid lines.

the isoprene degradation. Thus, further analysis was feasible concerning the isoprene concentration and the yields of the first degradation products MACR and MVK, which were all measured with the Perkin Elmer GC during the analyzed experiments. To compare the measured with the modelled concentrations, the arithmetic means of the model runs during the sampling periods were calculated. The comparison of measured and modelled VOC concentrations is provided in figure 4.4. It demonstrates, that the concentrations of the initial VOC isoprene are very well represented by the model, as they scatter around the 1:1 ratio, which is given as a dashed line for orientation in the plot. This behavior is not astonishing, as the model isoprene concentrations mainly depend on a single reaction, namely C5H8 + OH. Reactions with the other oxidizing species O₃ and NO₃ can be neglected at the conditions during the experiments. The rate coefficient of the C5H8 + OH reaction is very well established [46], thus, the model time series is mainly influenced by the assumed initial isoprene concentration and by the modelled OH concentration. As the isoprene can be injected more accurately than measured [133], the initial concentration $[VOC]_0$ was calculated from the volume of liquid isoprene V_{liVOC}

injected into the chamber following equation 4.1.

$$[VOC]_0 = \frac{n_{VOC}}{n_{Chamber}} = \frac{V_{liVOC} \cdot \rho_{liVOC}/m_{VOC}}{V_{Chamber} \cdot [M]}$$
(4.1)

The number of isoprene molecules is denoted as n_{VOC} , the number of air molecules inside the chamber as $n_{Chamber}$. The density of the liquid isoprene ρ_{liVOC} is 0.681g/ml and the molecular mass m_{VOC} is 68.12u. The SAPHIR chamber volume $V_{Chamber}$ is $270m^3$ and the pressure p[hPa] and temperature T[K] dependent number density of air molecules $[M] = p/(T \cdot 1.379)$ $10^{-19})Kcm^{-3}hPa^{-1}$. The error of the injection volume is 0.1 μl at most, impurities in the liquid can lower the real amount additionally. A pessimistic estimation of the relative error for the initial isoprene concentration of 5% is hence assumed. The error margins given for the GC measurements account for the precision (standard deviation of repeated measurements of gas standards) of the calibration process only. Additional biases originating from sources of errors during this calibration and during the sampling process concerning the removal of ozone, are not included in the delivered error estimates. The deviations found between GC measurements of the initial isoprene concentration and its calculation from the amount of liquid isoprene of 29, 18, 16, and 13% lower measurements than calculations for the 21st, 22nd, 23rd and 26th Sep 2005 experiment, respectively, may hence be attributed to these unaccounted sources of errors.

To calculate a weighted correlation for each single VOC, once more a relative error of 20% plus a bias of 5% the maximum value, accounting for accumulating errors, were applied to the model. For the measured data, the given experimental error estimates were used. The correlation parameters for each VOC are compiled in table 4.2.

In case of isoprene the slope of the linear least square fit lines do not significantly differ from one and the y-intercepts not significantly differ from zero. The linear correlations are almost perfect, and the χ^2 tests, yielding considerably less than the number of data points analyzed, suggest the model error to possibly be overrate.

In contrast to the good model performance of the initial isoprene, the first generation degradation products MACR and MVK are by no means represented well by the model. The yield of MACR is underestimated significantly by nearly 50%. Measurement and model figured out to be correlated linearly to some extent (r > 0.8, satisfactory χ^2). The correlation between MVK model and measurement is rather bad, so that the fitting line and χ^2 value have to be interpreted with care. A tendency towards an underestimation thus exists.

4.1.2 Discussion

The performance of the Master Chemical Mechanism isoprene degradation, which consists of 605 reactions (844 when adding the inorganic and chamber specific reactions introduced in chapter 3.1) of 201 organic species, showed to be very good concerning O_x production in NO_x polluted air in ambient concentrations. Especially, when considering the single reactions' high uncertainties

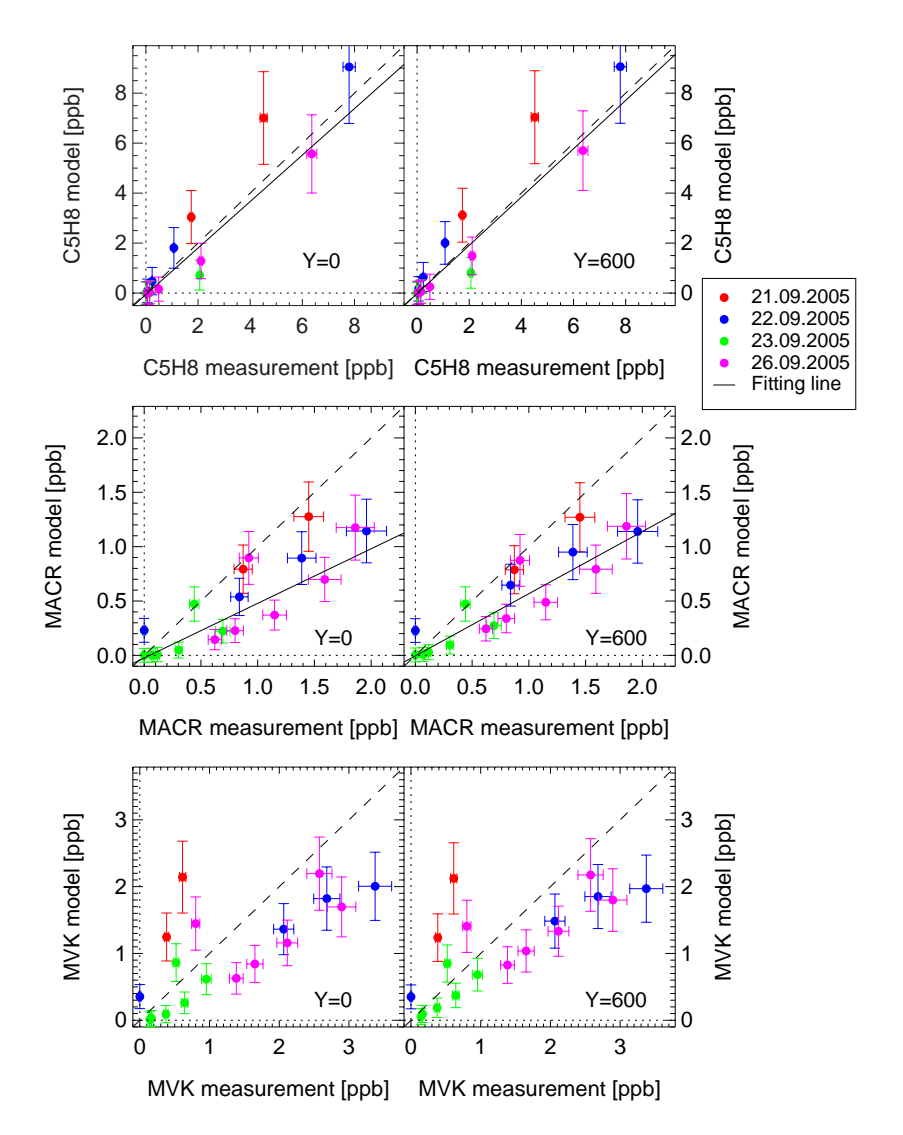


Figure 4.4: Correlations for measured vs. modelled VOC concentrations for Sep 2005 experiments during the illumination phases. The isoprene concentrations (upper panels) scatter around the 1:1 ratio (dashed line). The MACR (middle panel) is underestimated clearly, which is stressed by the best-fit solid line (compare text). The linear correlation between MVK measurement and model is rather bad, nevertheless, a tendency towards underestimation can been observed.

Table 4.2: Correlation parameters for the measurement visual the zero and 600ppb CO equivalents background reactivity (BR) model run for isoprene, methacrolein and methyl vinyl ketone. Given is the standard deviation σ in ppb, the axis intercept b in ppb and slope m of the fitting line $C_{mod} = m \cdot C_{meas} + b$, the number of data points N, the correlation coefficient r, and the goodness of fit measure χ^2 .

Specie	BR	σ	$b \pm \sigma(b)$	$m \pm \sigma(m)$	N	r	$ \chi^2 $
C5H8	0	1.0	-0.06 ± 0.14	0.93 ± 0.14	18	0.95	11.5
C5H8	600	1.0	-0.03 ± 0.15	0.97 ± 0.14	18	0.95	10.9
MACR	0	0.3	-0.02 ± 0.03	0.51 ± 0.06	18	0.86	30.1
MACR	600	0.2	0.0 ± 0.04	0.58 ± 0.06	18	0.90	19.4
MVK	0	0.6	0.03 ± 0.06	0.61 ± 0.07	18	0.71	37.1
MVK	600	0.6	0.11 ± 0.07	0.64 ± 0.08	18	0.75	29.2

of products, branching ratios and/or rate coefficients, which partially have an error estimate of a factor two, the correspondence is remarkable. Low production rates strongly depend on the applied background reactivity, in contrast to the gradient of the fitting line between measured and model O_x production rates, which did not significantly differ from one. The assumed model error estimate of around 20% probably exceeds the real error. Therefore, it can be said, that the O_x production can be predicted by the MCM better than within 30%, which was supposed by *Dodge 2000* [134] to be a realistic model error estimation. In her critical review on chemical oxidant mechanisms and their derivation and evaluation with the help of smog chamber experiments, she concluded, that "Given all these uncertainties, it would be surprising if available chemical mechanisms predict O_3 control strategies to better than $\pm 30\%$."

Obviously, the high model:measurement correspondence of the O_x production is a cancelling out of different errors. On the one hand, the O_x production in the MCM is influenced by about 200 reactions of ozone and NO₂. On the other hand, the concentration of the first degradation products MACR and MVK is influenced by about 20 production and destruction reactions. These intermediate species, which amount to about 70% of the isoprene's first generation degradation products, on the way from isoprene towards ozone, are much worse represented by the model than ozone. The underestimation of the MACR yield, which has already been reported by Karl et al. 2006 [96], was hence reproduced. When considering the up to 30% underestimation by the GC measurements, which could be quantified for the isoprene concentration, even stronger model deviations for MACR and MVK are likely, if all GC measurements would be "corrected" by the same factor.

Despite this GC underestimation, astonishingly, the measured isoprene concentrations are quite well represented by the model. This can only be attributed to elevated isoprene degradation rates predicted by the model due to overestimated OH concentrations. Additionally, the coverage of the data range is quite poor, as the isoprene nearly totally degrades within two GC

measurements, with the rest of the data conglomerating near the origin.

No compleat photochemical degradation of isoprene could be examined during the one day experiments, as still amounts of the degradation products, e.g. MACR, MVK, and HCHO, resided in the chamber, when the roof was closed and thus the further photochemical degradation stopped. Only about maximal six ozone molecules per isoprene reacted were produced, which is below the half of the theoretical 14 ozone molecules possible through OH induced degradation of isoprene as explained in chapter 2. Thus, the question still exists, whether the under- and overestimation already observed during the first few hours of the degradation, compensate for each other, so that the total amount of O_x produced per totally degraded isoprene is predicted correctly by the MCM. Due to the increasing influence of the background reactivity during the one day experiments and cause of the dilution by the replenishment flow, longer SAPHIR experiments will not answer this question. Therefore, independent one day photochemical O_x production chamber experiments of the main degradation products are necessary. This has already been done, but owing to high discrepancies between the NO_x model and measurement time series, further analyzed in chapter 5, adequate adjusting of the chamber HONO source and therewith the primary OH production is as impossible as a reasonable fully time dependent modelling.

4.2 First Degradation Step Approach

In the last subchapter it was shown, that the MCM $\rm O_x$ production predictions of the isoprene mechanism are quite good and much better than the model results of some intermediate species. The practicability for field experiments however is restricted by difficulties of defining representative initial conditions and by the nonlinearity of the chemical processes. Possibly unconsidered physical changes of trace constituents' concentrations, therefore, can influence the further chemical progress strongly. To couple time dependent model runs with the observed concentration time series, it is routine, to use these measured series as constraints for model runs. Still complex modelling is needed in the process.

In this chapter, the testing of a new approach for predicting the O_x production is presented, which uses all measured VOC and CO concentrations, which are together denoted as "fuel measurements" in the following, as they form the "fuel" for the photochemical O_x production. As beside the meteorological conditions also the measured concentrations of NO, NO₂, and OH are used, this first-degradation-step (FDS) approach is quasi the opposite of the one presented before, where measurements of gas phase species were not used as input variables at all. The approach only accounts for the first degradation step of each measured fuel, with the yields of species different from NO₂, O₃ and HO₂, which is a direct precursor of NO₂ (compare equation R2.18), being unimportant. By prescribing all the measured data, no extensive numerical simulations are necessary anymore, but basic arithmetics are sufficient.

4.2.1 Used Method

In the scope of this thesis, the first degradation step of a fuel is defined as the initial reaction induced by OH, O₃, or NO₃ attack or photolysis plus all subsequent reactions of the produced radicals. Stable products, which just degrade further, if a new initialization takes place, do not contribute to the first degradation step any more. As the radical reactions are orders of magnitudes faster than the initial reactions, the rate of the HO₂ and NO₂ and thus O₃ or O_x production of the *n*th VOC's first degradation step $\left(\frac{d[O_s]}{dt}\right)_n$ can be derived from the sum of the initial reaction rates $v_{n,\text{OH}}, v_{n,\text{O3}}, v_{n,\text{NO3}}$, and $v_{n,\text{h}\nu}$ times nearly constant amplifying factors $f_{n,\text{OH}}, f_{n,\text{O3}}, f_{n,\text{NO3}}$, and $f_{n,\text{h}\nu}$, respectively, depending on the particular mechanism:

$$\left(\frac{d[O_x]}{dt}\right)_n = v_{n,OH} \cdot f_{n,OH} + v_{n,O_3} \cdot f_{n,O_3} + v_{n,NO_3} \cdot f_{n,NO_3} + v_{n,h\nu} \cdot f_{n,h\nu}$$
(4.2)

When introducing the destruction velocity d_n of the nth VOC, which is

$$d_n = v_{n,OH} + v_{n,O_3} + v_{n,NO_3} + v_{n,h\nu}$$
(4.3)

a combined amplifying factor f_n can be defined as

$$f_n \equiv \frac{\left(\frac{d[\mathcal{O}_x]}{dt}\right)_n}{d_n} \quad \Leftrightarrow \quad \left(\frac{d[\mathcal{O}_x]}{dt}\right)_n = d_n \cdot f_n$$
 (4.4)

For example, the factor $f_{\rm VOC}$ of the idealized OH induced VOC ozone production cycle presented in chapter 2.1.1 is two; with CO as a fuel in an idealized cycle, the factor $f_{\rm CO}$ is one. Realistic amplifying factors and their variation in time for the isoprene degradation experiment of the 4th May 2006 experiment are provided in figure 4.5. Although the concentrations of OH, $O_{\rm x}$ and the VOCs, which are also shown in the figure, vary a lot, the amplifying factors of isoprene, MACR, MVK and HCHO are nearly constant during the illumination phase. The factor for isoprene nearly equates the idealized VOC factor of two, even more $O_{\rm x}$ per VOC degraded comes out for MACR and MVK. The factor for HCHO almost matches the idealized CO factor of one.

Summing up the contributions of all m individual measured VOCs and the contribution of CO should then give the O_x production being explained by the fuel measurements $\left(\frac{d[O_x]}{dt}\right)_{free}$:

$$\left(\frac{d[\mathcal{O}_{x}]}{dt}\right)_{\text{fme}} = \sum_{n=1}^{m} \left(\frac{d[\mathcal{O}_{x}]}{dt}\right)_{n} + \left(\frac{d[\mathcal{O}_{x}]}{dt}\right)_{\text{CO}} \tag{4.5}$$

The computation of the destruction rate is quite simple, just using equation 4.3 and applying the measured values marked here and in the following with the subscript meas, or, in the few cases where measurements are not available, model assumptions, marked with the subscript mod:

$$d_n = (\mathbf{k}_{n,OH}[OH]_{meas} + \mathbf{k}_{n,O_3}[O_3]_{meas} + \mathbf{k}_{n,NO_3}[NO_3]_{mod} + \mathbf{J}_{n,meas \text{ or } mod}) [VOC_n]_{meas}$$

$$(4.6)$$

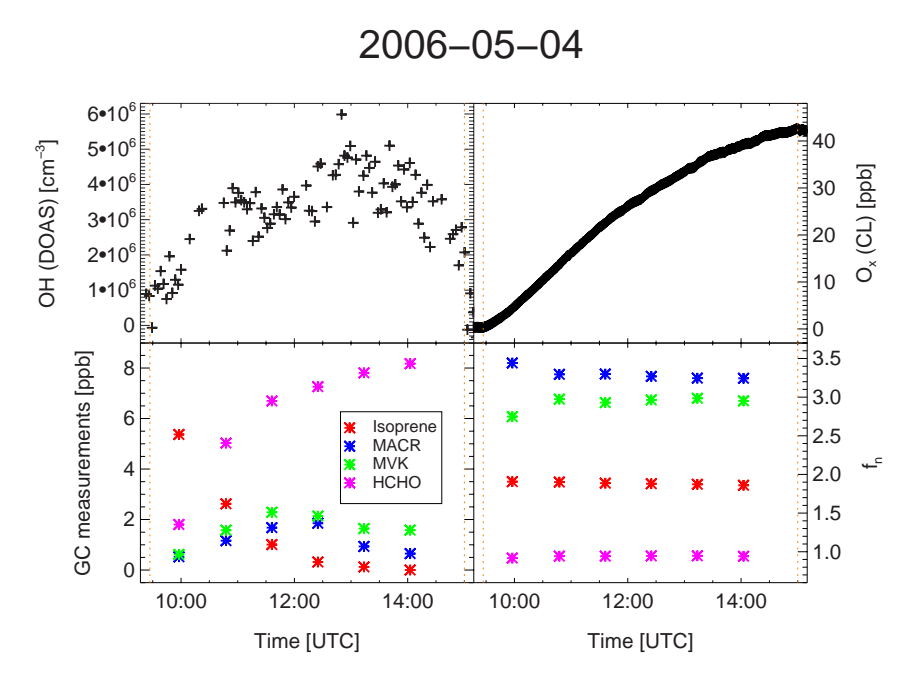


Figure 4.5: Variations of amplifying factors over time. Although the concentrations of OH (DOAS measurements shown in the upper left panel), O_x (combined O_3 and NO_2 CL measurements, upper right panel) and VOC (GC measurements, lower left panel) vary a lot, the amplifying factors of the measured VOCs show to be nearly constant (lower right panel).

Model assumptions thus had to be taken in the case for NO_3 concentrations and some photolysis frequencies. As NO_3 is photolyzed during daytime, very low concentrations are expected by the model. The NO_3 reaction rates are about three to four orders of magnitude lower than the reaction with OH. Thus only an underestimation of about 2 orders of magnitude, which are highly implausible, would change the degradation rate at most in the percent range. As the photolysis of some species, exemplary the photolysis of MACR, makes up about 30% of the whole degradation in the MCM model, the calculation of the destruction rate and branching ratios (see below) is much more errorprone concerning wrong photolysis frequencies. As other assumptions of the presented approach showed to be much more critical, which is discussed below, the error-proneness concerning wrong photolysis frequencies, has not been studied any further.

As the VOC measurements by the GC system yields concentration mean values for the 30min sampling time, all other measurements and model assumptions were averaged over the same periods of time.

A key role of the tested first-degradation-step approach plays the determination of the correct amplifying factors f_n . The way this is done is illustrated in figure 4.6 for the quite simple VOC ethanal. The procedure resembles probabilistic evaluation, as some kind of decision tree can be compiled representing the first degradation step. The initial VOC is located at the left. All initial reactions, three in the case of ethanal, are represented by a single branch starting at the ethanal and ending at the produced radical. If more than one reaction gives the same main product, the branches are connected at the endpoints, and the main product is given in the middle of the connection. Differing side products are specified at the endpoints. The reactant R is stated at the tilted part of the branch. For each of the m possible reactions of the consecutively numbered educts N, a branching ratio αN_R , comparable to the probability for this branch to be followed, can be calculated by the ratio:

$$\alpha N_{R_i} = \frac{v_{R_i}}{\sum_{j=1}^m v_{R_j}}$$

$$= \frac{k_{R_i}[R_i][N]}{\left(\sum_{j=1}^m k_{R_j}[R_j]\right)[N]} = \frac{k_{R_i}[R_i]}{\sum_{j=1}^m k_{R_j}[R_j]}$$
(4.7)

It is independent on the concentration of the educt N, as the fraction can be reduced by it, but remains to depend on the rate coefficients and the the concentrations of the (measured) reactants. For one educt N the complete sum of its αN_i is one.

To finally get the amplifying factor, each branch, which influences the concentration of O_x , hence NO_2 , O_3 and the NO_2 precursor HO_2 , thus having one or more of these species as educt or product, has to be followed. The branching ratios along each way to the specie are multiplied and the final amplifying factor is obtained by adding all results of the pathes with the stated species being products and subtracting the ones with the species being educts. If loss processes shall be treated later on, the amplifying factors can be set up for each specie separately. To illustrate the procedure, this is exemplarily done

for ethanal:

$$\begin{split} f_{\text{CH3CHO}}(\text{O}_3) &= (\alpha 1_{OH} + \alpha 1_{NO3}) \cdot \alpha 2_{HO2b} \\ f_{\text{CH3CHO}}(\text{NO}_2) &= (\alpha 1_{OH} + \alpha 1_{NO3}) \cdot \alpha 2_{NO} + \\ & \left[(\alpha 1_{OH} + \alpha 1_{NO3}) \cdot (\alpha 2_{NO} + \alpha 2_{RO2b}) + \alpha 1_{h\nu} \right] \cdot \alpha 3_{NO2b} \\ f_{\text{CH3CHO}}(\text{HO}_2) &= + \alpha 1_{h\nu} \\ & - (\alpha 1_{OH} + \alpha 1_{NO3}) \cdot \alpha 2_{HO2a} \\ & - (\alpha 1_{OH} + \alpha 1_{NO3}) \cdot \alpha 2_{HO2b} \\ & - \left[(\alpha 1_{OH} + \alpha 1_{NO3}) \cdot (\alpha 2_{NO} + \alpha 2_{RO2b}) + \alpha 1_{h\nu} \right] \cdot \alpha 3_{HO2} \\ & + \left[(\alpha 1_{OH} + \alpha 1_{NO3}) \cdot (\alpha 2_{NO} + \alpha 2_{RO2b}) + \alpha 1_{h\nu} \right] \cdot \\ & (\alpha 3_{NO2b} + \alpha 3_{RO2a}) \cdot \alpha 4 \end{split}$$

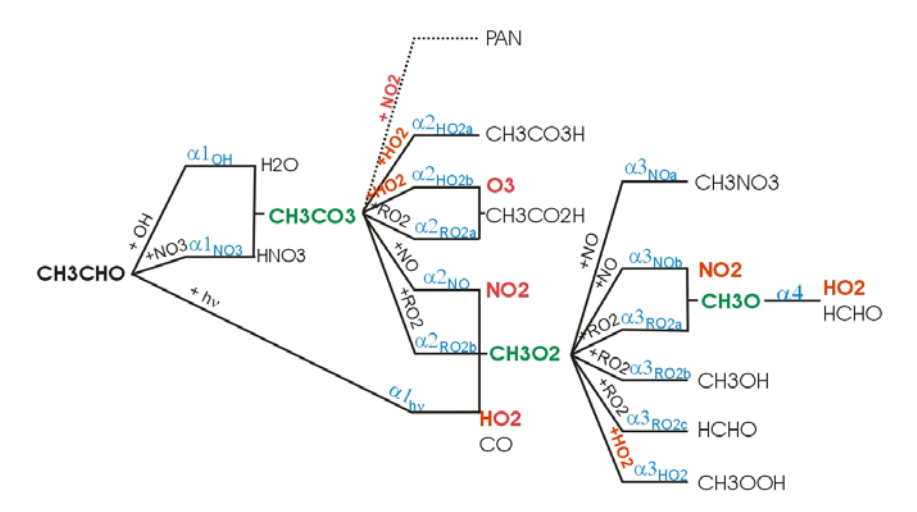


Figure 4.6: "Decision tree" for the determination of the amplifying factors. For the simple VOC ethanal, the first degradation step is plotted. Each branch symbolizes a possible reaction, with the reactants at the tilted part of the branch. Stable products are given in black at the end of the branches, radicals, which are processed further, are given in green. Reactions with the same main product are connected at the branches' end points. The species NO₂, HO_2 and O_3 , which are important for the O_x production, are displayed with red letters. Every branch with these species as educts or products is of importance for the amplification factor. The production of PAN, which is assumed to be in thermal equilibrium, thus decomposing at the same rate as being produced, is excluded from being a degradation path of the preceding radical. The branching ratios α can be easily defined and combined to give the amplifying factor. The procedure is described in the text.

Peroxyacyl nitrates are assumed to nearly be in thermal equilibrium, hence their production and decomposition rate being almost the same. With this assumption the PANs' production reaction has to be excluded from the calculation of the destruction rate of the precursor radical, as the production rate is almost balanced by the PANs' thermal decomposition and nearly no net effect is expected.

As in the previous subchapter, in the analysis, the derived $\left(\frac{d[O_x]}{dt}\right)_{\text{fme}}$ values were compared to the mean measured dO_x/dt corrected for the dilution.

4.2.2 Results

The approach was applied to the 4 experiments described in the previous subchapter. As no adjusting of the chamber source terms was necessary this time, additionally, it was applied to the experiments conducted in Oct 2005, May and June 2006, listed in the appendix B, table B.2. This experiments were executed like the experiments of the Sep 2005 period. Over night the chamber was flushed till ozone and NO_x were below the LoD. With the roof still closed, the chamber air was humidified, and the trace gases were added. At least one GC measurement was awaited, and then the roof was opened. Beside the GC (Perkin Elmer and/or Chrompack) and the obligatory NO, NO_2 and new ozone CL measurements, also DOAS OH and HCHO measurements were available for all of these experiments. As initial VOC, not only isoprene, but also methacrolein and methyl vinyl ketone were used. The starting concentration of NO_x was varied between "zero" (below LoD) and about 20ppb.

Exemplarily in figure 4.7, the results for the 15th of May 2006, which has been an experiment with round 10ppb MACR as the initial VOC and 18ppb NO_x in the beginning, are presented. In the upper left panel, the concentrationtime profile for O_x is shown together with the fitted straight lines for the determination of the O_x gradient. As in the example given in figure 4.1, the course is approximated by the straight lines quite well. Both, the gradient of the fitting lines corrected for the dilution and the O_x production calculated with the FDS approach are plotted over time in the upper right panel. Within their error margins, both are in agreement on this day. Astonishingly, the three values calculated for the early experiment times lie above the fitted ones, although, undoubtedly, not all degradation products could be measured with the used measuring instruments. Later on, the O_x production seems to be underestimated by the FDS approach, which is the expected behavior. With smaller symbols, the individual contributors of the calculation are plotted. To improve their visibility, they were plotted a little back shifted in time. In the beginning, MACR is, of course, the main contributor, later on it is superseded by HCHO. All other VOCs measured can be neglected, although the sum of the concentrations exceeds the one of MACR towards the end of the experiment. This is illustrated in the lower right panel of figure 4.7, where the concentration-time profiles of the measured VOCs are shown. Beside the VOC concentrations, the OH concentration is the main determining component of the FDS approach. That is why the DOAS measurements and the half an hour mean values are also shown (lower left panel).

Obviously, the net O_x production is not highest, when the initial VOC is highest, cause the OH concentration is very low due to the low HONO level at that early time. With a rising HONO level produced by the chamber source, the primary OH production increases, too, and the OH concentration levels on a higher value. About an hour later, the O_x production reaches its maximum, when still a lot of MACR is present and the OH concentration has increased. As the MACR's degradation products, one of which is HCHO, are less reactive against OH, the O_x gradient decreases in the following due to the decreasing reactivity of the VOC mix.

Although some single experiment days, like the one shown in figure 4.7, yield promising results, a correlation analysis of the combined data set of all mentioned experiments show a very bad correlation of r = 0.65 only. The χ^2 test for a weighted linear least square fit yields 361, which exceeds the number of data points N = 96 nearly by a factor of four, hence indicating a bad performance of the first-degradation-step approach. Increasing the error estimates for the approach, which have been, as a first guess, approximated by the sum of the relative OH and VOC measurement errors without introducing an additional approach error, would end in an better χ^2 test, but still the bad correlation. A systematic error of the FDS approach is therefore assumed, which cause a not linear deviation. This nonlinearity becomes obvious, when locking at the comparison of the fitted, dilution corrected and FDS calculated O_x production of the data set provided in figure 4.8. In the upper left panel, all experiment days are presented, which seem to tolerably group around the 1:1 line also given. The slope of the weighted linear least square regression line of 1.34±0.19 does not significantly differ from one. When looking at the data sets separated by the initial VOCs, no nonlinearity is recognizable for the isoprene subset. The correlation coefficient r = 0.66 is still low mainly cause of the comparatively high errors compared to the covered data range (compare appendix C). The slope of the regression line (0.95 ± 0.25) is nearly one. In the case of MACR however, both experiments in the medium NO_x range (6th of Oct 2005 and 13th of Jun 2006, pink and dark grey dots respectively) show a strong overestimation in the beginning. This overestimation is partly balanced by an underestimation in the following. The correlation r = 0.59 is worse than the one for the whole data set. The slope of the regression line (2.22 ± 0.54) significantly differs from one. The same characteristic found for the MACR experiments, although not that distinct, can be observed for the medium NO_x range MVK experiments (8th of May 2006 and 12th of June 2006, brown and light grey dots respectively). As they are very slight and the data range covered is greater than the one of the isoprene subset compared to the error estimates, the correlation coefficient r = 0.79 is even higher than the one of the isoprene subset. The slope of the regression line (1.06 ± 0.22) once more is not significantly different from one.

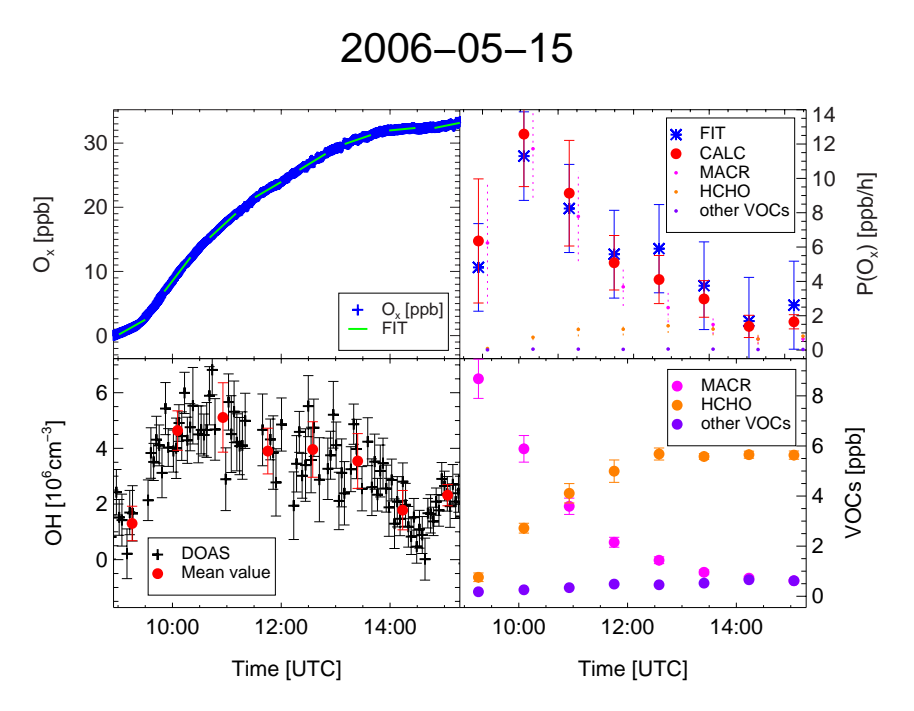


Figure 4.7: Time series of fitted versus first-degradation-step approach O_x production on 15th of May 2006. In the upper left panel, the blue crosses show the measured O_x progress over time. The fitting lines to determine the experimental production rate are plotted as green straight lines. In the upper right panel, the fitted production, corrected for the dilution (blue stars), is shown together with the FDS approach calculated production (red dots) over time. Within the error margins, both time series correspond for this day. With small symbols, the different contributors of the FDS approach are also given a little shifted in the time axis for better visibility. The main determining components, OH and VOC concentrations, are shown in the lower right and left panel, respectively.

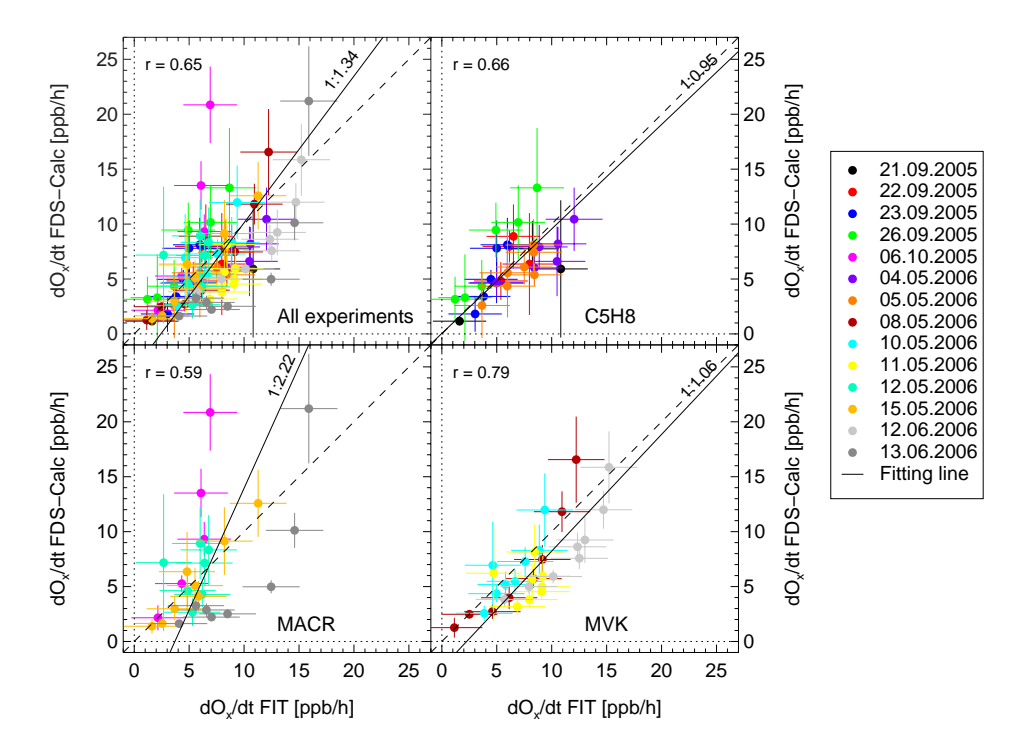


Figure 4.8: Comparison of fitted and FDS calculated photochemical net O_x production for experiments between Sep 2005 and June 2006. In the upper left panel, the whole data set is presented. The FDS calculated is plotted over the fitted, dilution corrected O_x production in ppb/h. The fitting yields a production of up to 15ppb/h, the FDS calculation even gives a maximum of about 21ppb/h. When looking at the data subsets for each initial VOC, nonlinearities become conspicuous for MACR (lower left panel, pink and dark grey data series) and MVK (lower right panel, brown and light grey data series), starting with an overestimation followed by an underestimation. The isoprene data (upper right panel) do not show such structures. Correlation coefficients for each data set are given in the upper left corner of each plot and the slopes of the weighted linear least square fitting lines (black solid) are written next to the respective lines.

4.2.3 Discussion

To analyze the performance of the FDS approach, also fully time dependent MCM model runs, as presented in the last subchapter, were consulted. When comparing the days with a bad performance of the FDS approach with the ones, where FDS approach results in a better correspondence to the measurements, a high amount of PANs produced (> 1ppb) is the most pronounced difference. As PANs are reservoirs for NO₂ and organic peroxy radicals, hence the precursors for the ozone production, their production and destruction reduces and raises the ozone production, respectively. The assumption made during the development of the FDS approach, that PANs rapidly reach their thermal equilibrium and only vary slightly most of the time, may hence be critical for chamber experiments. Due to the abrupt start of these experiments, with the initial VOC being rather high and no PANs being present in the beginning, high production rates of PANs may occur at the experiment's early stages. In the case of the OH induced degradation of MACR proposed by the MCM, which has been used for the derivation of the FSD approach, additionally, a cascading effect of radical reactions amplifies the effect of a wrong assumption concerning the production of PANs. To illustrate this, in figure 4.9, the MCM OH induced methacrolein degradation is plotted. Two different organic peroxy radicals can be formed by the initial OH attack. In the lower branch of figure 4.9, which proceeds over MACO3, MPAN and PAN are build. If one MPAN molecule is build in the MCM, not only the MACO3 radical and one NO₂ is temporarily consumed, but also the following radical reactions will not take place. During these cascading radical reactions, altogether three NO molecules are oxidized towards $\mathrm{NO}_2,$ and one HO_2 comes out. In MCM nomenclature the main reactions are:

$$MACO3 + NO \longrightarrow CH3CO3 + NO2 + HCHO$$
 (R4.1)

$$CH3CO3 + NO \longrightarrow CH3O2 + NO2 + CO2$$
 (R4.2)

$$CH3O2 + NO \longrightarrow CH3O + NO2$$
 (R4.3)

$$CH3O + O2 \longrightarrow HCHO + HO2$$
 (R4.4)

Hence a wrong assumption concerning MPAN production implies a wrong O_x production of about 5 times the MPAN production rate. Exemplarily, when a net MPAN production of 1ppb/h takes place at the beginning of the experiment, and the FDS approach disregards this net production, then, instead of applying a -1ppb/h loss of NO_2 through reaction

$$MACO3 + NO2 \longrightarrow MPAN,$$
 (R4.5)

it uses a +4ppb/h O_x in its production calculation. As not only the MPAN reservoir substance is built up in the beginning, but also PAN, the wrong PANs assumption easily causes the FDS approach to overestimate the O_x production by several ppb/h. In the case of MVK, beside PAN also its hydroxy derivative PHAN is built. As less radical reactions follow the PHAN precursor radical HOCH2CO3 as in the case of the MPAN precursor, the wrong PHAN production assumption has a less serious but still notable effect. In the case of the

isoprene degradation, the noted PANs are produced too, of course. Due to the spreading of the initial VOC amount onto the various intermediate products, mainly MACR and MVK, which degrade further on slightly different time scales, the building up of the PANs is not synchronous, but staggered, and less of each single peroxyacyl nitrate is synthesized compared to the MACR and MVK experiments. No overestimation in the beginning or underestimation in the following is hence evident.

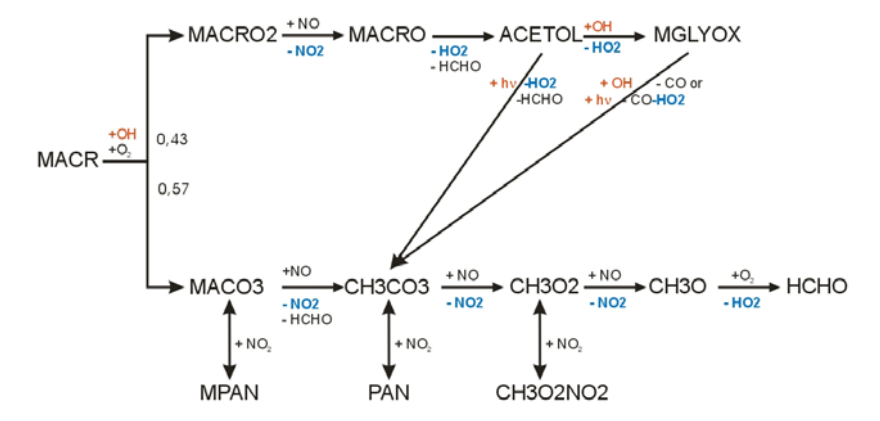


Figure 4.9: Main pathes of the methacrolein degradation induced by OH as proposed by the MCM. Two different organic peroxy radicals can be built in the reaction of MACR with OH. In the lower branch, the radical and NO₂ reservoirs MPAN and PAN are build. During the MPAN production, not only one NO₂ is consumed per MPAN formed, but also three NO₂ and one HO₂ less are formed. The upper branch also entails the production of the PAN precursor radical, but as one to two new initialization by photolysis or OH are necessary, the PAN production of this branch is delayed compared to the one of the lower branch.

Summing up, it can be said, that the FDS approach, with the assumption of nearly constant levels of the PANs, is not practicable for the interpretation of chamber experiments, as sudden changes of the concentration and lighting conditions possibly cause a rapid production of peroxyacyl nitrate species. Due to the sensitivity of the FDS approach toward the PANs gradient, in certain circumstances with well defined physical influences of the studied air mass, its comparison with the measured O_x progress, however, may be used as an indicator for the actual gradient of the PANs stage. If the assumption of constant PANs is applicable, which is the case during field campaigns most of the time, as due to continuing emissions a pseudo stationary state of the PANs is reached, the FDS approach may, nevertheless, be practicable for estimating the in situ photochemical O_x production. For the isoprene subset, which is most relevant, as isoprene is the biogenic specie emitted, not MACR of MVK, which never solely occur in nature, the slope of the regression line after all was

nearly one. To get a good estimation, presuming a pseudo stationary state of the PANs, a nearly complete chemical characterization of the analyzed air mass is necessary, which makes this approach highly expensive concerning measuring effort. An easier way to get a good estimation, with much less needed measured input, is presented in the following subchapter.

The analysis of the FDS approach additionally pointed out, that a proper understanding of the the PANs' production and destruction processes is crucial for a sound prediction of the current O_x progress caused by photochemistry. However, severe MCM model deviations concerning the PAN yield during the daytime OH and concerning the MPAN yield during the nighttime NO_3 induced MACR degradation have been identified during SAPHIR experiments. These are further analyzed in chapter 5.

4.3 OH Lifetime

The most important oxidizing agent of the troposphere during daytime is the OH radical, as nearly all tropospheric trace gases are degraded via OH induced oxidation. Its main primary production processes are the

• photolysis of ozone (see also detailed reaction scheme R2.13 - R2.16 given in chapter 2.1.1):

$$O_3 + h\nu \xrightarrow{H_2O} 2 \text{ OH}$$
 (R4.6)

• the photolysis of HCHO in areas of high anthropogenic air pollution yielding HO₂. Combined with its subsequent reaction with NO it can be designated as a OH source:

$$\text{HCHO} + h\nu + 2\text{O}_2 \xrightarrow{\text{M}} \text{CO} + \text{HO}_2 + \text{HO}_2$$
 (R3.6)
 $\text{NO} + \text{HO}_2 \longrightarrow \text{NO}_2 + \text{OH}$ (R2.18)

• the photolysis of HONO, especially during chamber experiments, but also in the atmosphere :

$$HONO + h\nu \longrightarrow NO + OH$$
 (R3.1)

The large primary production of the $\rm HO_x$ radicals ($\rm HO_x=OH+HO_2$) is balanced by chain terminating, radical consuming reactions (compare page 17), so that a quasi steady state is reached in the troposphere within seconds [135]. Depending on the VOC and $\rm NO_x$ concentration, the OH / HO₂ ratio adjusts. In highly VOC polluted air, the ratio is lowered, as the OH rapidly reacts with these VOCs. This fact is also used for another measure of the abundances of chemical emissions and their oxidation products, the so-called

OH lifetime $\tau_{\rm OH}$ [136]. It can be defined as the inverse of the OH reactivity $k_{\rm OH}$, which is given by equation 4.8:

$$\tau_{\text{OH}}^{-1} \equiv k_{\text{OH}} = \sum_{i} (k_{\text{OH+VOC}_{i}}[\text{VOC}_{i}]) + k_{\text{OH+CO}}[\text{CO}] + k_{\text{OH+NO}}[\text{NO}] + k_{\text{OH+NO}_{2}}[\text{NO}_{2}] + k_{\text{OH+SO}_{2}}[\text{SO}_{2}] + \dots$$
(4.8)

where $k_{\rm OH+X}$ corresponds to the bimolecular rate coefficient of the reaction OH + X. The reactivity hence corresponds to an integrated pseudo first order rate coefficient for the loss of OH. The OH lifetime is frequently dominated by the reactions with NMHCs [135]. As not all NMHCs can be measured, instruments for the direct measurement of the OH lifetime have been developed [136, 137]. One kind of instrument is based on OH measurements with the LIF technique inside a flow tube. Ambient air enters this flow tube, and excess OH is added, which is produced via a photolysis reaction. Then, the OH concentration is measured at different distances from the OH injection. By dividing the distance by the known flow velocity inside the tube, the decay time is achieved. After corrections for wall losses and OH recycling effects, the gradient of a logarithmic plotting of the concentrations over the reaction time gives the OH reactivity.

An OH lifetime measurement instrument of this kind will soon be established at the SAPHIR chamber, too. Preliminary model studies concerning the use of $\tau_{\rm OH}$ as a proxy for determining the photochemical $\rm O_x$ production rate therefore have been carried out and will be presented in the following. Proxy methods, which use the OH reactivity have already been proposed, e.g. by Kleinman et al. 1997 [138] and Daum et al. 2000 [139]. Beside the OH reactivity they use the modelled primary HO_x production, the modelled HO_2 + RO_2 yield per OH reaction, comparable to the amplifying factors introduced in the previous subchapter, and the NO_x abundance as input to estimate the instantaneous net photochemical $\rm O_x$ production $\frac{d[\rm O_x]}{dt}$.

4.3.1 Idea

To develop an even simpler proxy method, the idea introduced in the previous subchapter of multiplying amplifying factors with the degradation rate of each VOC to get the O_x production is extended. Instead of defining an amplifying factor f_i for each VOC_i's degradation rate, an integrated amplifying factor $F_{\rm OH}$ for the OH reaction rate $v_{\rm OH}$, hence the rate OH reacts with any specie, which is the OH reactivity $k_{\rm OH}$ times the OH concentration $v_{\rm OH} = \tau_{\rm OH}^{-1} \cdot [{\rm OH}]$ will be defined as

$$F_{\rm OH} \equiv \frac{\frac{d[{\rm O_x}]}{dt}}{{\rm v_{\rm OH}}} = \frac{\frac{d[{\rm O_x}]}{dt} \cdot \tau_{\rm OH}}{[{\rm OH}]}$$
(4.9)

When considering the idealized ozone production cycle presented in chapter R2.16, which approximates OH induced VOC degradations, a first guess for F_{OH} would be two. As not all VOC degradations are induced by OH, but also photolysis or ozonolysis take place during daytime, which also influence $\frac{d[O_x]}{dt}$,

and additionally considering, that the OH induced HCHO and CO degradation at most yielded VOC specific amplifying factors $f_{\text{HCHO, OH}}$ and $f_{\text{CO, OH}}$ of one, a negative deviation from the idealized factor two is expected. Nevertheless, the factor may be quite constant for air masses, which are mainly influenced by biogenic VOCs, as the OH reactivity will be dominated by reactions with these VOCs and not by the reaction with carbon monoxide, then. This CO is mainly an anthropogenic trace gas, which is emitted by incomplete combustion and biomass burning. Moreover, it has been shown by Rohrer and Berresheim 2006 [140], that the OH concentration strongly correlates with the J(O¹D) photolysis frequency. On that account, the ratio between OH and photolysis induced VOC degradation can be presumed to be quite constant for each single VOC. With a rising ozone level, the part of ozonolysis induced VOC degradation increases of course. Changes of the integrated factor F_{OH} may thus occur in late evening and beginning evening twilight hours, when ozone level may have reached high values, and the OH concentration and photolysis strength decreases due to weakening sunlight. A dependence on the NO_x concentration is likely, too, as without NO_x no O_x production would take place, and on the other side NO_x is involved in many chain terminating reactions.

4.3.2 Used Method

As $\tau_{\rm OH}$ measurements are not jet available at the SAPHIR chamber, the needed parameters for the definition of the integrated amplifying factor F_{OH}, hence, following equation 4.9, beside the OH lifetime the OH concentration and the net O_x production, had to be derived from MCM model calculations of conducted SAPHIR chamber experiments. The same experiments as used in the previous subchapter were used for the determination of F_{OH} for biogenic dominated air masses. As no ample GC measurements were needed, also the MACR degradation experiment of the 1st Sep 2006 experiment could be included into the analysis, which was executed in the same manner as all other experiments already described. A table of the analyzed VOC degradation experiments is given in appendix B, table B.2. To be independent of a correct model prediction of the primary OH production by the chamber sources, model runs with measured DOAS OH concentrations as constraints were used. The HONO and HCHO source of these models were manually adjusted to best fit the NO_x and HCHO measurements, respectively. The background reactivity was adjusted to conform the model ozone to the ozone measurements. The model runs were forced to output results one a 60sec equidistant time scale. The OH DOAS measurements used as an input therefore had to be interpolated on the same time pattern.

The needed OH concentrations hence correspond to the interpolated DOAS measurements. As reaction rates are routine output of EASY model runs, the OH loss rate $v_{\rm OH}$ could be obtained by summing up the rates of all reactions with OH as an educt. Once having the OH loss rate, division by the OH concentration yields the OH reactivity $k_{\rm OH}$, which in turn gives the OH lifetime by inversion. For species, which are not prescribed by measurements, also

production and destruction terms are provided by EASY. This output was used to simply calculate the net O_x production rates by adding the production terms of O_3 and NO_2 and subtracting the corresponding destruction terms. A correction for the dilution was done by adding the O_3 and NO_2 dilution rates to the net O_x production rate.

Exemplarily, the derived model quantities are presented for the illumination phase of the 22nd Sep 2005 isoprene degradation experiment in figure 4.10. It shows that the OH reactivity $\tau_{\rm OH}^{-1}$ of the air mass declines nearly parallel to the decrease of the initial VOC isoprene. The relative decrease of the OH reactivity, however, is not that ample as the relative isoprene decrease, as the degradation products, exemplarily the time profiles of MACR and MVK are shown, built up. They are very reactive against OH, too, and hence hold up a nonzero OH reactivity although the isoprene already is decomposed. As expected, the OH loss rate $v_{\rm OH}$ (= $\tau_{\rm OH}^{-1}\cdot[{\rm OH}]$) and the dilution corrected net O_x production $\frac{d[O_x]}{dt}+{\rm DIL}(O_x)$ strongly correlate, which is obvious by comparing the almost parallel proceeding time series and by the correlation plot giving $\frac{d[O_x]}{dt}+{\rm DIL}(O_x)$ over $\tau_{\rm OH}^{-1}\cdot[{\rm OH}]$ (lowest right panel of figure 4.10). The slope of a fitting line in this last plot corresponds to the integrated amplifying factor $F_{\rm OH}$.

A correlation plot of the last mentioned parameters for the whole data set, which consists of 5261 data points, to determine F_{OH} is provided in figure 4.11. A regression line was calculated by linear least square fit. The slope of the regression line and therewith the value for the integrated amplifying factor for biogenic dominated air masses was determined to be 1.27 ± 0.01 . The net O_x production and the OH loss rate showed to be clearly correlated with r = 0.87, although the data scatter a lot. Nearly 300 data points of the observed net O_x production rates exceed twice the OH loss rate, thus even pass the idealized VOC degradation amplifying factor of two, and about 900 O_x production data points remain under once the corresponding OH loss rate. Higher values emerge, when cascading effects, like the one discussed in the previous subchapter for the MACR degradation, take place. Organic peroxy radicals RO2 do not built oxy radicals RO while oxidizing NO towards NO₂, as in the idealized VOC degradation mechanism, but new RO2 radicals, which once more oxidize NO. Additionally, previously built up PANs can degrade without the need of an OH reaction, release NO₂ and peroxy radicals and thus rise the O_x production. On the other hand, building up of the PANs and other chain terminating reactions, presented in chapter R2.24, lower the yield of O_x produced per initial OH reaction. To the end of each analyzed experiment, the remain air mix was dominated by HCHO, which produces only one NO₂ per OH attack on average. Radical loss processes lower the yield of O_x per OH attack below one, then. The slight positive axis intercept of $0.23 \pm 0.06 ppb/h$ indicates, that O_x production need not to be induced by OH-VOC reactions, but also takes places in times of no OH reactions, e.g. degradation induced by ozonolysis. As only illuminated phases of the experiments were analyzed, the zero and even negative OH values provided by the DOAS measurements have to be attributed to the dispersion of the DOAS instrument at OH values

2005-09-22 Time [UTC] Time [UTC] 10:00 12:00 12:00 14:00 10:00 14:00 1.0 Isoprene [ppb] 0.8 MACR [ppb] 0.6 0.4 0.2 0 2.0 1.5 MVK [ppb] 1.0 0.5 0.0 τ_{OH}-1 x [OH] [ppb/h] 25 $\tau_{OH}^{-1} [s^{-1}]$ 20 15 10 25 25 $d[O_x]/dt + DIL(O_x) [ppb/h]$ $d[O_x]/dt + DIL(O_x) [ppb/h]$ 20 15 10 10:00 12:00 14:00 10 τ_{OH}^{-1} x [OH] [ppb/h] Time [UTC]

Figure 4.10: Time series of the defining parameters for the integrated amplifying factor derived from the MCM model run of the 22nd Sep 2005 SAPHIR chamber experiment. The OH reactivity $\tau_{\rm OH}^{-1}$ (third row, left panel) decreases with the amount of VOCs (uppermost row and second row, left panel) and their reactivity against OH. The OH concentration (second row, right panel) rises with decreasing OH reactivity. Net O_x production (lowest row, left panel) and OH loss rate $(\tau_{\rm OH}^{-1} \cdot [{\rm OH}],$ third row, right panel) are strongly correlated, which is striking in the correlation plot of both quantities (lowest row, right panel).



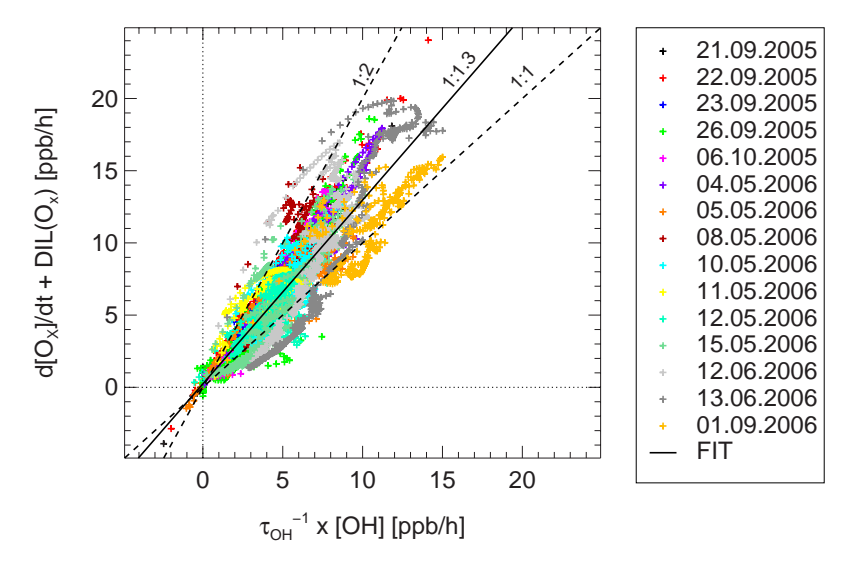


Figure 4.11: Correlation between the net O_x production and the OH loss rate for all experiments. The data scatter around a regression line with the slope of 1.27, which corresponds to the value of the integrated amplifying factor. Even values above the idealized factor of two for the OH induced VOC degradation and below the idealized factor of one for the CO oxidation emerge. Lines with the matching slope of one and two are given by dashed lines.

4.3.3 Results and Discussion

The determined factor F_{OH} of 1.27 ± 0.01 was applied to GC sampling time averaged data for a comparison with the approaches described previously. Therefore half an hour arithmetic means of the modelled OH concentrations and the OH loss rate were determined. The averaged model net O_x production was determined the same way as described for the measured O_x time series at the beginning of this chapter. A correction for the dilution was also done like described there. As only model data were used for both time series, no additional model error was introduced, but just the standard deviations adjusted by the averaging process, were applied.

A correlation plot for the averaged values is given in figure 4.12. It can not be used as an independent test of the approach, as the same data were used for the determination of the integrated amplifying factor F_{OH} , which is used for the calculations in this plot, but just as a consistency check, which is passed successfully. The averaged data set consisting of 96 data point shows still a high correlation (r = 0.84). A linear least square fit yields a slope of the regression line of 0.94 ± 0.05 and a standard deviation of $\sigma = 1.6ppb/h$.

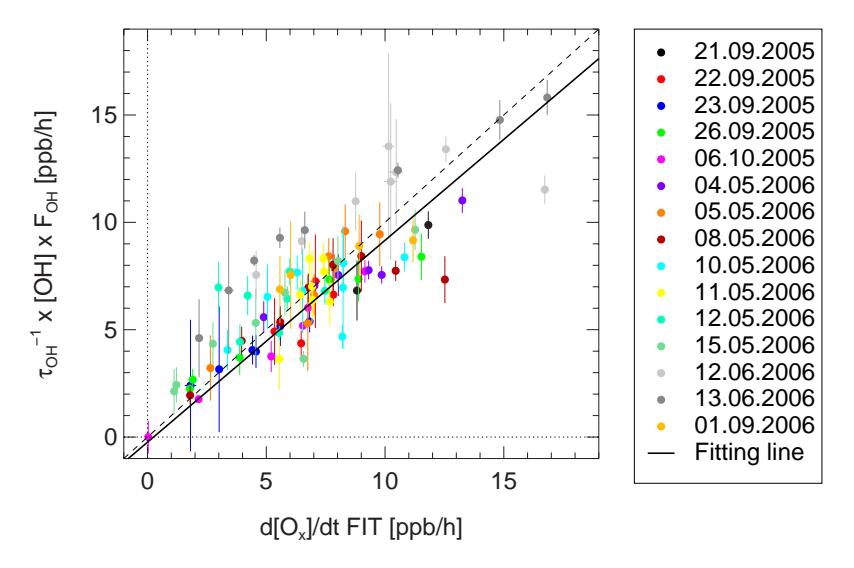


Figure 4.12: Averaged OH loss rate times amplifying factor over mean net O_x production.

Further test have been carried out, to analyzed the possible dependencies of the integrated factor, which have already been mentioned in subchapter 4.3.1. To do so, the original 60sec time step data set was used and F_{OH} was calculated for each data point by dividing the respective dilution corrected net O_x production by the corresponding OH loss rate. Numerical roundoff errors, occurring when dividing by very small according to amount OH loss rates, bring in a positive bias in the following analysis concerning $J(O^1D)$, NO_x and O_3 dependence, as much more small positive loss rates contribute to the analysis as negative ones. Outliers of F_{OH} values above about 4 and below zero can be attributed to the roundoff errors completely, which is demonstrated in figure 4.13.

The findings of the dependency analysis are summarized in figure 4.14. The $J(O^1D)$ photolysis frequency showed to be no influencing factor for F_{OH} , shown in the upper left panel of figure 4.14, including the horizontal regression line. No correlation between $J(O^1D)$ and F_{OH} exists (r = -0.01).

A $\mathrm{NO_x}$ dependence of the amplifying factor could also not be found (figure 4.14, upper right panel). It has to be considered though, that the setup of the experiments caused the highest (about 20ppb) and lowest (0ppb) $\mathrm{NO_x}$ concentrations to always occurred at the beginning of the experiments, with the "fresh" VOC mix. Low $\mathrm{NO_x}$ levels can not be reached with "older" air masses inside the SAPHIR chamber, as the HONO source causes an unpreventable rising of the $\mathrm{NO_x}$ concentration up to approximately 2ppb. As the HONO source does not compensate for the dilution of high $\mathrm{NO_x}$ levels on the other side, these decrease during experiments with a high starting level unless it is refilled by new gas injections. As the original intention of the experiments did not include the analysis carried out here, no refilling was done, however. The

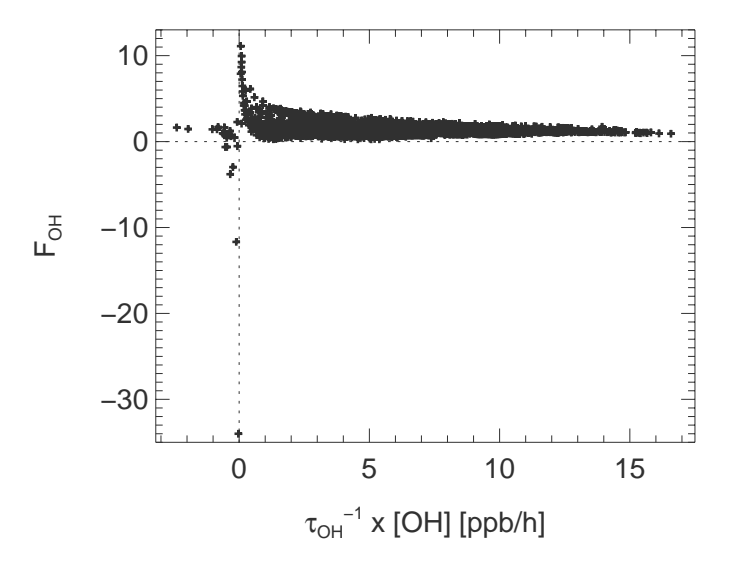


Figure 4.13: Roundoff errors occurring if F_{OH} is calculated by division of instantaneous O_x production rates by instantaneous OH loss rates and not by use of a regression line slope. At very small values according to amount of the OH loss rate unrealistically high values of the amplifying factor are calculated.

aging of the air mass influences F_{OH} , which is shown in the following. Thereby the analysis concerning NO_x is biased. To find out a trend, which probably would not be linear anyhow, a better coverage of the NO_x range of interest, including the very high an low regions, with air masses of different ages are desirable. At least, it can be concluded, that the factor does not change significantly with moderately high NO_x levels, as the mean value of the 10-20ppb NO_x experiments is equal to the one of the low and medium NO_x ranges, about 1.34.

A clear dependence on the ozone concentration seems to exist (bottom left panel of figure 4.14). Once more the realization of the experiments has to be taken into consideration, when interpreting this trend. All experiments started with no ozone inside the chamber, thus the initial VOC only met zero to medium ozone levels. During the degradation of the VOC and the building up of the less O_x productive species HCHO and CO the ozone increases. Thus, this trend is biased by the photochemical aging of the chamber air. As the plot of F_{OH} over elapsed experiment's time, which is shown in the bottom right panel of figure 4.14, shows the same trend, a separation between both influences is not possible with the present data set. Additional experiments with a nonzero ozone initial value are necessary for that. Even though the dependence is unclear, it has to be noted, that the trend line for both plots decreases from 1.80 (1.70) at zero ozone (starting time) to 0.81 (0.86) at the maximum reached ozone (maximum reached experimental time).

Although the integrated amplifying factor F_{OH} showed some dependencies,

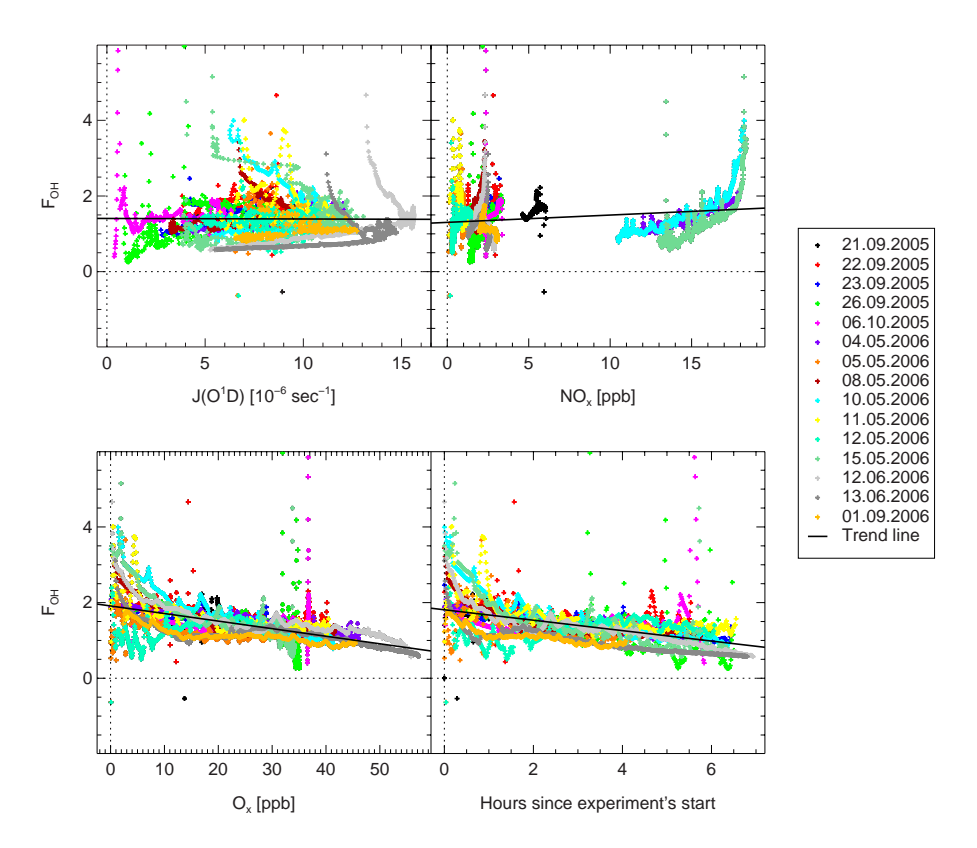


Figure 4.14: Dependencies of the integrated amplifying factor F_{OH} on different parameters supposed to be of importance. No dependency of F_{OH} on the $J(O^1D)$ can be found, which is demonstrated in the upper left panel, where F_{OH} is plotted over the mentioned photolysis frequency. No obvious NO_x dependence, shown in the upper right panel, could be found as well, probably just because of the experimental setup (see text). This setup also is the main influence for the observed dependence of F_{OH} from the ozone concentration, as high concentrations always correspond to long lighting periods (bottom left and right panel, respectively).

especially on the aging of the air masses, the method may, nevertheless, be useful as a proxy to estimate the photochemical O_x production. During SAPHIR chamber experiments the aging is in a way the extreme case, cause except for the HCHO source no VOCs are emitted in between. In natural atmospheres, however, isoprene is permanently emitted by vegetation during daytime, with varying, temperature and solar radiation dependent magnitude [141, 142, 143]. Due to the fresh emissions and the fact, that remains of degraded trace gases from previous days may still reside in the morning air, the aging of natural air masses can not be that pronounced.

In the SAPHIR chamber experiments, the averaged factor F_{OH} varied between 1.8 in the entirely new air mix and 0.8 in the aged air mix for biogenic (isoprene and its main degradation products) dominated air, which is within about $\pm 40\%$ of the mean value 1.27. As explained above, these variation limits are probably overestimated by a least 5% due to numerical roundoff errors. If additionally assuming the reduced aging in natural air to account for a 10% less variability, the mean F_{OH} value would vary within $\pm 30\%$, which is comparable to the error estimate of fully time dependent gas phase chemistry models, as described in subchapter 4.1.

The $F_{OH} \cdot v_{OH} = P_{O_x}$ approach hence shows promising. A multitude of analyses are indeed necessary, before the method can be granted to be reliable as a proxy to estimate the photochemical O_x production. These studies should include SAPHIR experiments with:

- anthropogenic VOCs dominated air with a high CO part.
- real OH lifetime measurements instead of model derivations of the OH reactivity.
- nonzero initial ozone conditions.
- naturally aged air, for example by filling in of ambient air at the afternoon
 of a highly photochemistry active day.
- high and low NO_x levels with aged air.

If these test are passed successfully, the proxy method would still be incomplete, as only two cases of air mixtures, dominated by biogenic and anthropogenic VOC emissions, respectively, would be covered. Therefore an additional (proxy) method is needed to estimate the ratio between anthropogenic and biogenic emissions. Such proxy methods have already been proposed. One example, as already mentioned in the introduction subchapter 1.4, is to use the ratio of different PANs, which have the same precursors as tropospheric ozone (compare chapter 2). In particular, peroxypropionic nitric anhydride CH₃CH₂C(O)OONO₂ (PPN) is supposed to be formed virtually only from anthropogenic compounds such as 1-butene and alkanes, whereas on the other side MPAN is solely derived from MACR and thus isoprene, which overwhelmingly is of biogenic origin. The MPAN to PPN ratio hence was used by Williams et al. 1997 [55] and Roberts et al. 1998 [56] to estimate the importance of biogenic versus anthropogenic VOCs concerning ozone production.

For an appropriate interpretation of the MPAN / PPN ratio, the production and destruction processes of both have to be well understood. Tests of the current knowledge of the MACR degradation and thus MPAN production have therefore been made in the SAPHIR chamber. The studies are presented in the following chapter.

4.4 Conclusion

When comparing the three approaches of the preceding subchapters for determining the photochemical O_x production of an air mass, at first glance the fully time dependent MCM model run shows the best performance, as the calculated net production rate does not significantly differ from the rate experimentally derived (slope of the regression line $m\pm\sigma(m)=1.28\pm0.20$ and 1.29 ± 0.21 for the zero and 600ppb model run respectively). As already mentioned, this good performance, however, needs well defined, thus measured initial conditions and sources and sinks of the participating trace gases known beforehand. For field experiments, such a fully time dependent approach is not feasible therefore.

The FDS approach on the other side is applicable to field experiments. The slope of the regression line for the whole data set (1.34 ± 0.19) is comparable to the one of the fully time dependent model run. For the chamber experiments with MACR as the initial VOC, the FDS approach performance, however, is quite bad, which can be traced back to the building up of PANs. The general impression of the FDS approach impairs for this partly bad performance. In nature, however, contrary to the artificial conditions inside SAPHIR, no air with MACR, which quasi completely stems from isoprene degradation, as the initial VOC exists. Additionally, smoother changes in the illumination occur. The subset of experiments with isoprene as the initial VOC therefore is more representative for natural air masses. The regression line slope of 0.95±0.25 between measured and modelled net O_x production even is nearer to one than in case of the fully time dependent model runs. A high effort for the measurements of as much as possible trace constituent ("fuels") is, however, required for this approach, as it would as well be for the initial conditions of a fully time dependent model run. As during field campaigns measuring instruments for some VOCs and OVOCs are not available or even do not exist at all, such a complete chemical characterization of air masses is not possible. The FDS approach hence tends to underestimate the real net O_x production rate due to the lacking of "fuel" measurements.

The $\tau_{\rm OH}$ approach has got the advantage of being experimentally much less expensive than the FDS approach. Two measuring instruments for the OH concentrations and the OH lifetime are sufficient. The attraction of the approach lies in the fact, that no undetected "fuels" may disturb the approach's performance, as due to the integrating feature of the $\tau_{\rm OH}$ quantity, all "fuels" are indirectly measured. No independent testing of the approach was possible until now. During the consistency check a slope of the regression line of 0.95 ± 0.05 was achieved, which is quite promising.

No final statement on the best or poorest approach can be given so far, as

CHAPTER 4. OZONE PRODUCTION DUE TO ISOPRENE DEGRADATION

such a ranking strongly depends on the requirements concerning the model output and input, hence its applicability. Additionally, the $\tau_{\rm OH}$ approach has not been tested widely enough to evaluate whether its $\rm O_x$ prediction performance is potentially comparably good the one of the FDS approach. Anyway the $\tau_{\rm OH}$ approach needs much less measuring effort and yields a higher time resolution. Much less error-prone measurements have to be combined for it and no gaps in the air masses characterization exists.

5 Methacrolein Degradation Studies

In the previous chapter, the focus concentrated on the photochemical ozone production caused by isoprene degradation. Among other things, it has been pointed out there that

- 1. MCM model runs yield good results concerning ozone production,
- product yields for the degradation products MACR and MVK are underestimated by the MCM,
- 3. good performance concerning ozone does not mean, that the mechanism is correct in all details, but that errors may cancel out each other, and
- 4. the production and destruction rates of PANs are strongly influencing the effective O_x progress.

As the production of PANs is quite important during the MACR degradation, the combination of the 2nd and 4th point may be crucial. Therefore in this chapter the degradation of MACR is looked at in more detail, especially with a deeper look on the PANs and the $\rm NO_x$ budget. Not only the OH-induced degradation was looked at, but also the other possible initializations by photolysis, ozonolysis, and $\rm NO_3$ attack were analyzed, as the chemistry following these initializations are quite similar, but emphasize different aspects of the degradation mechanism to differing extents.

5.1 OH Induced MACR Degradation

Five experiments dealing with the OH induced degradation of MACR in the SAPHIR chamber, with, beside the meteorological conditions and photolysis frequencies, at least the trace gases MACR, NO, NO₂, O₃, OH, and HCHO measured, have been conducted between Oct 2005 and Sep 2006. They are listed in table B.2. Especially for the medium NO_x (between 2 and 3.5ppb) experiments, the MCM model runs could not reproduce the time series of the measured NO_x, which is illustrated in figure 5.1, third row. During the first few hours of the experiments, the model NO_x decreases and therewith negatively deviates from the measurement to about an ppb difference. After passing a minimum, the model NO_x increases and reaches the measurements again with a good correspondence in the following. The measurements showed no decrease in the beginning, but a constant to rising level. The whole figure is described in detail in chapter 5.1.2.

The effect was first observed at the experiment carried out at the 6th October 2005 and was reproduced in two following experiments at the 13th June 2006 and 1st September 2006. The realization of the Oct 2005 and June 2006 experiments has already been described in the preceding chapter. The last experiment was carried out in the same way: flushing of the chamber with synthetic air over night until $\mathrm{NO_x}$ and ozone were below LoD. With the roof still closed, the air was humidified to about 65% relative humidity, and MACR and $\mathrm{NO_2}$ were injected. Two GC measurements were awaited and subsequently the roof was opened. After about 4 hours, the roof was closed again.

5.1.1 Used MCM Model

The MCM subset for the MACR degradation, which is a subset of the isoprene degradation mechanism listed in the appendix A.4, completed by the chamber specific reactions for dilution, background reactivity, wall deposition and the HCHO and HONO sources was used to model the experiments. The initial MACR concentration of the model runs were adjusted to the amount of liquid MACR injected into the chamber (compare chapter 4.1.1 equation 4.1).

When looking at the $\mathrm{NO_x}$ budget, especially the HONO source is a crucial parameter, as well as possible HONO impurities of the water used for the humidification, as for example observed at the standard experiment of the 31st Aug 2006 shown in chapter 3.1.5. For the three experiments studied in this chapter, no combination of both model parameters yielded in a good $\mathrm{NO_x}$ correspondence between model and measurements. This is demonstrated in figure 5.2. Due to the difficulty in adjusting the HONO source and therewith the primary OH production correctly, the MCM model runs presented here were constrained by using DOAS OH measurements as model input.

In figure 5.2, the NO_x measurements during the illumination of the chamber (blue crosses) of the 6th Oct 2005 are shown exemplarily. Different MCM model runs with varying HONO chamber sources and impurities are plotted in addition, which were selected by at least representing the starting and ending value of the shown interval quite well. A source term of 1.0 corresponds to a HONO source constant K of $4.7 \cdot 10^{13} cm^{-3}$ in equation 3.3, which is called the standard source in the following. Without applying an impurity of HONO introduced by the humidification, a HONO source term of 1.6 times the standard source is needed to at least reach the measured NO_x concentration at the end of the illumination phase (lilac line). When allowing for a already quite high impurity of 0.8ppb (factor 1.6 given in the legend of figure 5.2) directly before the roof is opened, the HONO source has to be scaled down towards 1.3 standards to get the final correspondence again (pink line). The deviation between this model run and the measurement is improved compared to the one described before. A further increase of the impurity toward anyway unrealistic values and a simultaneous down scaling of the HONO source, however, does not bring any further improvement. The negative deviation decreases at the cost of an emerging positive deviation at the beginning of the illumination phase (green to black line).

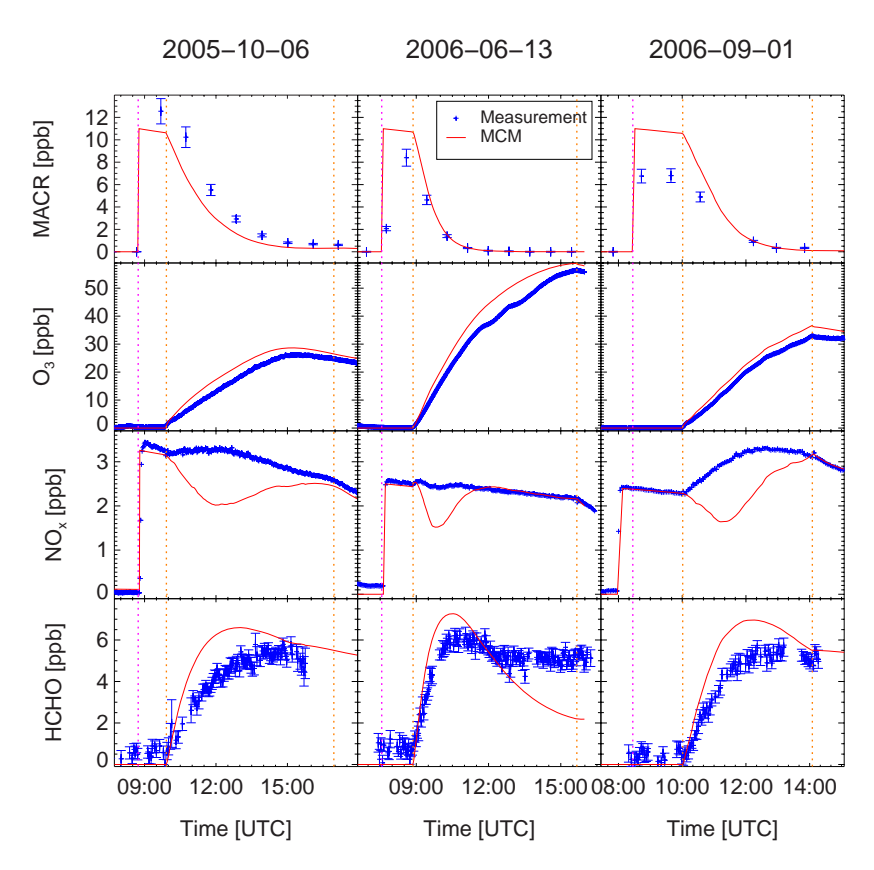


Figure 5.1: NO_x discrepancy at the OH induced MACR degradation. Measured time profiles for MACR (PE-GC), ozone (UV for the 6th of Oct 2005, CL for the following experiments), NO_x (CL), and HCHO (DOAS) are given by blue crosses. The MCM model runs (red lines), which are in detail described in chapter 5.1.1, represent the trends of the MACR measurements and the ozone measurements quite well. An obvious discrepancy exist between modelled and measured NO_x time profiles. The models overestimate the measured HCHO concentrations in the beginning even without applying a chamber HCHO source.

The injection times of MACR and NO_2 are marked with pink dashed lines for each day. The chamber roof was open between the times marked with orange dashed lines.

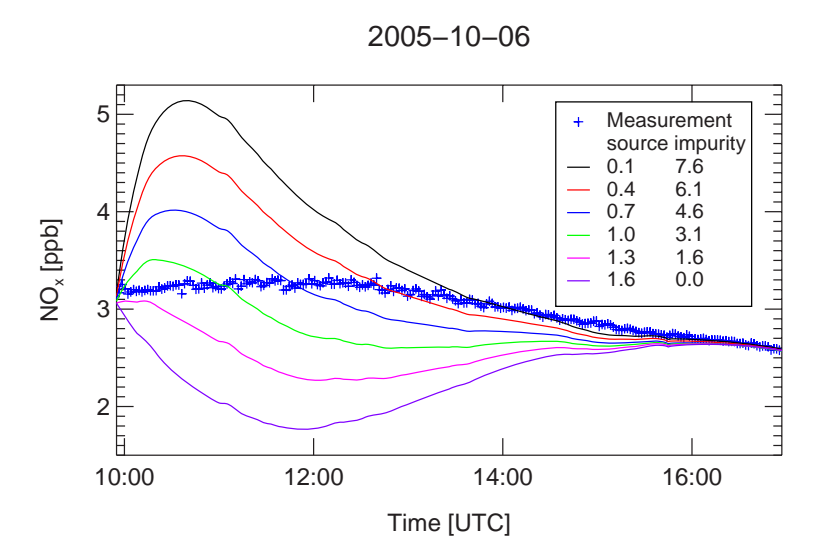


Figure 5.2: Comparison of the NO_x time series for different MCM model parameters of the HONO chamber source and of HONO impurities in the water for the humidification. Shown are the data of the 6th Oct 2005 during the illumination of the chamber. All model series were chosen to nearly have the same initial and final NO_x concentration. When no water impurity is assumed, the negative NO_x deviation is biggest (lilac line). When applying a slight impurity, the deviation gets smaller (pink line). However, a further rising of the impurity and even allowing for unrealistically high values (green to black line) does not improve the model performance any further, but results in an initial overestimation which is followed by a still present underestimation. A source term of 1.0 corresponds to a scaling factor K in equation 3.3 of $4.7 \cdot 10^{13} cm^{-3}$, an impurity of 1.6 to an initial HONO concentration of about 0.8ppb at the starting time, when the chamber roof is opened.

For the model runs of the first and second experiment in figure 5.1, the specific combinations of HONO source and impurities were selected in a way, that the negative deviation was smallest without any positive deviation in the beginning (approximately represented by the pink run of figure 5.2). As a standard experiment was carried out on the 31st Aug 2006 (presented in chapter 3.1.5), where the HONO impurity inside the humidification water could be estimated from, this value could be applied to the 1st Sep 2006 experiment and just the chamber HONO source was adjusted. Motivated by this standard experiment, additional chamber sources for photolytic acetaldehyde and formic acid were introduced into the 2006 model runs. The acetaldehyde source was adjusted during the 31st Aug 2006 standard experiment to represent the PAN measurements within their error margins, which resulted in a source strength of

$$S_{CH3CHO} = K_{CH3CHO} \cdot (10^6 + 1.4 \cdot 10^5 RH) cm^{-3} sec^{-1}$$
 (5.1)

with the scaling factor K_{CH3CHO} being 0.6. The formic acid source was approximated by

$$S_{HCOOH} = K_{HCOOH} \cdot (10^6 + 2.5 \cdot 10^5 RH) cm^{-3} sec^{-1}$$
 (5.2)

with $K_{HCOOH}=0.45$. In both equations the relative humidity RH is given in %.

The HCHO concentration is mainly influenced by the MACR degradation. It was measured by the DOAS instrument. The HCHO chamber source could thus be adjusted as good as possible by varying the pre factor of equation 3.8. As the MCM model runs already exceeded the HCHO measurements, no additional chamber source was applied. The background reactivity was scaled to approximate the model ozone to the ozone measurements. The chosen model parameters are listed in table 5.1.

5.1.2 Observations

In the uppermost row of figure 5.1, the MACR concentrations are given over time. The trend of the Perkin Elmer GC measurements (blue crosses) are quite well represented by the MCM model (red line) for all experiments. An overestimation of the GC measurements by the model can be found for the first experiment. The only reasonable explanation for this general high measurements during this day are problems with the calibration. For the second and third experiment, the measurements lie below the model systematically. This may be caused by unknown losses on the way from the injection septum into the chamber or by a bias of the GC instrument. This last mentioned option seems more realistic, as otherwise very high background reactivities (above around 500ppb CO equivalents) have to be chosen in the model to reproduce the ozone measurement time profiles. The ozone time profiles are shown in the second row of figure 5.1. For the 6th Oct 2005 experiment, the ozone is slightly overestimated by the model, although no background reactivity was assumed. For the 13th June and 1st Sep 2006 experiments, the measured ozone

Table 5.1: MCM model parameter for the OH induced MACR degradation experiments. Given are the scaling factor K_{HONO} for the standard HONO source of equation 3.3 and the HONO impurity introduced by the humidification just before the chamber roof is opened, which are both important for the total amount of NO_y in the chamber. The scaling factor K_{HCHO} replaces the constant pre factor $3.1 \cdot 10^{-3}$ in equation 3.8. The fourth parameter is the background reactivity Y given in ppb CO equivalents. For the experiments in 2006 in addition, chamber sources for acetaldehyde and formic acid were applied. Given are the scaling factors K_{CH3CHO} and K_{HCOOH} for equation 5.1 and 5.2, respectively.

date	2005-10-06	2006-06-13	2006-09-01
$K_{HONO} [4.7 \cdot 10^{13} cm^{-3}]$	1.3	1.1	2.0
HONO impurity $[ppb]$	0.8	0.7	0.6
$K_{HCHO} [3.1 \cdot 10^{13} cm^{-3}]$	0.0	0.0	0.0
Y [ppb CO]	0	350	100
K_{CH3CHO}	_	0.6	0.6
K_{HCOOH}	-	0.45	0.45

profiles are quite well represented by the model with normal background reactivities. Especially when taking the bad model performance concerning the $\rm NO_x$ concentrations into consideration, the simultaneous, comparatively good ozone conformity is astonishing.

As described at the beginning of this chapter, the model $\mathrm{NO_x}$ concentration starts to strongly decrease as soon as the chamber roof is opened. It reaches a minimum, at least about one ppb below the measurements, starts increasing thereafter, and finally reproduces the measurements quite well again. The $\mathrm{NO_x}$ measurements, however, show no decrease at all.

As the model NO_x discrepancies do not constantly increase during the whole experiments, but decrease autonomously again, it is assumed, that an instable temporary NO_x reservoir is built up from any degradation products of the MACR in the model. When the MACR is degraded and the concentration of the reservoir precursor decreases, the decomposition exceeds the production of the reservoir, and the NO_x is released again. When looking at the main paths of the OH induced MCM MACR degradation, which has already been presented in chapter 4.2 figure 4.9, two NO_x reservoir substances of the needed kind can be identified, namely the peroxy acyl nitrate species MPAN and PAN. Their model concentrations reached correspond to the magnitude of the NO_x discrepancy. No other NO_x containing species could be found in the mechanism, which reaches a corresponding order of magnitude and a similar time profile. Therefore it was assumed, that the MPAN and / or PAN yields of the MCM are incorrect.

In addition, the model formaldehyde concentrations overestimate the DOAS measurements in the beginning of each experiment without applying any cham-

ber HCHO source. As for the $\mathrm{NO_x}$ discrepancy, the HCHO deviation is not uniform and decreases autonomously. At the 13th June 2006 experiment, the model even underestimates the measured values in the second half of the experiment.

To get to the bottom of the discrepancy, first of all the IUPAC recommendation for the MACR + OH reaction was checked [144], together with some of the references given therein [145, 146]. Although the MCM claims to use this recommendation, a difference between both supposed mechanisms exists. The least crucial difference is the slightly changed rate coefficient for the initial reaction

$$MACR + OH \longrightarrow products$$
 (R5.1)

which is

$$k_{R5.1}(MCM) = 1.86 \cdot 10^{-11} \cdot \exp(175K/T)cm^3 sec^{-1}$$
 (5.3)

in the MCM, while IUPAC recommends

$$k_{R5.1}(IUPAC) = 8.0 \cdot 10^{-12} \cdot \exp(380K/T)cm^3sec^{-1}.$$
 (5.4)

In the temperature range of interest, both values differ by at most 15%, which is illustrated in figure 5.3.

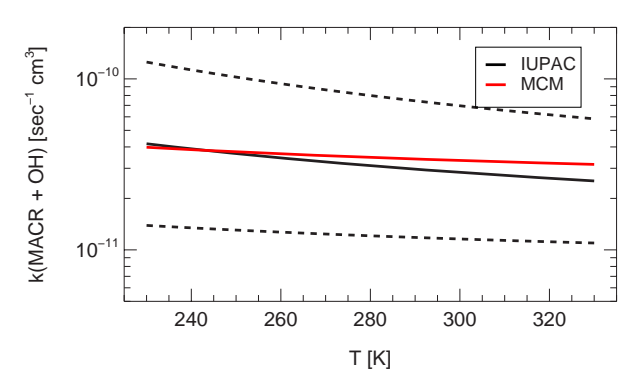


Figure 5.3: Rate coefficients used by the MCM and recommended by IUPAC for the MACR + OH reaction.

The difference between the MCM and the IUPAC recommendation, which is much more critical, is the fate of the radical products for the H-atom abstraction and OH-addition branches of the MACR + OH reaction. The main IUPAC reaction scheme is provided in figure 5.4, the MCM reaction scheme, as said before, has already been shown in chapter 4.2, figure 4.9.

At the upper path (OH-addition to one double bond of MACR), the MACRO radical decomposes exclusively to hydroxy acetone and formaldehyde (ACE-TOL + HCHO) in the MCM model, whereas two possible decomposition pathways are given in the IUPAC model with hydroxy acetone, a hydroperoxy radical, and carbon monoxide (ACETOL + HO $_2$ + CO) as products or methyl

glyoxal, formaldehyde, and carbon monoxide (MGLYOX + HCHO + CO). Methyl glyoxal and formaldehyde are also formed from the second oxy radical of the OH-addition pathway (OCH₂C(OH)(CH₃)CHO), which is not used in the MCM at all. As ACETOL has a longer atmospheric lifetime than MG-LYOX, the further degradation and thus PAN production of this degradation branch is slower in the case of the MCM compared to the IUPAC recommendation. No branching ratio is given for the MACRO decomposition into ACETOL or MGLYOX for the IUPAC mechanism. The further degradation of ACETOL and MGLYOX is not provided in figure 5.4 for clarity reasons. In the EASY implementation of this mechanism, their degradation is taken from the MCM. The main degradation products of both species are hence shown in figure 4.9.

The lower path in both figures shows the degradation following a H-atom abstraction. In each case MACO3 is built, which is the precursor of the intermediate NO_2 and peroxy radical reservoir methacryloylperoxynitrate (MPAN). If the MACO3 does not form the MPAN, but oxidizes NO to NO_2 , the MCM supposes CH3CO3 + HCHO to be formed, whereas the IUPAC recommends $CH_2=CCH_3+CO_2$ as additional products. The CH3CO3 radical is the precursor of PAN, which can hence be formed rapidly in the H-atom abstraction branch of the MCM mechanism, as only radical reactions take place after the initial OH reaction. The final first degradation step product of this branch in the MCM is one more formaldehyde, hence altogether two formaldehyde molecules are formed per MACR degrading via this branch. The reactions were already listed in chapter 4.2 (reactions R4.1 - R4.4). As a review reaction R5.2 gives the summation of this four reactions in the MCM:

$$MACO3 + 3 NO \xrightarrow{O_2} 2 HCHO + CO_2 + 3 NO_2 + HO_2$$
 (R5.2)

In the IUPAC recommendation no PAN can be formed via the H-atom abstraction path at all, as the CH₂CCH₃ radical subsequently formed is no precursor of PAN. The CH₂CCH₃ radical rather decomposes into CO₂, CO, and one HCHO. The individual reactions are:

$$MACO3 + NO \longrightarrow CH_2 = CCH_3 + NO_2 + CO_2$$
 (R5.3)

$$CH_2 = CCH_3 + O_2 \longrightarrow HCHO + CO + CO_2$$
 (R5.4)

and yield the effective reaction in the IUPAC recommendation:

$$MACO3 + NO \xrightarrow{O_2} NO_2 + CO + HCHO + 2 CO_2$$
 (R5.5)

5.1.3 Results

A new EASY model was set up to represent the differing IUPAC recommendation. The MCM model was still used as the basis and just the changes listed in table 5.3 at the end of this chapter were implemented. The new pseudo IUPAC

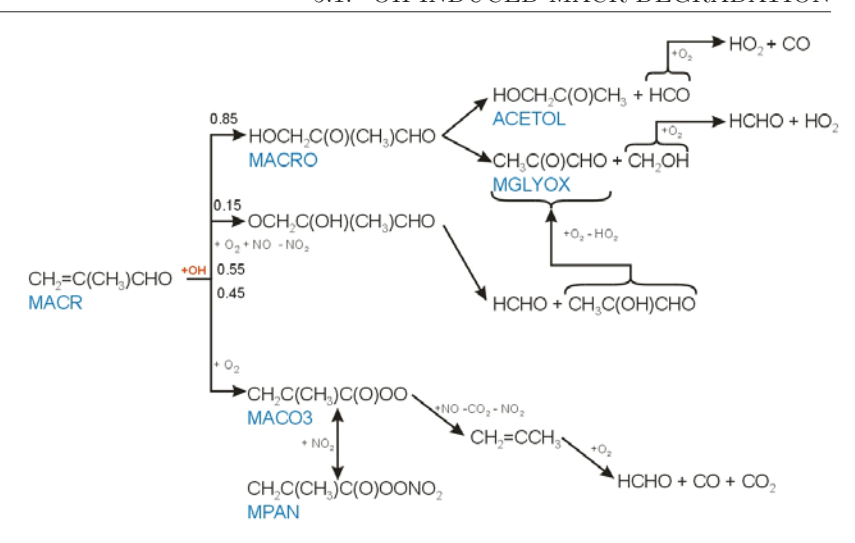


Figure 5.4: Main reaction scheme recommended by IUPAC for the MACR + OH reaction. Black letters give the species' names in IUPAC nomenclature, where available the differing MCM names are given in blue letters. The further degradation of hydroxy acetone (ACETOL) and methyl glyoxal (MGLYOX) are not given for clarity reasons. In the EASY implementation of this mechanism, their degradation steps are taken from the MCM.

model is denoted as 'IUPAC' in the following. A differentiation between both OH-addition pathways on the terminal (85%) or the second C-atom (15%) of the double bond was not done in the EASY implementation, as the products of the OCH₂C(OH)(CH₃)CHO radical are identical to MGLYOX path of the MACRO decomposition anyway. These both ways are hence lumped together and the branching of the MACRO decomposition cares for the additional path towards the MGLYOX + HCHO + HO₂ by being a least 15%. If an 50 : 50 branching for the MACRO decomposition is assumed, which was done as a first guess, this implies approximately a 40 : 60 ratio in the EASY implementation for the MACRO \longrightarrow ACETOL + HO₂ + CO reaction compared to the MACRO \longrightarrow MGLYOX + HCHO + HO₂ reaction.

When running this unaltered 'IUPAC' model for the different days and only adjusting the model parameters HONO and HCHO source, HONO impurity, background reactivity, and for the 2006 experiments formic acid and acetaldehyde chamber source (listed in table 5.2) in the same way as tried with the MCM model, the $\rm NO_x$ discrepancy nearly vanishes. This is demonstrated in figure 5.5. In the upper row of this figure, the MACR measurements and model concentrations are given over time. As the rate coefficient has been changed only slightly, no change is visible between MCM (figure 5.1) and 'IUPAC' model run. The ozone course is represented by the model slightly better, especially during the early stages of the experiments. The most obvious implication

of the model modification is the better, but still not perfect performance concerning the $\mathrm{NO_x}$ budget. Maximum model deviations from the measurements are reduced to about 0.4ppb or 15% now compared to up to 1.4ppb or 45% before. The formaldehyde concentration is also represented much better by the modified model: The initial overestimation is reduced and exceeds the error estimates of the HCHO measurements only slightly. The negative deviation on the 13th June 2006 is reduced, too.

Table 5.2: 'IUPAC' model parameters for the OH induced MACR degradation experiments. Explanations for the given parameters can be found at table 5.1.

date	2005-10-06	2006-06-13	2006-09-01
$K_{HONO} [4.7 \cdot 10^{13} cm^{-3}]$	1.3	1.2	2.0
HONO impurity $[ppb]$	0.6	0.5	0.6
$K_{HCHO} [3.1 \cdot 10^{13} cm^{-3}]$	0.3	0.5	0.5
Y [ppb CO]	300	400	200
K_{CH3CHO}	-	0.6	0.6
K_{HCOOH}	_	0.45	0.45

A further tuning of the 'IUPAC' model may yield even better conformances with the measurements. Especially the undefined branching of the MACRO decomposition is a yet free parameter. Measurements of ACETOL and MG-LYOX would help to define this ratio, but were not available for the presented experiments.

However, PAN measurements were performed during the 2006 experiments and at the last experiment even MPAN measurements. These measurements, additionally to the ones of NO_x , give a strong hint on the reliability of the used mechanisms. They are presented in figure 5.6 together with the MCM and 'IUPAC' model results. It can be seen that the MCM overestimates the PAN measurements on both days, whereas the 'IUPAC' represents them quite well for the first and very good for the second experiment. As was already clear by looking at both degradations schemes, the main difference in both implementations lies in the possible PAN building, which can hence be made responsible for the strong NO_x discrepancy of the MCM model.

The MPAN yield and time response, however, stays quite similar in both models, which additionally were approved by the MPAN measurements: both model estimates lie within the error margins of the measurements, the MCM at the higher and the 'IUPAC' at the lower limit. The MPAN production from the OH induced MACR degradation and, as it is an unstable adduct, also the daytime degradation thus seems to be quite well understood.

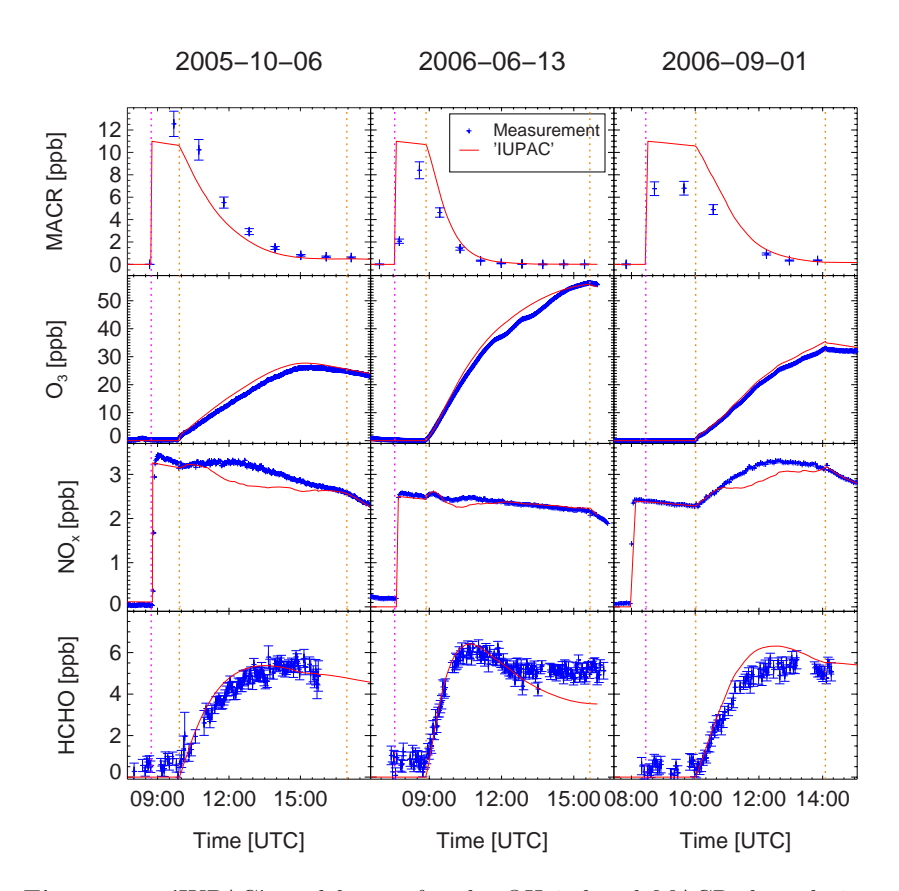


Figure 5.5: 'IUPAC' model runs for the OH induced MACR degradation. Given are measured (blue crosses) and modelled (red lines) time profiles for MACR (Perkin Elmer GC), ozone (UV for the 6th Oct 2005 and CL for the 2006 experiments), NO_x (CL), and HCHO (DOAS). No change between the MCM model run, presented in figure 5.1, and the 'IUPAC' model is obvious for the MACR concentrations. Slight improvements can be found for the ozone estimates, especially for the 13th June 2006 experiment, where the initial ozone production nearly perfectly corresponds to the measurements now. The NO_x discrepancy does not vanish completely, but is much smaller for each day. The formaldehyde measurements are much better represented, too.

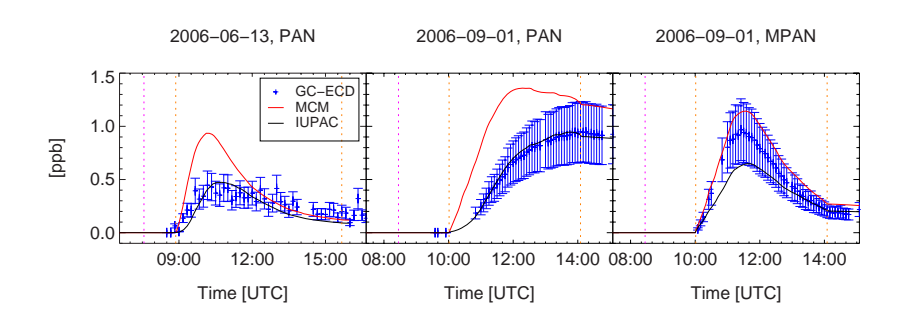


Figure 5.6: PAN and MPAN measurements compared to MCM and 'IUPAC' model predictions. The PAN measurements (blue crosses) on the 13th June 2006 (left) and 1st Sep 2006 (middle) experiments are both overestimated by the MCM model (red lines), up to nearly one ppb on the 1st Sep 2006 experiment. The 'IUPAC' model (black lines), however, represents the PAN measurements quite well for the 13th June 2006 and nearly perfectly for the 1st Sep 2006 experiment. Both MPAN model predictions lie within the error margins of the MPAN measurements on the 1st Sep 2006 (right panel). the MCM lies at the upper and the 'IUPAC' at the lower limit.

5.2 Photolysis and Ozonolysis of MACR

During daytime, not only OH-induced degradation of MACR takes place, but also photolysis and ozonolysis to a small extent. The latter is also important during nighttime, in addition to the NO_3 chemistry looked at in the next section. To further study the reliability of the PAN and MPAN model predictions, the photolysis, where the MPAN precursor MACO3 is supposed to be built, and the ozonolysis, where among others the PAN precursor MGLYOX is proposed to be formed, was looked at in an experiment carried out at 12th Apr 2007. Over night, the SAPHIR chamber was flushed until NO_{x} and ozone remained under the limits of detection for the specific specie. Then, 15ppb NO_2 , 7ppb MACR, and about 500ppm CO as a OH scavenger were added. After two GC measurements, the chamber roof was opened and the photolysis of MACR started. After about two hours additional ozone was added to enforce the ozonolysis.

5.2.1 Used Models

Three kinds of model runs were performed, each time completed by the same chamber specific reactions for the HONO source (source strength $K_{HONO} = 1.5$), formaldehyde source (source strength $K_{HCHO} = 0.2$), and background reactivity (Y = 200ppb CO equivalents):

1. unaltered MCM model

- 2. modified MCM model with a reduced MACR photolysis frequency by a factor 0.1.
- 3. 'IUPAC' model with the MACR photolysis frequency changed in the same manner as was done for the modified MCM model.

Only two studies exist about the photolysis of MACR, hence absorption cross section and quantum yields. They are not in good agreement. Cause of that, no recommendations on the products are given by IUPAC [147]. In the 'IUPAC' model, therefore the MCM assumptions were adopted. According to this, the MACR is uniformly photolyzed into MACO3 + HO2 and CH3CO3 + HCHO + CO + HO2. In the MCM, photolysis frequencies dependent on the solar zenith angle χ . For clear sky conditions they are parameterized by an expression of the form

$$J_{MCM} = l(\cos \chi)^m \exp(-n \sec \chi) \tag{5.5}$$

with $l=1.140\cdot 10^{-5}$, m=0.396, and n=-0.298 in the case of MACR [76]. For a simple adoption to inside SAPHIR conditions, at least a factor of 0.7 has to be applied to consider the transmission characteristics of the foils and girders. This factor has also been used in the model run called 'unaltered MCM'. The additional factor 0.1 was used for the model run called 'modified' or 'new J(MACR)' and for the 'IUPAC' model.

The main difference in the photolysis part of the degradation mechanism is the fate of the produced MACO3 radical, as described in the preceding subchapter. The 'IUPAC' EASY model implementation is schematically given in figure 5.7.

No changes concerning the MACR ozonolysis were made for the 'IUPAC' implementation compared to the MCM, as it already represents this recommendation. The mechanism is schematically given in figure 5.8. The degradation is quite complicated, as several branchings take place. Independent of the different pathes, in each case a CH3CO3 radical, the PAN precursor, is formed.

5.2.2 Results

Measurements and model runs of the 12th Apr 2007 experiment are compared in figure 5.9. From top to the bottom, measurements for MACR (Perkin Elmer GC), NO_x (CL), PAN, MPAN (both GC-ECD), and ozone (CL) are presented.

All different models show strong deviations from the MACR measurements. As the rate coefficient of the reaction

$$MACR + O3 \longrightarrow products$$
 (R5.6)

is known very well [148] the deviation is supposed to stem from problems in the ozone depletion of the GC caused by the very high ozone concentrations. With the original MACR photolysis frequency J(MACR), quite an amount of MACR is degraded via this process. The produced radicals would induce a

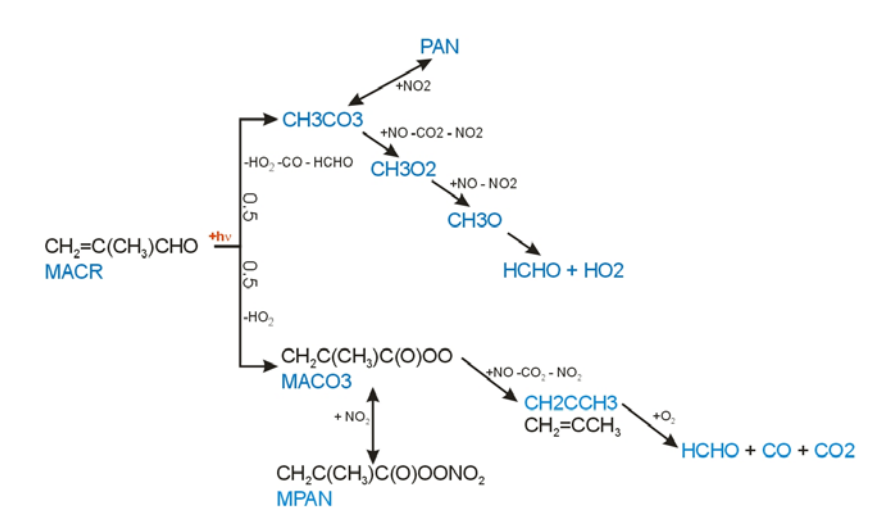


Figure 5.7: Reaction scheme of the MACR photolysis 'IUPAC' implementation. One branch yields the MPAN precursor MACO3, which can hence be built during the photolysis. In the upper branch, also the PAN precursor CH3CO3 is proposed to be built. In the MCM, the PAN precursor is built in both branches.

measurable ozone production. As the ozone production observed (lowest panel of figure 5.9), is nearly totally explained by the added OH scavenger CO, it was decided to scale down the anyway quite uncertain J(MACR) [147].

The MCM model with reduced J(MACR) thus shows a much better performance concerning the ozone. In this model, nearly no photolysis takes place any more. That is also the reason, why it is only slightly different from the 'IUPAC' model with reduced J(MACR). As mentioned before, the only difference between both models consist of the MACO3 fate, which is solely produced during the photolysis. In the ozone progress, no difference between the altered MCM and the 'IUPAC' can hence be seen.

As only very small amounts of PAN and MPAN are formed in any of the models, no difference in the NO_{x} time profiles can be seen, which all correspond to the measurements very well.

Differences between the altered MCM and the 'IUPAC' model become visible only slightly in their PAN and MPAN predictions. A little more PAN is built in the case of the altered MCM due to the additional possibility of also building PAN from the MACO3 photolysis path. Both overestimate the PAN measurements moderately. The MCM with the original MACR photolysis frequency highly overestimates the measured PAN yield. Beside the elevated ozone course, this is another indication for the overestimated photolysis frequency. The PAN measurements, however, could give no hint on the fate of the MACO3 radical, whether PAN is formed in the subsequent degradation or not, as the modified MCM and the 'IUPAC' model differ from each other and from the PAN measurements only slightly. Provided that the modified pho-

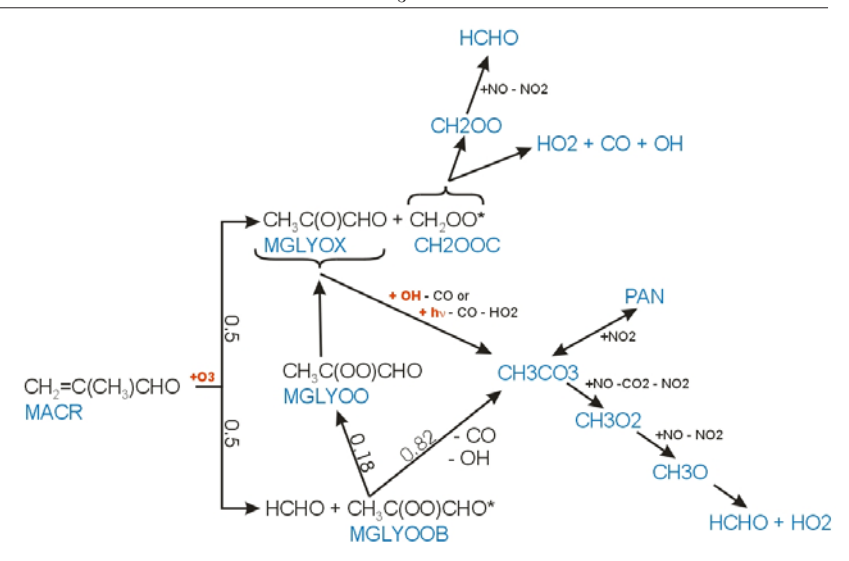


Figure 5.8: Reaction scheme of the MACR ozonolysis. Independent of the different branches, the PAN precursor radical CH3CO3 is formed in every degradation path.

tolysis frequency is correct, nearly no PAN is produced during the photolysis, but nearly all PAN descends from the ozonolysis, which appears to be fairly understood, so.

Only few measuring points laid over the LoD for the MPAN during the illumination phase presented in figure 5.9, fourth row. The 'IUPAC' and modified MCM overestimate this value by about a factor two, the original MCM by about a factor five. Due to the big uncertainties concerning the MACR photolysis, to which the MPAN yield is highly sensitive, a factor of two deviation between 'IUPAC' model and measurements still does not imply the model to be wrong. Especially when considering, that the photolysis frequency could only be adjusted indirectly by trying to bring the modelled and measured ozone concentrations to correspondence during the first part of the experiment, makes the deviation observed acceptable to still rely on the model. Unfortunately, no more direct measure, e.g. due to the lack of more reliable MACR measurements to cross check the photolysis frequency with the MACR degradation rate later on, were available.

5.3 NO₃ Induced MACR Degradation

During nighttime, OH and photolysis degradation processes lose importance, as no light is present and the OH concentration is reduced by orders of magnitude. Gas phase chemistry, nevertheless, takes place, as another radical, the

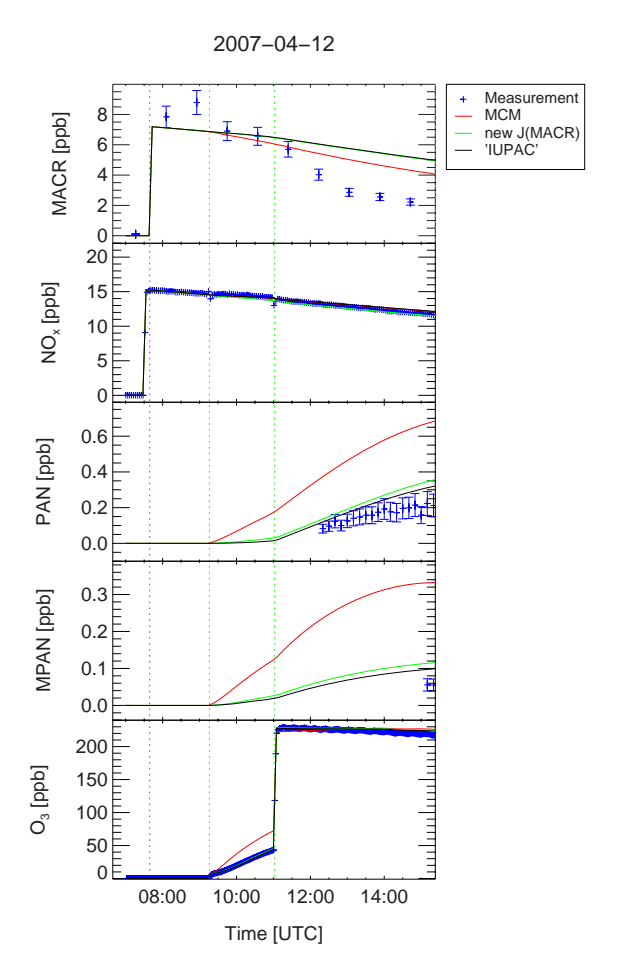


Figure 5.9: MACR photolysis and ozonolysis experiment on 12th Apr 2007. Shown are the measured time profiles for MACR (Perkin Elmer GC), NO_x (CL), PAN, MPAN (both GC-ECD), and ozone (CL) (blue crosses). They are compared to three different model runs (red, green and black solid lines), which are described in the text. The MACR measurements are very badly represented by each model, NO_x is estimated very well in each case. The PAN yield is strongly overestimated, when the photolysis frequency is not scaled down (original MCM model), but quite well represented with reduced J(MACR). MPAN was below LoD nearly all the time. As for the PAN the yield is overestimated only by the unaltered MCM model. Ozone is also well represented, except for the unaltered MCM during the photolysis.

The pink hatched line represent the injection time of MACR, NO₂, and CO, the orange hatched line the start of the illumination, and the green hatched line the time of an additional ozone injection enhancing the ozonolysis.

NO₃ is formed by reaction

$$NO_2 + O_3 \longrightarrow NO_3 + O_2$$
 (R5.7)

During daytime, this NO₃ radical is photolyzed via

$$NO_3 + h\nu \xrightarrow{O_2} NO_2 + O_3,$$
 (R5.8)

which is diminishing the impact of this radical in illuminated air. In darkness, NO_3 reactions mainly drive the chemistry. In first place, NO_3 induces the degradation of VOCs by H-atom abstraction:

$$RH + NO_3 \xrightarrow{O_2} RO_2 + HNO_3$$
 (R5.9)

and in the second place, NO_3 radicals substitute the NO molecules in reacting with the RO_2 radicals, as the NO concentration is nearly zero, cause no photolysis of NO_2 reproduces it:

$$RO_2 + NO_3 \longrightarrow RO + NO_2 + O_2$$
 (R5.10)

In case of MACR, it was supposed by *Warneke et al. 2004* [30] that during the nighttime MACR+NO₃ reaction a MPAN yield of nearly 100% can be expected, following the H-atom abstraction path of the MACR degradation already presented in chapter 5.1.

Two MACR nighttime chemistry experiments were carried out at SAPHIR at 13th Nov 2006 and 13th Apr 2007. As usual, the chamber was flushed over night until NO_x and ozone concentrations were below the LoD. Around 8ppb MACR and 20ppb NO_x were injected at the 13th Nov 2006 experiment, on the 13th of Apr 2007 additionally about 500ppm CO were added as OH scavenger (OH is an product of the ozonolysis, which also takes place during nighttime chemistry). After awaiting at least two GC measurements, about 200ppb ozone were introduced. Therewith, following reaction R5.7, NO_3 is formed and the chemical degradation of MACR is started. Before that moment, the decrease is solely caused by the dilution.

5.3.1 Used Models

Once more, the original MCM and an 'IUPAC' model were tested against the chamber experiments. In case of nighttime chemistry, the differences concerning the fate of the MACO3 radical is much more pronounced, as the degradation is supposed to proceed via the H-atom abstraction exclusively, thus MACO3 branch. In case of the MCM, the MACO3 radical further reacts with NO3 and forms the PAN precursor radical CH3CO3. No IUPAC recommendation is given for the reaction of MACO3 with NO3, but in analogy to the reactions with NO during daytime, it is supposed that in terms of IUPAC the MACO3 further proceeds via

$$MACO3 + NO_3 \longrightarrow CH_2CCH_3 + CO_2 + NO_2 + O_2$$
 (R5.11)

The PAN precursor CH3CO3 is thus not formed and no PAN is expected in contradiction to the MCM model. The MACR + NO₃ reaction scheme implemented in the 'IUPAC' EASY model is provided in figure 5.10, the changed reactions are separately listed in table 5.3.

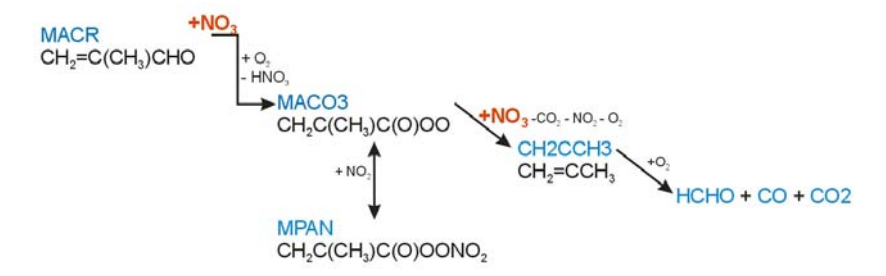


Figure 5.10: NO_3 induced MACR degradation scheme implemented in the 'IUPAC' model.

Except for the dilution, none of the important chamber features of the last subchapters influence the NO_3 chemistry. As the chamber is not illuminated, no photolytic HONO or HCHO is built. The chamber air was not humidified, thus no impurities can be introduced by the water vapor. And as nearly no OH is present, even scavenged by 500ppm CO in the second experiment, the background reactivity is negligible.

5.3.2 Results

Measurement and model run comparisons for both days are provided in figure 5.11. The measured concentrations for MACR (Perkin Elmer GC), NO_x (CL), PAN and MPAN (both GC-ECD), and ozone (CL) are given together with concentrations calculated with the help of the original MCM and the 'IUPAC' mechanism.

The MACR degradation rate measured by the GC is underestimated by both models during the first half of the experiments. The steep measured decrease of the second experiment may also partly be attributed to the assumed problems of the GC measurements with the ozone depletion, which has been already assumed for the ozonolysis experiment of the 12th Apr 2007 presented in the previous section. As no $\rm NO_3$ measurements were available, the modelled MACR concentrations are mainly determined by the modelled $\rm NO_3$ concentration, which is influenced by numerous reactions, and the rate coefficient of the reaction

$$MACR + NO_3 \xrightarrow{O_2} MACO_3 + HNO_3.$$
 (R5.12)

This rate coefficient was studied at least five times, with four studies being in good agreement [149] and thus give a solid basis for a sound recommendation. The MCM model predictions for the NO_3 concentration had been proven to be quite accurate (within $\pm 10\%$ during aldehyde plus NO_3 experiments in the

SAPHIR chamber in the study of Bossmeyer et al. 2006 [86]). Nevertheless, the modelled NO_3 concentration can not be granted to be that accurate. An overestimation towards the end of the experiment may therefore lead to the continuing model MACR degradation which is no more visible in the measurements.

Missing model representations of NO_3 loss processes inside the chamber during the second experiment may also lead to the excessive NO_x estimates compared to the measurements.

What already becomes evident, when looking at the different model reaction schemes of the original MCM and the 'IUPAC' model, namely no PAN in case of 'IUPAC' for the NO₃ degradation path in contrast to a high yield in the MCM, clearly shows up in the model runs. Only minor amounts of PAN are predicted with the help of the 'IUPAC' model for both days. They emerge due to the ozonolysis, which makes up about 10% of the total MACR degradation by the experimental setup with the high ozone concentrations. The PAN measurements are roughly approximated by the 'IUPAC' model. The MCM model, however, highly overestimates the measured PAN yield. The MACO3 radical thus once more seems not to further proceed via the CH3CO3 radical, as was already found for the OH-induced MACR degradation of chapter 5.1, but via the CH2CCH3 radical as recommended by the IUPAC panel.

The MPAN measurements are clearly, up to a factor of four, overestimated by both models. As the measurements proved to be reliable in the experiments described before, the model deviations are attributed to incomplete knowledge and thus incorrect representation in the mechanisms concerning the MPAN nighttime destruction processes or of the production and destruction processes of its precursor radical MACO3. As the MPAN measurements were represented within the measurement error margins for the OH-induced MACR degradation, the building and thermal decomposition of MPAN itself is assumed to be comparatively well represented by the model.

During the kinetic studies cited in the IUPAC recommendation [149], e.g. by $Kwok\ et\ al.\ 1996\ [150]$, $Chew\ et\ al.\ 1998\ [151]$, or $Canosa-Mas\ et\ al.\ 1999\ [152]$, no specific product studies of the MACR + NO₃ reaction have been conducted. Analogy with the H-atom abstraction branch of the OH-induced MACR degradation is assumed up to now. Hence there is room for speculations:

- The initial reaction R5.12 may not only yield MACO3 and HNO₃ but may also result in other products, which are no MPAN precursors any more.
- 2. The rate coefficient for the reaction R5.11 and the corresponding MCM reaction, respectively, may be to small. A 'lumped' rate coefficients for all $\rm RO_2+NO_3$ is used by now.
- MPAN may not only decompose thermally, but could react with NO₃, too.

To distinguish between this different possibilities is infeasible with the given set of experimental data. New experimental set ups have to be considered

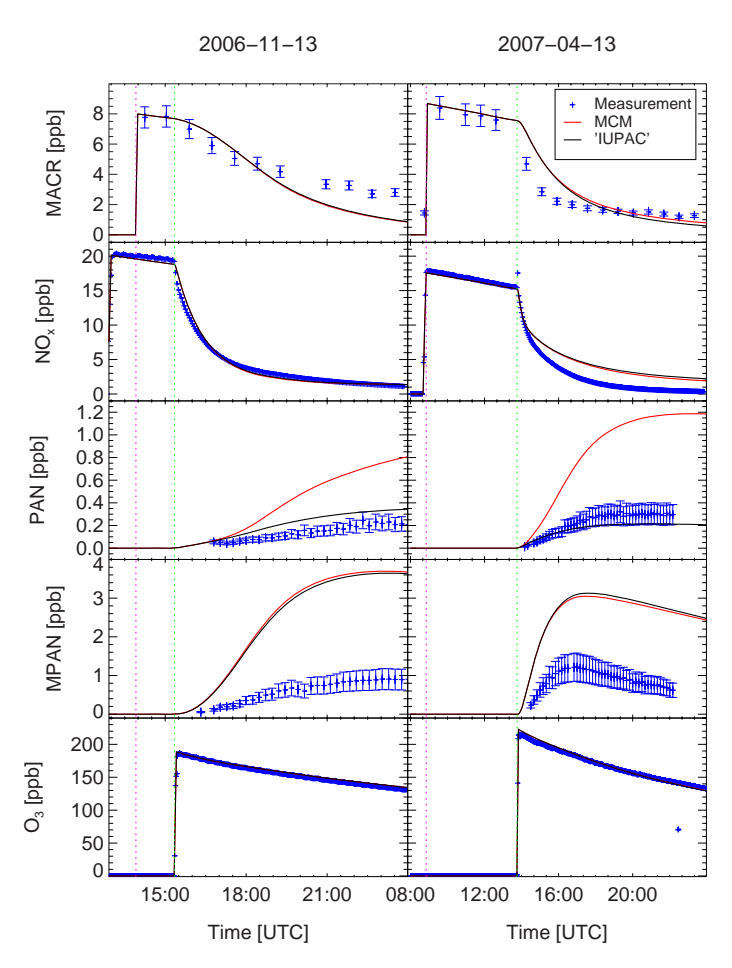


Figure 5.11: Nighttime MACR degradation experiments on 13th Nov 2006 and 13th Apr 2007. From top to the bottom, the measured time profiles of MACR (GC), NO_x (CL), PAN, MPAN (both GC-ECD), and ozone (CL) are shown by blue crosses. At the pink hatched line, MACR was added. NO_x had already been introduced about an hour before during the first (left column) and some minutes before during the second experiment (right column). For the second experiment, about 500ppm CO were injected before the MACR was added. At the times marked with green hatched lines about 200ppb ozone was inserted to start the degradation reaction.

Concentration estimates calculated with the original MCM (red lines) and the 'IUPAC' mechanism (black) are provided for comparison. Except for the PAN concentrations, they proceed nearly uniformly. The MPAN measurements are strongly overestimated by both models.

therefore. For example, when considering the third suggestion, more MPAN could be produced by the OH induced MACR degradation. If the roof is closed at high MPAN concentrations and it is cared for enough ozone and NO_2 for reasonably high NO_3 concentrations, then an elevated MPAN degradation should be quantifiable, if MPAN actually reacts with NO_3 .

5.4 Conclusion

The OH-induced MACR degradation seems to be fairly understood with respect to the IUPAC recommendation. In the MCM, however, a wrong fate for the MACO3, the initial peroxy radical of the H-atom abstraction path, is given. In the preceding sections it has been shown, that contrary to the MCM proposal, no PAN is built during the course of this H-atom abstraction path, neither during the OH nor the photolysis nor the NO₃ induced MACR degradation.

Although the PAN yield of the MCM hence is wrong, astonishingly, no significant deviations of the ozone course could be seen. This can be traced back to the cancelling out of different errors. Indeed, the CH3CO3 as a product of MACO3+NO gives the opportunity to built up PAN and consumes RO₂ and NO₂ at this time. CH3CO3 which does not build PAN, but degrades further, however, yields much more ozone than the CH2CCH3 radical recommended by IUPAC. This can be seen quite simply, when once more looking at the lumped reactions R5.2 and R5.5 and comparing the number of NO₂s and HO₂ formed in each reaction.

The photolysis of MACR was found to be smaller by a factor of ten than given in the (anyway arguable) IUPAC recommendation and in the MCM.

The most important finding, indeed, was the much smaller MPAN concentration measured than expected during nighttime NO_3 chemistry. The yield is far away from being 100% as supposed by Warneke et al. 2004 [30], but hardly reaches 20%. As obviously much less MPAN is produced during NO_3 night-time chemistry than by the OH-induced daytime (photochemical) degradation, MPAN shows to be an even better marker for the biogenic photochemical ozone production, as used by Williams et al. 1997 [55] and Roberts et al. 1998 [56], than expected before, as it is less influenced by nighttime chemical reactions. Additionally, the photochemical MPAN production seems to be sufficiently understood to legitimate the use as a marker.

Table 5.3: Changes in the MCM easy model to represent the IUPAC recommendation for the MACR + OH reaction. The further reactions of the degradation products, e.g. HCHO, MGLYOX or ACETOL, are used as given in the MCM.

														_				_
k[MACO3+NO3->CO2+NO2+CH2CCH3]	k[MACO3+NO3->CH3CO3+HCHO+NO2]		NO_3 chemistry:	k[MACRO->ACETOL+CO+HO2]	k[MACRO->MGLYOX+HCHO+CO+HO2]	$\mid k[MACRO->ACETOL+HCHO+HO2] \mid$	k[CH2CCH3->HCHO+CO+CO2]		k[MACO3+NO->CO2+NO2+CH2CCH3]	k[MACO3+NO->CH3CO3+HCHO+NO2]		k[MACR+OH->MACO3]	H-atom abstraction pathway:			k[MACR+OH->MACRO2]	OH addition pathway:	parameter
	$2.5 \cdot 10^{-12} \cdot 1.6$	MACO3+NO3->CH3CO3+HCHO+NO2				$10^6 sec^{-1}$				$8.70 \cdot 10^{-12} \cdot \exp(290/T) sec^{-1} cm^3$	MACO3+NO->CH3CO3+HCHO+NO2	$1.86 \cdot 10^{-11} \cdot \exp(175/T) \cdot 0.57 sec^{-1} cm^3$			MACRO->ACETOL+HCHO+HO2	$1.86 \cdot 10^{-11} \cdot \exp(175/T) \cdot 0.43 sec^{-1} cm^3$		MCM
$2.5 \cdot 10^{-12} \cdot 1.6$		MACO3+NO3->CH3CO3+HCHO+NO2 MACO3+NO3->CO2+NO2+CH2CCH3		$4.0 \cdot 10^5 sec^{-1}$	$6.0 \cdot 10^5 sec^{-1}$		$10^{-15} \cdot [O2] sec^{-1} cm^3$	CH2CCH3->HCHO+CO+CO2	$8.70 \cdot 10^{-12} \cdot \exp(290/(T))sec^{-1}cm^3$		MACO3+NO->CO2+NO2+CH2CCH3	$8.0 \cdot 10^{-12} \cdot \exp(380./T) \cdot 0.45 sec^{-1} cm^3$		MACRO->ACETOL+CO+HO2	MACRO->MGLYOX+HCHO+CO+HO2	$8.0 \cdot 10^{-12} \cdot \exp(380./T) \cdot 0.55 sec^{-1} cm^3$		'IUPAC'

6 Résumé and Outlook

In a first part of the thesis at hand, different approaches for the prediction of the photochemical O_x production were tested against environmental chamber experiments conducted at the atmosphere simulation chamber SAPHIR, Forschungszentrum Jülich, ICG-2. Gas mixtures of NO_x between 1 and 20ppb, the biogenic emitted VOC isoprene, and its degradation products methacrolein and methyl vinyl ketone with starting values of up to about 13ppb were analyzed.

When testing modelling approaches against chamber data, the chamber features have to be characterized as good as possible. Before starting the $\rm O_x$ production analysis, the dry HCHO chamber source strength, quantified by an empirical formula depending on temperature and $\rm NO_2$ photolysis frequency [109], therefore was analyzed concerning a dependence on the relative humidity of the chamber air. Four standard experiments with variable humidity between June 2004 and Apr 2006 were examined. By standardizing the HCHO source strength by division through a normalized dry chamber source, a remaining humidity dependence could be detected and was quantified. Still undetected dependencies exist, however. The derived, upgraded empirical formula strongly improves the estimation of the HCHO source strength for the use in inverse modelling of photochemical SAPHIR experiments carried out between June 2004 and Apr 2006, when no HCHO measurements are available.

The three O_x prediction approaches tested were fully time dependent MCM model runs, the first degradation step approach, and the τ_{OH} approach. It was the first time, the MCM was tested against environmental chamber experiments at ambient concentrations concerning the O_x production, which showed to be well predicted by the MCM, as measured and modelled net O_x productions did not significantly differ from each other. With this result, it can be reasoned, that comparing the ozone production predicted by the MCM with the one predicted by strongly lumped chemical mechanisms of CTMs can act as a meaningful test for the last mentioned. In contrast to the good O_x performance, the yield of the isoprene degradation product MACR was strongly underestimated by the MCM model, which is a reproduction of the result of Karl et al. 2006 [96].

The first degradation step approach, developed and first time presented in this thesis, is feasible for the estimation of the photochemical O_x production versus physical changes of the O_x concentration during field experiments. An extensive set of measuring instruments is needed for the chemical characterization of the air mass, however, the calculation necessary is quite simple, instead, as no complex numerical solving is needed, but basic arithmetics suffice. Accordingly, by the use of this new approach, the complexity of used models for

the interpretation of field campaigns can strongly be reduced. For the subset of experiments with isoprene as the initial VOC, the FDS approach showed a very high correspondence between measured and calculated O_x progress. The applicability though is restricted to air masses, which have reached a pseudo stationary state of PANs' concentrations. This approximation can be made for in natural conditions with continuous trace gas sources, thus as well during field campaigns, but not during chamber experiments with no refilling of the initial VOC that produced PANs during its degradation.

The third approach tested was entirely new as well and utilizes the fact, that during daytime most VOC degradations are induced by the reaction with OH and proceed via alike degradation steps. The OH concentration [OH] and the OH lifetime $\tau_{\rm OH}$ are therefore identified as good measures for the photochemical O_x production. Simply multiplying [OH] with $\tau_{\rm OH}^{-1}$ and with an integrated factor $F_{\rm OH}$, which has been identified to be 1.27 for isoprene dominated air masses in a NO_x range above about 1ppb, yields a fairly good approximation for the net O_x production rate.

As $\tau_{\rm OH}$ measurements are not yet available at the SAPHIR chamber, the derivation and testing of the approach was up to now limited to modelled data. Experimental, independent tests need to follow. As the integrated factor showed a dependence on the time the chamber air was illuminated, thus the air masses' age, primarily tests with more realistic chemical aging should be performed. This agings is less pronounced in natural environments, as fresh emissions always regenerate the initial (fresh) VOC, therefore the integrated factor is hoped not to vary much in natural air masses. SAPHIR chamber experiments with continuing injections, at the best reproducing mean diurnal courses of natural biogenic isoprene emissions, would shed light on realistic variances of the integrated factor. Presuming the tests to be passed successfully, the proposed $\tau_{\rm OH}$ approach even further reduces the modelling and especially the experimental effort for the interpretation of the $\rm O_x$ progress during field campaigns, which are needed for the further development and evaluation of CTMs.

In the second part of this thesis, the MACR degradation was looked at in more detail. Especially during medium NO_x range photochemical MACR degradation experiments carried out in the SAPHIR chamber, the measured NO_x progress could not be explained by MCM model runs. This discrepancy could be traced back to a deviation of the MCM from the IUPAC recommendation for the MACR+OH reaction, which strongly influences the yield of the NO_x reservoir peroxyacetylnitrate per MACR degraded. The model runs adapting the IUPAC recommendation yielded about a factor of two less PAN than the MCM model runs and showed convincing correspondence with the measured NO_x, PAN and MPAN concentrations. The photolysis frequency of MACR showed to be overestimated probably by about a factor ten concerning the one proposed by IUPAC and used by the MCM. As this estimate was achieved only indirectly by comparison of modelled and measured O_x progress, more direct MACR photolysis tests may be fruitful to approve the deviation.

The most striking outcome of the MACR degradation studies was the strong

overestimation of the MPAN yield during the NO_3 nighttime chemistry. The deviation could not yet be explained. Further well thought-out experimental studies should therefore be carried out to fill the gaps in knowledge obviously existent concerning the nighttime MPAN production and destruction processes.

By the analysis of the MACR degradation studies at the SAPHIR chamber, the use of MPAN as a marker for the daytime photochemical ozone production driven by biogenic precursor VOCs [55, 56] could be legitimated, as on the one hand, the analysis of the MACR degradation induced by OH, $\rm O_3$ and photolysis showed convincing correspondence between modelled and measured MPAN. Nighttime $\rm NO_3$ induced degradation, on the other hand, figured out to be of much less importance for the MPAN concentration than expected before.

A Used Gas Phase Chemistry Mechanisms

In the following, the gas phase chemistry mechanism based on the MCM [78, 77], which was used as a basis for the model studies of this thesis, are compiled. Functions and constants are given in EASY format, which follows FACSIMILE notation. Signs with a special meaning are:

- ; Begin of a comment lasting till the end of the line.
- %n nth input parameter
- \$ line continuation sign
- @ exponentiating symbol: $a@b := a^b$

A.1 Function Definitions

```
; Function definitions
; FILE: mcmex31.incl /Part 1
;-----
;Constant
CONST=FUNCTION[%1]
; Number density of air molecules
; (%1 = pressure [hPa], %2 = temperature [K]
DENSITY=FUNCTION[%1/(%2*1.379E-19)]
; Photolysis frequency, SZA = solar zenith angle
PHTFKT=FUNCTION[(%1*((COS(AMIN(SZA,89.9)*0.0174533))@(%2))* $
               EXP(%3*1./COS(AMIN(SZA,89.9)*0.0174533)))]
; Complex rate coefficient
; Format: k(k0,ki,F) = k0*k1/(k0+k1)*F
         F(k0,ki,Fc) = Fc^{(1/(1+log10(k0/k1)/N)^2)}
         N(Fc) = log(0.75-1.27*log10(Fc))
; %1 = k0 : low pressure limit, M -> 0
; %2 = ki : high pressure limit, M -> infinity
; %3 = Fc : broadening factor
; -> IUPAC 2001 Guide (Lindemann-Hinshelwood expression)
COMPRC = FUNCTION[%1*%2/(%1+%2)*$
                %3@(1/(1+(LOG10(%1/%2)/$
                ((0.75-1.27*LOG10(%3))))@2))]
```

```
; Relative humidity to water vapor concentration
RH2WVC =FUNCTION[%1/100.*exp(21.36469-5339.66/T)/P*M]

; Water vapor concentration to relative humidity
WVC2RH =FUNCTION[%1*100./(exp(21.36469-5339.66/T)/P*M)]
```

A.2 Default Settings and MCM Constants

```
; Default Settings and MCM Constants
; FILE: mcmex31.incl /Part 2
; DEFAULT settings, normally redefined by read in Input
; Temperature in Kelvin
T =CONST(273.2)
; Pressure in hPa
P =CONST(1013.)
; Solar zenith angle
SZA=CONST(45.)
; light exposure
HV=CONST(1.)
; FINAL Definitions
; Number density of the air molecules
M =DENSITY(P,T)
; Oxygen
02=CONST(0.20946*M)
; Nitrogen
N2=CONST(0.78084*M)
KFPAN
       = COMPRC(2.70D-28*(T/300)@-7.1*M, 1.20D-11*(T/300)@-0.9, 0.3)
KBPAN
       = COMPRC(4.90D-03*EXP(-12100/T)*M, 5.40D+16*EXP(-13830/T), 0.3)
KMT01
        = COMPRC(1.00D-31*N2*(T/300)@-1.6, 3.00D-11*(T/300)@0.3, 0.85)
KMT02
       = COMPRC(1.30D-31*N2*(T/300)@-1.5, 2.30D-11*(T/200)@0.24, 0.6)
KMT03
       = COMPRC(3.60D-30*N2*(T/300)@-4.1, 1.90D-12*(T/300)@0.2, 0.35)
       = COMPRC(1.00D-03*N2*(T/300)@-3.5*EXP(-11000/T), $
KMT04
                 9.70D+14*(T/300)@0.1*EXP(-11080/T), 0.35)
KMT05
       = CONST(1+((0.6*M)/(2.652D+19*(300/T))))
       = CONST(1.+1.4D-21*H20*EXP(2200/T))
KMT06
KMT07
        = COMPRC(7.40D-31*N2*(T/300)@-2.4, 3.30D-11*(T/300)@-0.3,$
                 EXP(-T/1420))
KMT08
       = COMPRC(3.30D-30*N2*(T/300)@-3.0, 4.10D-11, 0.4)
```

```
KMT09
        = COMPRC(1.80D-31*N2*(T/300)@-3.2, 4.70D-12, 0.6)
KMT10
        = COMPRC(4.10D-05*N2*EXP(-10650/T), 4.80D+15*EXP(-11170/T), 0.5)
KMT11
        = CONST(2.40D-14*EXP(460/T)+(6.50D-34*EXP(1335/T)*M)/$
               (1+(6.50D-34*EXP(1335/T)*M/2.70D-17*EXP(2199/T))))
KMT13
        = COMPRC(2.50D-30*(T/300)@5.5*M, 7.50D-12, 0.36)
KMT14
        = COMPRC(9.00D-05*EXP(-9690/T)*M, 1.10D+16*EXP(-10560/T), 0.36)
KMT16
        = COMPRC(8.00D-27*(T/300)@-3.5*M, 3.00D-11, 0.5)
KRO2NO3 = CONST(2.50D-12)
KRO2NO = CONST(2.54D-12*EXP(360/T))
KRO2HO2 = CONST(2.91D-13*EXP(1300/T))
KAPHO2 = CONST(4.30D-13*EXP(1040/T))
KAPNO
        = CONST(8.10D-12*EXP(270/T))
KNO3AL = CONST(1.44D-12*EXP(-1862/T))
        = CONST(1.00D+06)
KDEC
KROPRIM = CONST(6.00D-14*EXP(-550/T))
KROSEC = CONST(1.50E-14*EXP(-200/T))
```

A.3 Inorganic Section

The reactions given in this inorganic mechanism were exclusively used for the draw up of figure 2.4. The default settings given above in chapter A.2 were used. Additionally, the initial conditions 1% water vapor concentration and 50ppb ozone were chosen. The model was run for 10,000 seconds and the final values were plotted.

The reaction files anorg.dark.mech and anorg.phot.mech for the anorganic dark and anorganic photolysis reactions, respectively, were skipped, as the used chemical mechanism becomes clear by the corresponding rate files, which are quoted it the following (anorg.dark.rate and anorg.phot.rate), anyway, as the reactions are given in between the squared brackets [].

```
k[0+N02-->N0]=CONST(5.50D-12*EXP(188/(T)))
k[0+N02-->N03]=CONST(KMT02)
k[01D-->0] {SUM}=CONST(1.80D-11*N2*EXP(107/(T))+3.20D-11*02*EXP(67/(T)))
k[NO+O3-->NO2] = CONST(1.40D-12*EXP(-1310/(T)))
k[NO2+O3-->NO3]=CONST(1.40D-13*EXP(-2470/(T)))
k[NO+NO-->NO2+NO2]=CONST(3.30D-39*EXP(530/(T))*02)
k[NO+NO3-->NO2+NO2]=CONST(1.80D-11*EXP(110/(T)))
k[NO2+NO3-->NO+NO2]=CONST(4.50D-14*EXP(-1260/(T)))
k[NO2+NO3-->N2O5]=CONST(KMTO3)
k[N2O5-->NO2+NO3]=CONST(KMTO4)
k[01D-->0H+0H]=CONST(2.20D-10*H20)
k[OH+O3-->HO2]=CONST(1.70D-12*EXP(-940/(T)))
k[OH+H2->HO2]=CONST(7.70D-12*EXP(-2100/(T)))
k[OH+CO-->HO2+CO2] {APPEND_CO2}=CONST(1.30D-13*KMT05)
k[OH+H2O2-->HO2]=CONST(2.90D-12*EXP(-160/(T)))
k[H02+03-->OH] = CONST(2.03D-16*(((T)/300)@4.57*EXP(693/(T))))
k[OH+HO2-->]=CONST(4.80D-11*EXP(250/(T)))
k[H02+H02-->H202]=CONST(2.20D-13*KMT06*EXP(600/(T))+1.90D-33*M*KMT06*EXP(980/(T)))
k[OH+NO-->HONO]=CONST(KMTO7)
k[OH+NO2-->HNO3]=CONST(KMT08)
k[OH+NO3-->HO2+NO2]=CONST(2.20D-11)
k[HO2+NO-->OH+NO2]=CONST(3.60D-12*EXP(270/(T)))
k[H02+N02-->H02N02]=CONST(KMT09)
k[H02N02-->H02+N02] = CONST(KMT10)
k[OH+HO2NO2-->NO2]=CONST(1.90D-12*EXP(270/(T)))
k[H02+N03-->OH+N02]=CONST(4.00D-12)
k[OH+HONO-->NO2]=CONST(2.50D-12*EXP(260/(T))); MCM: CONST(2.50D-12*EXP(-260/(T)))
k[OH+HNO3-->NO3]=CONST(KMT11)
k[0+S02-->S03]=CONST(4.00D-32*EXP(-1000/(T))*N2)
k[OH+SO2-->HSO3]=CONST(KMT12)
k[HSO3-->HO2+SO3]=CONST(1.30D-12*EXP(-330/(T))*O2)
; Anorganic photolysis frequencies
; FILE: anorg.phot.rate
k[03+hv-->01D]=PHTFKT(6.073D-05,1.743,-0.474)
k[03+hv-->0]=PHTFKT(4.775D-04,0.298,-0.080)
k[H2O2+hv-->OH+OH]=PHTFKT(1.041D-05,0.723,-0.279)
k[NO2+hv-->NO+O]=PHTFKT(1.165D-02,0.244,-0.267)
k[NO3+hv-->NO]=PHTFKT(2.485D-02,0.168,-0.108)
k[NO3+hv-->NO2+0]=PHTFKT(1.747D-01,0.155,-0.125)
k[HONO+hv-->OH+NO]=PHTFKT(2.644D-03,0.261,-0.288)
k[HNO3+hv-->OH+NO2]=PHTFKT(9.312D-07,1.230,-0.307)
```

A.4 MCM Isoprene Subset

In the following the MCM isoprene subset is given in EASY nomenclature. The different include files quoted were produced by the conversion tool mcmcv from the downloaded C5H8 subset, called with initial species: C5H8, NO2 and O3, thus, no reactions with sulfur containing species or chlorine are possible. Like for the inorganic part, the reaction file is omitted and just the rate files

is given.

The handling of organic peroxy radicals reacting with each other (reaction R2.28) is treated in a "lumped" way. Instead of giving all possible combinations of partitioning RO₂ radicals, a lumped specie RO2 is introduced, which is equal to the sum of all organic peroxy radicals' concentrations (given in file: ISOPREN.mcm31.ro2.init.inc1). Two reactions are given for each single RO₂ reacting with this lumped specie, as it can act as RO₂ or R'O₂ in reaction R2.28.

```
; MCM Isoprene subset
; FILE: ISOPRENE.init.rate
k[ACETOL+OH-->MGLYOX+HO2]=CONST(3.00D-12)
k[ACETOL+hv-->CH3CO3+HCHO+HO2]=PHTFKT(5.804D-06,1.092,-0.377)
k[ACLOO+CO-->ACETOL]=CONST(1.2D-15)
k[ACLOO+NO-->ACETOL+NO2] = CONST(1.OD-14)
k[ACLOO+NO2-->ACETOL+NO3]=CONST(1.OD-15)
k[ACLOO-->ACETOL+H2O2]=CONST(6.0D-18*H2O)
k[ACLOOA-->ACLOO]=CONST(KDEC*0.11)
k[ACLOOA-->OH+HO2+MGLYOX]=CONST(KDEC*0.89)
k[ACO3+HO2-->ACO2H+O3]=CONST(KAPHO2*0.29)
k[ACO3+HO2-->ACO3H]=CONST(KAPHO2*0.71)
k[ACO3+NO-->HO2+CO+HCHO+NO2]=CONST(KAPNO)
k[ACO3+NO2-->ACRPAN]=CONST(KFPAN)
k[ACO3+NO3-->HO2+CO+HCHO+NO2]=CONST(KRO2NO3*1.60)
k[ACO3-->ACO2H]=CONST(1.00D-11*0.3*RO2)
k[ACO3-->HO2+CO+HCHO]=CONST(1.00D-11*0.7*RO2)
k[ACO3H+hv-->HO2+CO+HCHO+OH]=PHTFKT(7.649D-06,0.682,-0.279)
k[ACR+hv-->ACO3+HO2]=PHTFKT(1.140D-05.0.396.-0.298)
k[ACR+hv-->HCHO+CO+HO2+CO+HO2]=PHTFKT(1.140D-05,0.396,-0.298)
k[ACRPAN-->ACO3+NO2]=CONST(KBPAN)
k[BIACETOH+hv-->CH3CO3+HOCH2CO3]=PHTFKT(3.326D-04,0.148,-0.215)
k[C4PAN10-->H13C02C03+N02]=C0NST(KBPAN)
k[C4PAN6-->CO2H3CO3+NO2]=CONST(KBPAN)
k[C5100-->NOA+GLYOX+HO2]=CONST(KDEC)
k[C51002+H02-->C51000H]=CONST(KR02H02*0.706)
k[C51002+N0-->C5100+N02]=CONST(KR02N0)
k[C51002+N03-->C5100+N02]=CONST(KR02N03)
k[C51002-->C5100]=CONST(9.20D-14*0.7*R02)
k[C51002-->C5100H]=CONST(9.20D-14*0.3*R02)
k[C51000H+hv-->C5100+OH]=PHTFKT(7.649D-06,0.682,-0.279)
k[C570-->MGLYOX+HOCH2CHO+HO2]=CONST(KDEC)
k[C5702+H02-->C5700H]=CONST(KR02H02*0.706)
k[C5702+N0-->C570+N02]=C0NST(KR02N0)
k[C5702+N03-->C570+N02]=C0NST(KR02N03)
k[C5702-->C570]=CONST(9.20D-14*0.7*R02)
k[C5702-->C570H]=CONST(9.20D-14*0.3*R02)
k[C5700H+hv-->C570+OH]=PHTFKT(7.649D-06,0.682,-0.279)
k[C580-->ACETOL+GLYOX+HO2]=CONST(KDEC)
k[C5802+H02-->C5800H]=CONST(KR02H02*0.706)
k[C5802+N0-->C58N03]=C0NST(KR02N0*0.019)
k[C5802+N0-->C580+N02]=CONST(KR02N0*0.981)
k[C5802+N03-->C580+N02]=CONST(KR02N03)
```

```
k[C5802-->C580]=CONST(9.20D-14*0.7*R02)
k[C5802-->C580H]=CONST(9.20D-14*0.3*R02)
k[C5800H+hv-->C580+OH]=PHTFKT(7.649D-06,0.682,-0.279)
k[C590-->ACETOL+HOCH2CO3]=CONST(KDEC)
k[C5902+H02-->C5900H]=CONST(KR02H02*0.706)
k[C5902+N0-->C590+N02]=CONST(KR02N0)
k[C5902+N03-->C590+N02]=CONST(KR02N03)
k[C5902-->C590]=CONST(9.20D-14*R02)
k[C5900H+hv-->C590+OH]=PHTFKT(7.649D-06,0.682,-0.279)
k[C5900H+hv-->HOCH2CO3+ACETOL+OH]=PHTFKT(5.804D-06,1.092,-0.377)
k[C5PAN17-->HC4ACO3+NO2]=CONST(KBPAN)
k[C5PAN18-->NC4C03+NO2]=CONST(KBPAN)
k[C5PAN19-->HC4CCO3+NO2]=CONST(KBPAN)
k[CH200+C0-->HCH0]=CONST(1.20D-15)
k[CH200+N0-->HCH0+N02]=CONST(1.00D-14)
k[CH200+N02-->HCH0+N03]=CONST(1.00D-15)
k[CH200-->HCH0+H202]=CONST(6.00D-18*H20)
k[CH200-->HCOOH]=CONST(1.00D-17*H20)
k[CH200B-->CH200]=CONST(KDEC*0.24) k[CH200B-->C0]=CONST(KDEC*0.40)
k[CH200B-->H02+CO+OH]=CONST(KDEC*0.36)
k[CH200C-->CH200] = CONST(KDEC*0.18)
k[CH200C-->H02+C0+OH]=CONST(KDEC*0.82)
k[CH200E-->CH200]=CONST(KDEC*0.22) k[CH200E-->CO]=CONST(KDEC*0.51)
k[CH200E-->H02+CO+OH]=CONST(KDEC*0.27)
k[CH3CH0+hv-->CH302+H02+C0]=PHTFKT(7.344D-06,1.202,-0.417)
k[CH3CH0HCH0+N03-->CH3CH0HCO3+HNO3]=CONST(KNO3AL*2.4)
k[CH3CHOHCHO+OH-->CH3CHOHCO3]=CONST(2.65D-11)
k[CH3CH0HCH0+hv-->CH3CH0+H02+C0+H02]=PHTFKT(7.914D-05,0.764,-0.364)
k[CH3CH0HCO3+HO2-->IPROPOLPER]=CONST(KAPHO2)
k[CH3CH0HCO3+NO-->CH3CH0+HO2+NO2]=CONST(KAPNO)
k[CH3CH0HCO3+NO2-->IPROPOLPAN]=CONST(KFPAN)
k[CH3CH0HC03+N03-->CH3CH0+H02+N02]=CONST(KR02N03*1.60)
k[CH3CH0HC03-->CH3CH0+H02]=CONST(1.00D-11*R02)
k[CH3CH00+C0-->CH3CH0]=CONST(1.20D-15)
k[CH3CH00+N0-->CH3CH0+N02]=CONST(1.00D-14)
k[CH3CH0O+NO2-->CH3CHO+NO3]=CONST(1.00D-15)
k[CH3CH00-->CH3CH0+H202]=CONST(6.00D-18*H20)
k[CH3CH00-->CH3CO2H]=CONST(1.00D-17*H20)
k[CH3CH00A-->CH3CH00]=CONST(KDEC*0.24)
k[CH3CH00A-->CH302+CO+OH]=CONST(KDEC*0.36)
k[CH3CH00A-->CH302+H02]=CONST(KDEC*0.20)
k[CH3CHOOA-->CH4]=CONST(KDEC*0.20)
k[CH3CO2H+OH-->CH3O2]=CONST(8.00D-13)
k[CH3CO3+HO2-->CH3CO2H+O3]=CONST(KAPHO2*0.29)
k[CH3CO3+HO2-->CH3CO3H]=CONST(KAPHO2*0.71)
k[CH3CO3+NO-->NO2+CH3O2]=CONST(KAPNO)
k[CH3CO3+NO2-->PAN]=CONST(KFPAN)
k[CH3CO3+NO3-->NO2+CH3O2]=CONST(KRO2NO3*1.60)
k[CH3CO3-->CH3CO2H]=CONST(1.00D-11*0.3*RO2)
k[CH3CO3-->CH3O2]=CONST(1.00D-11*0.7*RO2)
k[CH3CO3H+OH-->CH3CO3]=CONST(3.70D-12)
k[CH3CO3H+hv-->CH3O2+OH]=PHTFKT(7.649D-06,0.682,-0.279)
k[CH3COCH2O-->CH3CO3+HCHO]=CONST(KDEC)
k[CH3COCO2H+hv-->CH3CO3+H02]=PHTFKT(1.537D-04,0.170,-0.208)
k[CH3NO3+hv-->CH3O+NO2]=PHTFKT(1.588D-06,1.154,-0.318)
k[CH30-->HCH0+H02]=CONST(7.20D-14*EXP(-1080/(T))*02)
```

```
k[CH302+H02-->CH300H]=CONST(3.80D-13*EXP(780/(T)))
k[CH302+NO-->CH3NO3]=CONST(3.00D-12*EXP(280/(T))*0.001)
k[CH302+NO-->CH30+NO2]=CONST(3.00D-12*EXP(280/(T))*0.999)
k[CH302+N02-->CH302N02]=CONST(KMT13)
k[CH302+N03-->CH30+N02]=CONST(KR02N03*0.40)
k[CH302-->CH30]=CONST(1.82D-13*EXP(416/(T))*0.33*R02)
k[CH302-->CH30H]=CONST(1.82D-13*EXP(416/(T))*0.335*R02)
k[CH302-->HCH0]=CONST(1.82D-13*EXP(416/(T))*0.335*R02)
k[CH302N02-->CH302+N02]=CONST(KMT14)
k[CH30H+OH-->H02+HCH0]=CONST(6.01D-18*(T)@2*EXP(170/(T)))
k[CH300H+hv-->CH30+OH]=PHTFKT(7.649D-06,0.682,-0.279)
k[CHOPRNO3+NO3-->PRNO3CO3+HNO3]=CONST(KNO3AL*2.4)
k[CHOPRNO3+OH-->PRNO3CO3]=CONST(3.55D-12)
k[CHOPRNO3+hv-->HO2+CO+CH3CHO+NO2]=PHTFKT(3.363D-06,1.296,-0.322)
k[CHOPRNO3+hv-->PROPALO+NO2]=PHTFKT(7.549D-06,1.015,-0.324)
k[CO23C3CHO+hv-->CH3CO3+CO+CO+HO2]=PHTFKT(1.537D-04,0.170,-0.208)
k[CO23C3CHO+hv-->CH3CO3+HCOCO3]=PHTFKT(3.326D-04,0.148,-0.215)
k[CO2H3CHO+hv-->MGLYOX+CO+HO2+HO2]=PHTFKT(2.792D-05,0.805,-0.338)
k[CO2H3CO3+HO2-->CO2H3CO3H]=CONST(KAPHO2)
k[CO2H3CO3+NO-->MGLYOX+HO2+NO2]=CONST(KAPNO)
k[CO2H3CO3+NO2-->C4PAN6]=CONST(KFPAN)
k[CO2H3CO3+NO3-->MGLYOX+HO2+NO2]=CONST(KRO2NO3*1.60)
k[CO2H3CO3-->MGLYOX+HO2]=CONST(1.00D-11*RO2)
k[CO2H3CO3H+hv-->CH3CO3+HO2+HCOCO3H]=PHTFKT(5.804D-06,1.092,-0.377)
k[CO2H3CO3H+hv-->MGLYOX+HO2+OH]=PHTFKT(7.649D-06,0.682,-0.279)
k[GA00+C0-->HOCH2CH0]=CONST(1.2D-15)
k[GAOO+NO-->HOCH2CHO+NO2] = CONST(1.0D-14)
k[GAOO+NO2-->HOCH2CHO+NO3]=CONST(1.0D-15)
k[GA00-->HOCH2CH0+H2O2]=CONST(6.0D-18*H2O)
k[GA00-->HOCH2CO2H]=CONST(1.0D-17*H20)
k[GAOOB-->GAOO]=CONST(KDEC*0.11)
k[GAOOB-->OH+HO2+CO+HCHO]=CONST(KDEC*0.89)
k[GLYOO+CO-->GLYOX]=CONST(1.2D-15)
k[GLYOO+NO-->GLYOX+NO2]=CONST(1.OD-14)
k[GLYOO+NO2-->GLYOX+NO3]=CONST(1.OD-15)
k[GLY00-->GLY0X+H202]=CONST(6.0D-18*H20)
k[GLYOO-->HCOCO2H]=CONST(1.OD-17*H2O)
k[GLYOOB-->GLYOO]=CONST(KDEC*0.24)
k[GLYOOB-->HCHO]=CONST(KDEC*0.20)
k[GLY00B-->H02+H02+C0]=CONST(KDEC*0.20)
k[GLY00B-->0H+C0+C0+H02]=CONST(KDEC*0.36)
k[GLYOOC-->GLYOO] = CONST(KDEC*0.11)
k[GLYOOC-->OH+HO2+CO+CO]=CONST(KDEC*0.89)
k[GLYOX+hv-->CO+CO+H2]=PHTFKT(6.845D-05,0.130,-0.201)
k[GLYOX+hv-->CO+CO+HO2+HO2]=PHTFKT(3.802D-05,0.644,-0.312)
k[GLYOX+hv-->HCHO+CO]=PHTFKT(1.032D-05,0.130,-0.201)
k[GLYPAN-->HCOCO3+NO2]=CONST(KBPAN)
k[H13CO2CHO+hv-->HOCH2CHO+CO+HO2+HO2] = PHTFKT(2.792D-05,0.805,-0.338)
k[H13C02C03+H02-->H13C02C03H]=CONST(KAPH02)
k[H13CO2CO3+NO-->HOCH2COCHO+HO2+NO2]=CONST(KAPNO)
k[H13CO2CO3+NO2-->C4PAN10]=CONST(KFPAN)
k[H13CO2CO3+NO3-->HOCH2COCH0+HO2+NO2]=CONST(KRO2NO3*1.60)
k[H13C02C03-->H0CH2C0CH0+H02]=C0NST(1.00D-11*R02)
k[H13CO2CO3H+hv-->HOCH2COCHO+HO2+OH]=PHTFKT(7.649D-06,0.682,-0.279)
k[H14C023C4+OH-->H1C023CHO+H02]=CONST(4.44D-12)
k[H14CO23C4+hv-->HOCH2CO3+HOCH2CO3]=PHTFKT(3.326D-04,0.148,-0.215)
```

```
k[H1CO23CHO+OH-->CO+CO+HOCH2CO3]=CONST(1.44D-11)
k[H1CO23CHO+hv-->CO+CO+HOCH2CO3+HO2]=PHTFKT(1.537D-04,0.170,-0.208)
k[H1CO23CHO+hv-->CO+CO+HOCH2CO3+HO2]=PHTFKT(3.326D-04,0.148,-0.215)
k[H2O2+hv-->OH+OH]=PHTFKT(1.041D-05,0.723,-0.279)
k[HC4ACHO+hv-->ACETOL+HO2+HO2+CO+CO]=PHTFKT(1.140D-05,0.396,-0.298)
k[HC4ACH0+hv-->HC4ACO3+HO2]=PHTFKT(1.140D-05,0.396,-0.298)
k[HC4ACO3+HO2-->HC4ACO2H+O3]=CONST(KAPHO2*0.29)
k[HC4ACO3+HO2-->HC4ACO3H]=CONST(KAPHO2*0.71)
k[HC4ACO3+NO-->ACETOL+CO+HO2+NO2]=CONST(KAPNO)
k[HC4ACO3+NO2-->C5PAN17]=CONST(KFPAN)
k[HC4ACO3+NO3-->ACETOL+C0+HO2+NO2] = CONST(KRO2NO3*1.60)
k[HC4ACO3-->ACETOL+HO2+CO]=CONST(1.00D-11*0.7*RO2)
k[HC4ACO3-->HC4ACO2H] = CONST(1.00D-11*0.3*RO2)
k[HC4ACO3H+hv-->ACETOL+CO+HO2+OH]=PHTFKT(7.649D-06,0.682,-0.279)
k[HC4CCH0+hv-->CH3CO3+HO2+CO+HOCH2CH0]=PHTFKT(1.140D-05,0.396,-0.298)
k[HC4CCHO+hv-->HC4CCO3+HO2]=PHTFKT(1.140D-05,0.396,-0.298)
k[HC4CCO3+HO2-->HC4CCO2H+O3]=CONST(KAPHO2*0.29)
k[HC4CC03+H02-->HC4CC03H]=CONST(KAPH02*0.71)
k[HC4CCO3+NO-->CH3CO3+HOCH2CHO+NO2]=CONST(KAPNO)
k[HC4CCO3+NO2-->C5PAN19]=CONST(KFPAN)
k[HC4CCO3+NO3-->CH3CO3+HOCH2CHO+NO2]=CONST(KRO2NO3*1.60)
k[HC4CCO3-->CH3CO3+HOCH2CHO]=CONST(1.00D-11*0.7*RO2)
k[HC4CC03-->HC4CC02H] = CONST(1.00D-11*0.3*R02)
k[HC4CCO3H+hv-->HOCH2CHO+CH3CO3+OH]=PHTFKT(7.649D-06,0.682,-0.279)
k[HCHO+hv-->CO+HO2+HO2]=PHTFKT(4.642D-05,0.762,-0.353)
k[HCHO+hv-->H2+CO]=PHTFKT(6.853D-05,0.477,-0.323)
k[HCOC5+hv-->CH3CO3+HCHO+HOCH2CO3]=PHTFKT(1.836D-05,0.395,-0.296)
k[HCOCO2H+hv-->HO2+HO2+CO]=PHTFKT(1.537D-04,0.170,-0.208)
k[HCOCO3+HO2-->HCOCO2H+O3]=CONST(KAPHO2*0.29)
k[HCOCO3+HO2-->HCOCO3H]=CONST(KAPHO2*0.71)
k[HCOCO3+NO-->HO2+CO+NO2]=CONST(KAPNO)
k[HCOCO3+NO2-->GLYPAN]=CONST(KFPAN)
k[HCOCO3+NO3-->HO2+CO+NO2]=CONST(KRO2NO3*1.60)
k[HCOCO3-->CO+HO2]=CONST(1.00D-11*0.7*RO2)
k[HCOCO3-->HCOCO2H]=CONST(1.00D-11*0.3*RO2)
k[HCOCO3H+hv-->HO2+CO+OH]=PHTFKT(7.649D-06,0.682,-0.279)
k[HCOCO3H+hv-->HO2+CO+OH]=PHTFKT(2.792D-05,0.805,-0.338)
k[HCOOH+OH-->HO2]=CONST(4.50D-13)
k[HMGLOO+CO-->HOCH2COCHO] = CONST(1.20D-15)
\verb|k[HMGLOO+NO-->HOCH2COCHO+NO2] = CONST(1.00D-14)
k[HMGLOO+NO2-->HOCH2COCHO+NO3]=CONST(1.00D-15)
k[HMGLOO-->HOCH2COCHO+H2O2]=CONST(6.00D-18*H2O)
k[HMGLO0-->HOCH2COCO2H] = CONST(1.00D-17*H20)
k[HMGLOOA-->HMGLOO]=CONST(KDEC*0.24)
k[HMGLOOA-->HOCH2CHO]=CONST(KDEC*0.20)
k[HMGLOOA-->HOCH2CO3+HO2]=CONST(KDEC*0.20)
k[HMGLOOA-->OH+CO+HOCH2CO3]=CONST(KDEC*0.36)
k[HMVKAO-->MGLYOX+HCHO+HO2]=CONST(KDEC)
k[HMVKAO2+HO2-->HMVKAOOH] = CONST(KRO2HO2*0.625)
k[HMVKAO2+NO-->HMVKANO3]=CONST(KRO2NO*0.017)
k[HMVKAO2+NO-->HMVKAO+NO2]=CONST(KRO2NO*0.983)
k[HMVKAO2+NO3-->HMVKAO+NO2]=CONST(KRO2NO3)
k[HMVKAO2-->CO2H3CHO]=CONST(2.00D-12*0.2*RO2)
k[HMVKAO2-->HMVKAO]=CONST(2.00D-12*0.6*RO2)
k[HMVKAO2-->HO12CO3C4]=CONST(2.00D-12*0.2*RO2)
k[HMVKAOOH+hv-->HMVKAO+OH]=PHTFKT(7.649D-06,0.682,-0.279)
```

```
k[HMVKBO-->CH3CO3+HOCH2CHO]=CONST(KDEC)
k[HMVKB02+H02-->HMVKB00H]=CONST(KR02H02*0.625)
k[HMVKB02+N0-->HMVKB0+N02]=CONST(KR02N0)
k[HMVKBO2+NO3-->HMVKBO+NO2]=CONST(KRO2NO3)
k[HMVKB02-->BIACETOH]=CONST(8.80D-13*0.2*R02)
k[HMVKBO2-->HMVKBO]=CONST(8.80D-13*0.6*RO2)
k[HMVKB02-->H012C03C4]=CONST(8.80D-13*0.2*R02)
k[HMVKBOOH+hv-->HMVKBO+OH]=PHTFKT(7.649D-06.0.682.-0.279)
k[HNO3+hv-->OH+NO2]=PHTFKT(9.312D-07,1.230,-0.307)
k[H012C03C4+hv-->CH3C03+H0CH2CH0+H02]=PHTFKT(5.804D-06,1.092,-0.377)
\verb|k[HO2+HO2-->H2O2]| = CONST(2.20D-13*KMT06*EXP(600/(T))+1.90D-33*M*KMT06*EXP(980/(T)))|
k[HO2+NO-->OH+NO2]=CONST(3.60D-12*EXP(270/(T)))
k[H02+N02-->H02N02]=CONST(KMT09)
k[HO2+NO3-->OH+NO2]=CONST(4.00D-12)
k[HO2+O3-->OH]=CONST(2.03D-16*(((T)/300)@4.57*EXP(693/(T))))
k[H02N02-->H02+N02]=C0NST(KMT10)
k[HOCH2CH0+NO3-->HOCH2CO3+HNO3]=CONST(KNO3AL)
k[HOCH2CH0+OH-->GLYOX+HO2]=CONST(1.00D-11*0.200)
k[HOCH2CH0+OH-->HOCH2CO3]=CONST(1.00D-11*0.800)
k[HOCH2CHO+hv-->HO2+HCHO+HO2+CO]=PHTFKT(2.792D-05,0.805,-0.338)
k[HOCH2CO2H+OH-->HCHO+HO2]=CONST(2.73D-12)
k[HOCH2CO3+HO2-->HOCH2CO2H+O3]=CONST(KAPHO2*0.29)
k[HOCH2CO3+HO2-->HOCH2CO3H]=CONST(KAPHO2*0.71)
k[HOCH2CO3+NO-->NO2+HO2+HCHO]=CONST(KAPNO)
k[HOCH2CO3+NO2-->PHAN]=CONST(KFPAN)
k[HOCH2CO3+NO3-->NO2+HO2+HCHO]=CONST(KRO2NO3*1.60)
k[HOCH2CO3-->HCH0+HO2]=CONST(1.00D-11*0.7*RO2)
k[HOCH2CO3-->HOCH2CO2H]=CONST(1.00D-11*0.3*RO2)
k[HOCH2CO3H+OH-->HOCH2CO3]=CONST(6.19D-12)
k[HOCH2CO3H+hv-->HCHO+HO2+OH]=PHTFKT(7.649D-06,0.682,-0.279)
k[HOCH2COCH0+hv-->HOCH2CO3+CO+HO2]=PHTFKT(1.537D-04,0.170,-0.208)
k[HOCH2COCO2H+OH-->HOCH2CO3]=CONST(2.89D-12)
k[HOCH2COCO2H+hv-->HOCH2CO3+HO2]=PHTFKT(1.537D-04,0.170,-0.208)
k[HONO+hv-->OH+NO]=PHTFKT(2.644D-03,0.261,-0.288)
k[HYPROPO-->CH3CHO+HCHO+HO2]=CONST(2.00D+14*EXP(-6410/(T)))
k[HYPROPO2+HO2-->HYPROPO2H]=CONST(KRO2HO2*0.520)
k[HYPROPO2+NO3-->HYPROPO+NO2]=CONST(KRO2NO3)
k[HYPROPO2-->ACETOL]=CONST(8.80D-13*0.2*RO2)
k[HYPROPO2-->HYPROPO]=CONST(8.80D-13*0.6*RO2)
k[HYPROPO2-->PROPGLY]=CONST(8.80D-13*0.2*R02)
k[HYPROPO2H+OH-->ACETOL+OH]=CONST(2.44D-11)
k[HYPROPO2H+OH-->HYPROPO2]=CONST(1.90D-12*EXP(190/(T)))
k[HYPROPO2H+hv-->HYPROPO+OH]=PHTFKT(7.649D-06,0.682,-0.279)
\verb|k[IPROPOLO-->CH3CHO+HCHO+HO2] = CONST(2.00D+14*EXP(-5505/(T)))|
k[IPROPOLO2+HO2-->IPROPOLO2H]=CONST(KRO2HO2*0.520)
k[IPROPOLO2+NO-->IPROPOLO+NO2]=CONST(KRO2NO*0.991)
k[IPROPOLO2+NO-->PROLNO3]=CONST(KRO2NO*0.009)
k[IPROPOLO2+NO3-->IPROPOLO+NO2]=CONST(KRO2NO3)
k[IPROPOLO2-->CH3CHOHCHO]=CONST(2.00D-12*0.2*RO2)
k[IPROPOLO2-->IPROPOLO]=CONST(2.00D-12*0.6*RO2)
k[IPROPOLO2-->PROPGLY]=CONST(2.00D-12*0.2*RO2)
k[IPROPOLO2H+OH-->CH3CHOHCHO+OH]=CONST(1.83D-11)
k[IPROPOLO2H+OH-->IPROPOLO2]=CONST(1.90D-12*EXP(190/(T)))
k[IPROPOLO2H+hv-->IPROPOLO+OH]=PHTFKT(7.649D-06,0.682,-0.279)
k[IPROPOLPAN+OH-->CH3CHO+CO+NO2]=CONST(2.34D-12)
k[IPROPOLPAN-->CH3CH0HCO3+NO2]=CONST(KBPAN)
```

```
k[IPROPOLPER+OH-->CH3CHOHCO3]=CONST(9.34D-12)
k[IPROPOLPER+hv-->CH3CH0+H02+OH]=PHTFKT(7.649D-06,0.682,-0.279)
k[ISOPANO3+hv-->ISOPAO+NO2]=PHTFKT(2.485D-06,1.196,-0.328)
k[ISOPAO-->HC4CCHO+HO2]=CONST(8.4D+10*EXP(-3523/(T)))
k[ISOPAO2+HO2-->ISOPAOOH]=CONST(KRO2HO2*0.706)
k[ISOPAO2+NO-->ISOPANO3]=CONST(KRO2NO*0.108)
k[ISOPA02+N0-->ISOPA0+N02]=CONST(KR02N0*0.892)
k[ISOPAO2+NO3-->ISOPAO+NO2]=CONST(KRO2NO3)
k[ISOPAO2-->HC4ACHO] = CONST(2.40D-12*0.1*RO2)
k[ISOPA02-->ISOPA0]=CONST(2.40D-12*0.8*R02)
k[ISOPAO2-->ISOPAOH]=CONST(2.40D-12*0.1*RO2)
k[ISOPAOOH+hv-->ISOPAO+OH]=PHTFKT(7.649D-06,0.682,-0.279)
k[ISOPBNO3+hv-->ISOPBO+NO2]=PHTFKT(1.135D-05,0.974,-0.309)
k[ISOPBO-->MVK+HCHO+HO2]=CONST(KDEC*0.75)
k[ISOPBO-->MVKOH+CH302]=CONST(KDEC*0.25)
k[ISOPBO2+HO2-->ISOPBOOH]=CONST(KRO2HO2*0.706)
k[ISOPBO2+NO-->ISOPBNO3]=CONST(KRO2NO*0.072)
k[ISOPBO2+NO-->ISOPBO+NO2]=CONST(KRO2NO*0.928)
k[ISOPBO2+NO3-->ISOPBO+NO2]=CONST(KRO2NO3)
k[ISOPBO2-->ISOPBO]=CONST(8.00D-13*0.8*RO2)
k[ISOPBO2-->ISOPBOH]=CONST(8.00D-13*0.2*RO2)
k[ISOPBOOH+hv-->ISOPBO+OH]=PHTFKT(7.649D-06,0.682,-0.279)
k[ISOPCNO3+hv-->ISOPCO+NO2]=PHTFKT(2.485D-06,1.196,-0.328)
k[ISOPCO-->HC4ACHO+HO2]=CONST(8.4D+10*EXP(-3523/(T)))
k[ISOPCO2+HO2-->ISOPCOOH]=CONST(KRO2HO2*0.706)
k[ISOPCO2+NO-->ISOPCNO3]=CONST(KRO2NO*0.108)
k[ISOPCO2+NO-->ISOPCO+NO2]=CONST(KRO2NO*0.892)
k[ISOPCO2+NO3-->ISOPCO+NO2]=CONST(KRO2NO3)
k[ISOPCO2-->HC4CCHO]=CONST(2.00D-12*0.1*RO2)
k[ISOPCO2-->ISOPAOH]=CONST(2.00D-12*0.1*R02)
k[ISOPCO2-->ISOPCO]=CONST(2.00D-12*0.8*RO2)
k[ISOPCOOH+hv-->ISOPCO+OH]=PHTFKT(7.649D-06,0.682,-0.279)
k[ISOPDNO3+hv-->ISOPDO+NO2]=PHTFKT(4.095D-06,1.111,-0.316)
k[ISOPDO-->MACR+HCHO+HO2]=CONST(KDEC)
k[ISOPD02+H02-->ISOPD00H]=CONST(KR02H02*0.706)
k[ISOPDO2+NO-->ISOPDNO3]=CONST(KRO2NO*0.145)
k[ISOPDO2+NO-->ISOPDO+NO2]=CONST(KRO2NO*0.855)
k[ISOPDO2+NO3-->ISOPDO+NO2]=CONST(KRO2NO3)
k[ISOPD02-->HCOC5]=CONST(2.90D-12*0.1*R02)
k[ISOPD02-->ISOPD0]=CONST(2.90D-12*0.8*R02)
k[ISOPDO2-->ISOPDOH]=CONST(2.90D-12*0.1*RO2)
k[ISOPDOOH+hv-->ISOPDO+OH]=PHTFKT(7.649D-06,0.682,-0.279)
k[MACO3+HO2-->MACO2H+O3]=CONST(KAPHO2*0.29)
k[MACO3+HO2-->MACO3H]=CONST(KAPHO2*0.71)
k[MACO3+NO-->CH3CO3+HCHO+NO2]=CONST(8.70D-12*EXP(290/(T)))
k [MACO3+NO2-->MPAN] =CONST(KFPAN)
k[MACO3+NO3-->CH3CO3+HCHO+NO2]=CONST(KRO2NO3*1.60)
k[MACO3-->CH3CO3+HCH0]=CONST(1.00D-11*0.7*RO2)
k[MACO3-->MACO2H] = CONST(1.00D-11*0.3*RO2)
k[MACO3H+hv-->CH3CO3+HCHO+OH]=PHTFKT(7.649D-06,0.682,-0.279)
k[MACR+hv-->CH3CO3+HCHO+CO+HO2]=PHTFKT(1.140D-05,0.396,-0.298)
k[MACR+hv-->MACO3+HO2]=PHTFKT(1.140D-05,0.396,-0.298)
k [MACRO-->ACETOL+HCHO+HO2] = CONST (KDEC)
k[MACRO2+HO2-->MACROOH] = CONST(KRO2HO2*0.625)
k[MACRO2+NO-->MACRO+NO2]=CONST(KRO2NO)
k [MACRO2+NO3-->MACRO+NO2] = CONST (KRO2NO3)
```

```
k[MACRO2-->MACRO]=CONST(9.20D-14*0.7*RO2)
k[MACRO2-->MACROH]=CONST(9.20D-14*0.3*RO2)
k[MACROH+hv-->ACETOL+CO+HO2+HO2]=PHTFKT(7.914D-05,0.764,-0.364)
k[MACROO+CO-->MACR] = CONST(1.2D-15)
k[MACROO+NO-->MACR+NO2] = CONST(1.0D-14)
k[MACROO+NO2-->MACR+NO3]=CONST(1.0D-15)
k[MACROO-->MACO2H] = CONST(1.0D-17*H20)
k[MACROO-->MACR+H2O2]=CONST(6.0D-18*H2O)
k[MACROOA-->C3H6]=CONST(KDEC*0.255)
k[MACROOA-->CH3CO3+HCHO+HO2]=CONST(KDEC*0.255)
k[MACROOA-->MACROO]=CONST(KDEC*0.22)
k[MACROOA-->OH+CO+CH3CO3+HCHO]=CONST(KDEC*0.27)
k[MACROOH+hv-->ACETOL+CO+HO2+OH]=PHTFKT(7.914D-05,0.764,-0.364)
k[MACROOH+hv-->MACRO+OH]=PHTFKT(7.649D-06,0.682,-0.279)
k[MGLOO+CO-->MGLYOX]=CONST(1.2D-15)
k[MGLOO+NO-->MGLYOX+NO2]=CONST(1.OD-14)
k[MGLOO+NO2-->MGLYOX+NO3]=CONST(1.0D-15)
k[MGLOO-->CH3COCO2H] = CONST(1.0D-17*H20)
k[MGL00-->MGLYOX+H202]=CONST(6.0D-18*H20)
k[MGLOOA-->CH3CH0]=CONST(KDEC*0.20)
k[MGLOOA-->CH3CO3+HCHO+HO2]=CONST(KDEC*0.20)
k[MGLOOA-->MGLOO]=CONST(KDEC*0.24)
k[MGLOOA-->OH+CO+CH3CO3]=CONST(KDEC*0.36)
k[MGLYOO+CO-->MGLYOX]=CONST(1.2D-15)
k[MGLY00+N0-->MGLY0X+N02]=CONST(1.0D-14)
k[MGLYOO+NO2-->MGLYOX+NO3] = CONST(1.OD-15)
k[MGLY00-->MGLY0X+H202]=CONST(6.0D-18*H20)
k[MGLYOOA-->MGLYOO] = CONST(KDEC*0.11)
k[MGLYOOA-->OH+CO+CH3CO3]=CONST(KDEC*0.89)
k[MGLY00B-->MGLY00]=CONST(KDEC*0.18)
k[MGLYOOB-->OH+CO+CH3CO3]=CONST(KDEC*0.82)
k[MGLYOX+hv-->CH3CO3+CO+HO2]=PHTFKT(1.537D-04,0.170,-0.208)
k [MPAN-->MACO3+NO2] = CONST (KBPAN)
k[MVK+hv-->C3H6+C0]=PHTFKT(1.836D-05,0.395,-0.296)
k[MVK+hv-->CH3CO3+HCHO+CO+HO2]=PHTFKT(1.836D-05,0.395,-0.296)
k[MVKO-->HCHO+ACO3]=CONST(KDEC)
k[MVKO2+HO2-->MVKOOH] = CONST(KRO2HO2*0.625)
k[MVKO2+NO-->MVKO+NO2]=CONST(KRO2NO)
k[MVKO2+NO3-->MVKO+NO2]=CONST(KRO2NO3)
k[MVKO2-->MVKO] = CONST(2.00D-12*0.6*RO2)
k[MVKO2-->MVKOH]=CONST(2.00D-12*0.2*RO2)
k[MVKO2-->VGLYOX]=CONST(2.00D-12*0.2*RO2)
k[MVKOH+O3-->HMGLOOA+HCHO]=CONST(7.51D-16*EXP(-1521/(T))*0.5)
k[MVKOH+O3-->HOCH2COCHO+CH2OOB]=CONST(7.51D-16*EXP(-1521/(T))*0.5)
k[MVKOH+OH-->MVKOHAO2]=CONST(4.60D-12*EXP(452/(T))*0.3)
k[MVKOH+OH-->MVKOHBO2] = CONST(4.60D-12*EXP(452/(T))*0.7)
k[MVKOH+hv-->ALLYLOH+CO]=PHTFKT(1.836D-05,0.395,-0.296)
k[MVKOH+hv-->HCHO+HO2+HOCH2CO3+CO]=PHTFKT(1.836D-05,0.395,-0.296)
k[MVKOHANO3+OH-->H13CO2CHO+NO2]=CONST(4.37D-12)
k[MVKOHAO-->HOCH2COCHO+HCHO+HO2]=CONST(KDEC)
k[MVKOHAO2+HO2-->MVKOHAOOH]=CONST(KRO2HO2*0.625)
k[MVKOHAO2+NO-->MVKOHANO3]=CONST(KRO2NO*0.017)
k[MVKOHAO2+NO-->MVKOHAO+NO2]=CONST(KRO2NO*0.983)
k[MVKOHAO2+NO3-->MVKOHAO+NO2]=CONST(KRO2NO3)
k[MVKOHAO2-->H13CO2CHO]=CONST(2.00D-12*RO2*0.2)
k[MVKOHAO2-->MVKOHAO]=CONST(2.00D-12*RO2*0.6)
```

```
k[MVKOHAO2-->MVKOHAOH]=CONST(2.00D-12*RO2*0.2)
k[MVKOHAOH+OH-->H13CO2CHO+H02]=CONST(2.10D-11)
k[MVKOHAOH+hv-->HOCH2CO3+HOCH2CH0+HO2]=PHTFKT(5.804D-06,1.092,-0.377)
k[MVKOHAOOH+OH-->H13CO2CHO+OH] =CONST(5.98D-11)
k[MVKOHAOOH+hv-->MVKOHAO+OH]=PHTFKT(5.804D-06,1.092,-0.377)
k[MVKOHAOOH+hv-->MVKOHAO+OH]=PHTFKT(7.649D-06,0.682,-0.279)
k[MVKOHBO-->HOCH2CHO+HOCH2CO3]=CONST(KDEC)
k[MVKOHBO2+HO2-->MVKOHBOOH]=CONST(KRO2HO2*0.625)
k[MVKOHBO2+NO-->MVKOHBO+NO2]=CONST(KRO2NO)
k[MVKOHBO2+NO3-->MVKOHBO+NO2]=CONST(KRO2NO3)
k[MVKOHB02-->H14C023C4]=CONST(8.80D-13*R02*0.2)
k[MVKOHBO2-->MVKOHAOH]=CONST(8.80D-13*RO2*0.2)
k[MVKOHBO2-->MVKOHBO]=CONST(8.80D-13*RO2*0.6)
k[MVKOHBOOH+OH-->H14CO23C4+OH]=CONST(4.39D-12)
k[MVKOHBOOH+hv-->HOCH2CHO+HOCH2CO3+OH]=PHTFKT(5.804D-06,1.092,-0.377)
k[MVKOHBOOH+hv-->MVKOHBO+OH]=PHTFKT(7.649D-06,0.682,-0.279)
k[MVK00+C0-->MVK]=CONST(1.2D-15)
k[MVKOO+NO-->MVK+NO2] = CONST(1.0D-14)
k[MVKOO+NO2-->MVK+NO3]=CONST(1.0D-15)
k[MVKOO-->MVK+H2O2]=CONST(6.0D-18*H2O)
k[MVKOOA-->C3H6]=CONST(KDEC*0.255)
k[MVKOOA-->CH3O2+HCHO+CO+HO2]=CONST(KDEC*0.255)
k[MVKOOA-->MVKOO]=CONST(KDEC*0.22)
k[MVKOOA-->OH+MVKO2]=CONST(KDEC*0.27)
k[MVKOOH+hv-->HCHO+OH+ACO3]=PHTFKT(1.836D-05,0.395,-0.296)
k[MVKOOH+hv-->MVKO+OH]=PHTFKT(7.649D-06,0.682,-0.279)
k[N205-->N02+N03]=CONST( KMT04 )
k[NC4CHO+hv-->NOA+CO+CO+HO2+HO2]=PHTFKT(1.140D-05,0.396,-0.298)
k[NC4C03+H02-->NC4C02H+03]=CONST(KAPH02*0.29)
k[NC4CO3+HO2-->NC4CO3H]=CONST(KAPHO2*0.71)
k[NC4CO3+NO-->NOA+CO+HO2+NO2] = CONST(KAPNO)
k[NC4CO3+NO2-->C5PAN18]=CONST(KFPAN)
k[NC4CO3+NO3-->NOA+CO+HO2+NO2]=CONST(KRO2NO3*1.60)
k[NC4CO3-->NC4CO2H]=CONST(1.00D-11*0.3*RO2)
k[NC4C03-->NOA+H02+C0]=CONST(1.00D-11*0.7*R02)
k[NC4CO3H+hv-->NOA+CO+HO2+OH]=PHTFKT(7.649D-06,0.682,-0.279)
k[NISOPNO3+hv-->NISOPO+NO2]=PHTFKT(2.485D-06,1.196,-0.328*2.0)
k[NISOPO-->NC4CHO+HO2]=CONST(KROPRIM*O2)
k[NISOPO2+HO2-->NISOPOOH]=CONST(KRO2HO2*0.706)
k[NISOPO2+NO-->NISOPNO3]=CONST(KRO2NO*0.052)
k[NISOPO2+NO-->NISOPO+NO2] = CONST(KRO2NO*0.948)
k[NISOPO2+NO3-->NISOPO+NO2]=CONST(KRO2NO3)
k[NISOPO2-->ISOPCNO3]=CONST(1.30D-12*0.2*RO2)
k[NISOPO2-->NC4CHO]=CONST(1.30D-12*0.2*RO2)
k[NISOPO2-->NISOPO]=CONST(1.30D-12*0.6*RO2)
k[NISOPOOH+hv-->NISOPO+OH]=PHTFKT(7.649D-06,0.682,-0.279)
k[NO+HYPROPO2-->HYPROPO+NO2]=CONST(KRO2NO*0.977)
k[NO+HYPROPO2-->PROPOLNO3]=CONST(KRO2NO*0.023)
k[N0+N0-->N02+N02] = CONST(3.30D-39*EXP(530/(T))*02)
k[NO+NO3-->NO2+NO2]=CONST(1.80D-11*EXP(110/(T)))
k[NO+O3-->NO2]=CONST(1.40D-12*EXP(-1310/(T)))
k[NO2+NO3-->N2O5]=CONST( KMTO3 )
k[NO2+NO3-->NO+NO2]=CONST(4.50D-14*EXP(-1260/(T)))
k[NO2+O3-->NO3]=CONST(1.40D-13*EXP(-2470/(T)))
k[NO2+hv-->NO+0]=PHTFKT(1.165D-02,0.244,-0.267)
k[NO3+ACR-->ACO3+HNO3]=CONST(KNO3AL*1.2)
```

```
k[NO3+C3H6-->PRONO3AO2]=CONST(9.40D-15*0.35)
k[NO3+C3H6-->PRONO3BO2]=CONST(9.40D-15*0.65)
k[NO3+C5H8-->NISOPO2]=CONST(3.03D-12*EXP(-446/(T)))
k[NO3+CH3CH0-->HNO3+CH3CO3]=CONST(KNO3AL)
k[NO3+CO23C3CHO-->CH3CO3+CO+CO+HNO3]=CONST(KNO3AL*4.0)
k[NO3+CO2H3CHO-->CO2H3CO3+HNO3]=CONST(KNO3AL*4.0)
k[NO3+GLYOX-->CO+CO+HO2+HNO3]=CONST(KNO3AL*0.6)
k[NO3+GLYOX-->HCOCO3+HNO3]=CONST(KNO3AL*0.4)
k[NO3+H13CO2CHO-->H13CO2CO3+HNO3]=CONST(KNO3AL*4.0)
k[NO3+HC4ACHO-->HC4ACO3+HNO3]=CONST(KNO3AL*4.25)
k[NO3+HC4CCH0-->HC4CCO3+HNO3]=CONST(KNO3AL*4.25)
k[NO3+HCHO-->HNO3+CO+HO2]=CONST(5.80D-16)
k[NO3+HOCH2COCHO-->HOCH2CO3+CO+HNO3]=CONST(KNO3AL*2.4)
k[NO3+MACR-->MACO3+HNO3]=CONST(KNO3AL*2.0)
k[NO3+MGLYOX-->CH3CO3+CO+HNO3]=CONST(KNO3AL*2.4)
k[NO3+NC4CHO-->NC4CO3+HNO3]=CONST(KNO3AL*4.25)
k[NO3+VGLYOX-->CO+ACO3+HNO3]=CONST(KNO3AL*2.0)
k[NO3+hv-->NO] = PHTFKT(2.485D-02,0.168,-0.108)
k[NO3+hv-->NO2+0]=PHTFKT(1.747D-01,0.155,-0.125)
k[NOA+OH-->MGLYOX+NO2]=CONST(1.30D-13)
k[NOA+hv-->CH3CO3+HCHO+NO2]=PHTFKT(3.363D-06,1.296,-0.322)
k[NOA+hv-->CH3COCH2O+NO2]=PHTFKT(7.549D-06,1.015,-0.324)
k[NOAOO+CO-->NOA] = CONST(1.2D-15)
k[NOAOO+NO-->NOA+NO2]=CONST(1.OD-14)
k[NOAOO+NO2-->NOA+NO3]=CONST(1.OD-15)
k[NOAOO-->NOA+H2O2]=CONST(6.OD-18*H2O)
k[NOAOOA-->NOAOO]=CONST(KDEC*0.11)
k[NOAOOA-->OH+NO2+MGLYOX]=CONST(KDEC*0.89)
k[0+N0-->N02]=CONST(KMT01)
k[0+NO2-->NO]=CONST(5.50D-12*EXP(188/(T)))
k[0+N02-->N03]=CONST(KMT02)
k[0+03--]=CONST(8.00D-12*EXP(-2060/(T)))
 k[0-->03] = \texttt{CONST}(5.60D-34*02*N2*(((T)/300)@-2.6+6.00D-34*02*02*(((T)/300)@-2.6))) 
k[01D-->0] \{SUM\}=CONST(1.80D-11*N2*EXP(107/(T))+3.20D-11*02*EXP(67/(T)))
k[O1D-->OH+OH]=CONST(2.20D-10*H20)
k[O3+ACR-->CH2OOB+GLYOX]=CONST(2.9D-19*0.5)
k[O3+ACR-->GLYOOB+HCHO]=CONST(2.9D-19*0.5)
k[03+C3H6-->CH200B+CH3CH0]=CONST(5.51D-15*EXP(-1878/(T))*0.5)
k[O3+C3H6-->CH3CHOOA+HCHO]=CONST(5.51D-15*EXP(-1878/(T))*0.5)
k[03+C5H8-->CH200E+MACR]=CONST(7.86D-15*EXP(-1913/(T))*0.3)
k[O3+C5H8-->CH2OOE+MVK]=CONST(7.86D-15*EXP(-1913/(T))*0.2)
k[03+C5H8-->HCHO+MACROOA] = CONST(7.86D-15*EXP(-1913/(T))*0.3)
k[O3+C5H8-->HCHO+MVKOOA]=CONST(7.86D-15*EXP(-1913/(T))*0.2)
k[03+HC4ACH0-->ACETOL+GLYOOC]=CONST(2.40D-17*0.5)
k[O3+HC4ACHO-->ACLOOA+GLYOX]=CONST(2.40D-17*0.5)
k[O3+HC4CCHO-->MGLYOOA+HOCH2CHO]=CONST(2.40D-17*0.5)
k[O3+HC4CCHO-->MGLYOX+GAOOB]=CONST(2.40D-17*0.5)
k[O3+MACR-->CH2OOC+MGLYOX]=CONST(1.36D-15*EXP(-2112/(T))*0.5)
k[O3+MACR-->HCHO+MGLYOOB]=CONST(1.36D-15*EXP(-2112/(T))*0.5)
k[03+MVK-->MGLOOA+HCHO] = CONST(7.51D-16*EXP(-1521/(T))*0.5)
k[O3+MVK-->MGLYOX+CH2OOB]=CONST(7.51D-16*EXP(-1521/(T))*0.5)
k[03+NC4CH0-->NOA+GLYOOC]=CONST(2.40D-17*0.5)
k[O3+NC4CHO-->NOAOOA+GLYOX]=CONST(2.40D-17*0.5)
k[03+hv-->0] = PHTFKT(4.775D-04,0.298,-0.080)
k[03+hv-->01D] = PHTFKT(6.073D-05,1.743,-0.474)
k[OH+ACO2H-->HO2+CO+HCHO]=CONST(8.66D-12)
```

```
k[OH+ACO3H-->ACO3]=CONST(1.22D-11)
k[OH+ACR-->ACO3]=CONST(1.99D-11)
k[OH+ACRPAN-->HOCH2CHO+CO+NO2]=CONST(8.63D-12)
k[OH+ALLYLOH-->ACR+HO2]=CONST(2.59D-11)
k[OH+BIACETOH-->CO23C3CHO+HO2]=CONST(2.69D-12)
k[OH+C3H6-->HYPROPO2]=CONST(KMT16*0.87)
k[OH+C3H6-->IPROPOLO2]=CONST(KMT16*0.13)
k[OH+C4PAN10-->HOCH2COCH0+C0+NO2]=CONST(5.83D-12)
k[OH+C4PAN6-->MGLYOX+CO+NO2]=CONST(3.74D-12)
k[OH+C510OH-->C5100]=CONST(2.69D-11)
k[OH+C51000H-->C51002]=CONST(2.81D-11)
k[OH+C570H-->C570]=CONST(3.04D-11)
k[OH+C5700H-->C5702]=CONST(3.16D-11)
k[OH+C58NO3-->ACETOL+GLYOX+HO2+NO2]=CONST(2.32D-11)
k[OH+C580H-->C580]=CONST(3.04D-11)
k[OH+C5800H-->C5802]=CONST(3.16D-11)
k[OH+C5900H-->C5902]=CONST(9.70D-12)
k[OH+C5H8-->ISOPA02]=CONST(2.54D-11*EXP(410/(T))*0.164)
k[OH+C5H8-->ISOPBO2]=CONST(2.54D-11*EXP(410/(T))*0.491)
k[OH+C5H8-->ISOPCO2]=CONST(2.54D-11*EXP(410/(T))*0.086)
k[OH+C5H8-->ISOPDO2]=CONST(2.54D-11*EXP(410/(T))*0.259)
k[OH+C5PAN17-->MACROH+CO+NO2]=CONST(2.52D-11)
k[OH+C5PAN18-->NOA+C0+C0+NO2]=CONST(2.16D-11)
k[OH+C5PAN19-->H012C03C4+C0+N02]=CONST(2.52D-11)
k[OH+CH3CHO-->CH3CO3]=CONST(5.55D-12*EXP(311/(T)))
k[OH+CH3COCO2H-->CH3CO3]=CONST(8.0D-13)
k[OH+CH3NO3-->HCHO+NO2]=CONST(1.00D-14*EXP(1060/(T)))
k[OH+CH30OH-->CH302]=CONST(1.90D-12*EXP(190/(T)))
k[OH+CH3OOH-->HCHO+OH]=CONST(1.00D-12*EXP(190/(T)))
k[OH+CH4-->CH3O2]=CONST(9.65D-20*(T)@2.58*EXP(-1082/(T)))
k[OH+CO-->HO2+CO2] {APPEND_CO2}=CONST(1.30D-13*KMT05)
k[OH+CO23C3CHO-->CH3CO3+CO+CO]=CONST(1.23D-11)
k[OH+CO2H3CHO-->CO2H3CO3]=CONST(2.45D-11)
k[OH+CO2H3CO3H-->CO2H3CO3]=CONST(7.34D-12)
k[OH+GLYOX-->CO+CO+HO2]=CONST(1.14D-11*0.6)
k[OH+GLYOX-->HCOCO3]=CONST(1.14D-11*0.4)
k[OH+GLYPAN-->CO+CO+NO2]=CONST(1.22D-11)
k[OH+H13CO2CHO-->H13CO2CO3]=CONST(2.66D-11)
k[OH+H13CO2CO3H-->H13CO2CO3]=CONST(9.43D-12)
k[OH+H2-->HO2]=CONST(7.70D-12*EXP(-2100/(T)))
k[OH+H2O2-->HO2]=CONST(2.90D-12*EXP(-160/(T)))
k[OH+HC4ACHO-->C5802]=CONST(4.52D-11*0.52)
k[OH+HC4ACHO-->HC4ACO3]=CONST(4.52D-11*0.48)
k[OH+HC4ACO2H-->ACETOL+CO+HO2]=CONST(2.52D-11)
k[OH+HC4ACO3H-->HC4ACO3]=CONST(2.88D-11)
k[OH+HC4CCHO-->C5702]=CONST(4.52D-11*0.52)
k[OH+HC4CCH0-->HC4CCO3]=CONST(4.52D-11*0.48)
k[OH+HC4CCO2H-->CH3CO3+HOCH2CHO]=CONST(2.52D-11)
k[OH+HC4CCO3H-->HC4CCO3]=CONST(2.88D-11)
k[OH+HCHO-->HO2+CO]=CONST(1.20D-14*(T)*EXP(287/(T)))
k[OH+HCOC5-->C5902]=CONST(3.81D-11)
k[OH+HCOCO2H-->CO+HO2]=CONST(1.23D-11)
k[OH+HCOCO3H-->HCOCO3]=CONST(1.58D-11)
k[OH+HMVKANO3-->CO2H3CHO+NO2]=CONST(2.23D-12)
k[OH+HMVKAOOH-->CO2H3CHO+OH]=CONST(5.77D-11)
k[OH+HMVKBOOH-->BIACETOH+OH]=CONST(3.95D-11)
```

```
k[OH+HN03-->N03]=CONST(KMT11)
k[OH+H012C03C4-->BIACETOH+H02]=CONST(1.88D-11)
k[OH+HO2-->]=CONST(4.80D-11*EXP(250/(T)))
k[OH+HO2NO2-->NO2]=CONST(1.90D-12*EXP(270/(T)))
k[OH+HOCH2COCHO-->HOCH2CO3+CO]=CONST(1.44D-11)
k[OH+HONO-->NO2]=CONST(2.50D-12*EXP(260/(T)))
k[OH+ISOPANO3-->HC4ACHO+NO2]=CONST(8.91D-11)
k[OH+ISOPAOH-->HC4ACHO+HO2]=CONST(9.30D-11*0.5)
k[OH+ISOPAOH-->HC4CCHO+HO2]=CONST(9.30D-11*0.5)
k[OH+ISOPAOOH-->HC4ACHO+OH]=CONST(1.07D-10)
k[OH+ISOPBNO3-->MVK+HCHO+NO2]=CONST(3.55D-11)
k[OH+ISOPBOH-->ISOPBO]=CONST(3.85D-11)
k[OH+ISOPBOOH-->ISOPBO2]=CONST(4.20D-11)
k[OH+ISOPCNO3-->HC4CCHO+NO2]=CONST(8.91D-11)
k[OH+ISOPCOOH-->HC4CCHO+OH]=CONST(1.07D-10)
k[OH+ISOPDNO3-->HCOC5+NO2]=CONST(6.10D-11)
k[OH+ISOPDOH-->HCOC5+HO2]=CONST(7.38D-11)
k[OH+ISOPDOOH-->HCOC5+OH]=CONST(1.07D-10)
k[OH+MACO2H-->CH3CO3+HCHO]=CONST(1.51D-11)
k[OH+MACO3H-->MACO3]=CONST(1.87D-11)
k[OH+MACR-->MACO3]=CONST(1.86D-11*EXP(175/(T))*0.57)
k[OH+MACR-->MACRO2]=CONST(1.86D-11*EXP(175/(T))*0.43)
k[OH+MACROH-->MACRO]=CONST(2.46D-11)
k[OH+MACROOH-->MACRO2]=CONST(2.82D-11)
k[OH+MGLYOX-->CH3CO3+CO]=CONST(1.72D-11)
k[OH+MPAN-->ACETOL+CO+NO2]=CONST(3.60D-12)
k[OH+MVK-->HMVKAO2]=CONST(4.13D-12*EXP(452/(T))*0.3)
k[OH+MVK-->HMVKBO2]=CONST(4.13D-12*EXP(452/(T))*0.7)
k[OH+MVKOOH-->MVKO2]=CONST(1.90D-12*EXP(190/(T)))
k[OH+MVKOOH-->VGLYOX+OH]=CONST(2.55D-11)
k[OH+NC4CHO-->C51002]=CONST(4.16D-11*0.52)
k[OH+NC4CHO-->NC4CO3]=CONST(4.16D-11*0.48)
k[OH+NC4CO2H-->NOA+CO+HO2]=CONST(2.16D-11)
k[OH+NC4CO3H-->NC4CO3]=CONST(2.52D-11)
k[OH+NISOPNO3-->NC4CHO+NO2]=CONST(8.55D-11)
k[OH+NISOPOOH-->NC4CHO+OH]=CONST(1.03D-10)
k[OH+NO-->HONO]=CONST(KMTO7) k[OH+NO2-->HNO3]=CONST(KMTO8)
k[OH+NO3-->HO2+NO2]=CONST(2.20D-11)
k[OH+O3-->HO2]=CONST(1.70D-12*EXP(-940/(T)))
k[OH+VGLYOX-->CO+ACO3]=CONST(2.95D-11)
k[PAN+OH-->HCHO+CO+NO2]=CONST(9.50D-13*EXP(-650/(T)))
k[PAN-->CH3CO3+NO2]=CONST(KBPAN)
k[PHAN+OH-->HCHO+CO+NO2]=CONST(1.12D-12)
k[PHAN-->HOCH2CO3+NO2]=CONST(KBPAN)
k[PR102HN03+OH-->CHOPRN03+OH]=CONST(1.69D-12)
k[PR102HN03+0H-->PR0N03A02]=CONST(1.90D-12*EXP(190/(T)))
k[PR102HN03+hv-->PR0N03A0+0H]=PHTFKT(7.649D-06,0.682,-0.279)
k[PR202HN03+OH-->NOA+OH]=CONST(3.47D-12)
k[PR202HN03+0H-->PR0N03B02]=CONST(1.90D-12*EXP(190/(T)))
k[PR202HN03+hv-->PR0N03B0+0H]=PHTFKT(7.649D-06,0.682,-0.279)
k[PRN03C02H+OH-->CH3CHO+N02]=CONST(3.14D-13)
k[PRN03C03+H02-->PRN03C02H+03]=CONST(KAPH02*0.29)
k[PRN03C03+H02-->PRN03C03H]=CONST(KAPH02*0.71)
k[PRN03C03+N0-->CH3CH0+N02+N02] = CONST(KAPN0)
k[PRNO3CO3+NO2-->PRNO3PAN]=CONST(KFPAN)
k[PRN03C03+N03-->CH3CH0+N02+N02]=CONST(KR02N03*1.60)
```

```
k[PRN03C03-->CH3CH0+N02]=CONST(1.00D-11*0.7*R02)
k[PRN03C03-->PRN03C02H]=CONST(1.00D-11*0.3*R02)
k[PRN03C03H+OH-->PRN03C03]=CONST(3.77D-12)
k[PRNO3CO3H+hv-->CH3CHO+NO2+OH]=PHTFKT(7.649D-06,0.682,-0.279)
k[PRNO3PAN+OH-->CH3CHO+CO+NO2+NO2] = CONST(1.43D-13)
k[PRNO3PAN-->PRNO3CO3+NO2]=CONST(KBPAN)
k[PROLNO3+OH-->CH3CHOHCHO+NO2]=CONST(1.71D-12)
k[PRONO3AO-->CHOPRNO3+HO2]=CONST(KROPRIM*O2)
k[PRONO3A0-->HCHO+CH3CHO+NO2]=CONST(7.00D+03)
k[PRONO3A02+H02-->PR102HN03]=CONST(KR02H02*0.520)
\verb|k[PRONO3AO2+NO-->PRONO3AO+NO2] = \verb|CONST(KRO2NO)||
k[PRONO3A02+NO3-->PRONO3A0+NO2] = CONST(KRO2NO3)
k[PRONO3A02-->CHOPRNO3]=CONST(6.00D-13*0.2*RO2)
k[PRONO3A02-->PRONO3A0]=CONST(6.00D-13*0.6*R02)
k[PRONO3A02-->PROPOLNO3]=CONST(6.00D-13*0.2*RO2)
k[PRONO3B0-->CH3CH0+HCH0+NO2]=CONST(7.00D+03)
k[PRONO3BO-->NOA+HO2]=CONST(KROSEC*O2)
k[PRONO3B02+H02-->PR202HN03]=CONST(KR02H02*0.520)
k[PRONO3B02+NO-->PRONO3B0+NO2] = CONST(KRO2NO)
k[PRON03B02+N03-->PRON03B0+N02]=CONST(KR02N03)
k[PRONO3B02-->NOA] = CONST(4.00D-14*0.2*R02)
k[PRONO3B02-->PROLNO3]=CONST(4.00D-14*0.2*R02)
k[PRONO3B02-->PRONO3B0]=CONST(4.00D-14*0.6*R02)
k[PROPALO-->CH3CH0+H02+C0]=CONST(KDEC)
k[PROPGLY+OH-->ACETOL+HO2]=CONST(1.20D-11*0.613)
k[PROPGLY+OH-->CH3CHOHCHO+H02]=CONST(1.20D-11*0.387)
k[PROPOLNO3+OH-->ACETOL+NO2]=CONST(9.16D-13)
k[VGLYOX+hv-->HO2+CO+ACO3]=PHTFKT(1.537D-04,0.170,-0.208)
; Sum of Organic Peroxy Radicals
; FILE: ISOPRENE.mcm31.ro2.init.incl
 RO2 = CONST( 0.0 + ISOPAO2 + ISOPBO2 + ISOPCO2 + ISOPDO2 + $
              NISOPO2 + CH200E + CH200 + HMVKA02 + HMVKB02 + $
              CH3CO3 + MVKOO + MVKO2 + CH3O2 + MACO3 + MACRO2 + $
              CH200C + MACROO + C5802 + HC4ACO3 + HC4CCO3 + $
              C5702 + C5902 + HOCH2CO3 + NC4CO3 + C51002 + $
              HYPROPO2 + IPROPOLO2 + PRONO3BO2 + PRONO3AO2 + $
              MGLOO + MGLYOO + GLYOO + ACLOO + HCOCO3 + MVKOHBO2 + $
              MVKOHAO2 + GAOO + NOAOO + CH3CHOO + CO2H3CO3 + $
              ACO3 + HMGLOO + CH3CHOHCO3 + PRNO3CO3 + H13CO2CO3 )
```

A.4.1 Chamber-Features in the Isoprene MCM Model

To account for the dilution of all species inside the SAPHIR chamber, described in chapter 3.1.1, additionally the file ISOPREN.init.dil.mech exists, containing reactions of the type

```
X + DIL -->
```

for each specie of the mechanism. The rates, which are the same for all species, are given in the file ISOPREN.init.dil.rate in the form:

```
k[X + DIL -->] = CONST(DILUTE).
```

The constant DILUTE is derived from the experimental gas flow (equation 3.1): DILUTE = CONST(FLOW/(270.*3600.))

where FLOW is the replenishment gas flow given in m³/h. The reaction partner DIL acts as a mark and switch for the dilution reactions and is set to one or zero depending on the objective of the model run.

The model settings to account for the deposition at the walls described in chapter 3.1.6 are stored in the separate include file saphir.walldep.incl given below. WALLDEP once again is a switch for on and off turning the deposition effect in the model.

```
; Wall deposition
; FILE: saphir.walldep.incl
DV = CONST(3.858e-06)
WALLDEP = CONST(1.)
HN03 -->
HONO -->
H2O2 -->
HO2 -->
03 -->
N205 -->
k[HNO3 --> ] = CONST( WALLDEP * DV )
k[HONO --> ] = CONST( WALLDEP * DV )
k[H202 -->] = CONST(WALLDEP * DV)
k[HO2 \longrightarrow] = CONST(WALLDEP * DV)
k[03 -->] = CONST(WALLDEP * DV)
k[N205 -->] = CONST(WALLDEP * DV)
```

If measured photolysis frequencies (compare chapter 3.2.5) are to be read in, then the include file $saphir.jmeasured_02.incl$ redefines some photolysis reactions adequate to the definitions of the given measured values. Some photolysis frequencies with no measured values given are scaled by the scaling function PHOTMMSC dependent on the measured NO_2 photolysis frequency jno2.

```
hv + N02 -/-> 0 + N0
N02 + hv --> 03 + N0
hv + 03 -/-> 0
N03 + hv -/-> N02 + 0
N03 + hv --> N02 + 03
k[NO3+hv-->NO]=$
        PHOTMMSC(2.485e-2,0.168,0.108,1.165e-2,0.244,0.267,jno2)
k[N03+hv-->N02+03] = $
        PHOTMMSC(1.747e-1,0.155,0.125,1.165e-2,0.244,0.267,jno2)
k[HNO3+hv-->OH+NO2] = $
        PHOTMMSC(9.312e-7,1.230,0.307,1.165e-2,0.244,0.267,jno2)
k[CH3CH0 + hv --> CH302 + CO + H02] = $
        PHOTMMSC(8.443e-6,1.177,0.437,1.165e-2,0.244,0.267,jno2)
k[NO3CH2CHO + hv --> HO2+CO+HCHO+NO2] = $
        PHOTMMSC(3.363e-6,1.296,0.322,1.165e-2,0.244,0.267,jno2)
k[NO3CH2CHO + hv --> NO2+HCOCH2O] = $
        PHOTMMSC(7.549e-6,1.015,0.324,1.165e-2,0.244,0.267,jno2)
```

The IDL program mcmcv prepares a temporary EASY input file, which gives additional definitions for the HONO source of chapter 3.1.2, the HCHO source (chapter 3.1.3), and the background reactivity (chapter 3.1.4). The user has to provide some final settings, like initial values and the name of an ENZ file with measured values and settings that shall be employed as input to make this file complete.

```
k[hv + SHONO --> HONO] = CONST( 4.7e13 * (1. + (RH/11.6)@2) * exp(-3950./T) * jno2 )
SHONO = CONST(1.)
: HCHO source
hv + SHCHO --> HCHO
; k[hv + SHCHO --> HCHO] = CONST(2.8e6); outdated
; (PhD Thesis C. Richter, 2007)
k[hv + SHCHO --> HCHO] = CONST(3.1e13 * jno2 * (0.21 + 2.6e-2*RH) * exp(-2876./T))
SHCHO = CONST(1.)
*************************************
;/BGREAC, Background reactivity
Y + OH --> HO2
k[Y + OH --> HO2] = CONST(2.4e-13)
Y=CONST(200.e-9*M); Y in CO equivalents
**************************
; DILUTION, /DIL
#include ISOPREN.mcm31.dil.init.mech ;dilution mechanism
#include ISOPREN.mcm31.dil.init.rate ;dilution rate
FLOW = CONST(6.); Replenishment flow in m^3/h
DILUTE = CONST(FLOW/(270.*3600.))
DIL = CONST(1.); Switch for dilution
; Water as a variable
INITIAL[H20] = CONST(1.e-4*M)
************************
;/MEASURED, use measured photolysis frequencies (given in ENZ-file)
          and other measured parameters]
#include saphir.jmeasured_02.incl; definitions for further use of jno2
                           ; and jold as scaling factors of other
                           ; photolysis frequencies
SZA = INPUT(sz); solar zenith angle
HV = INPUT(hv) ; switch for light
jno2 = INPUT(jno2)
k[NO2 + HV \longrightarrow O3 + NO] = CONST(jno2)
jo1d = INPUT(jo1d)
k[03 + HV --> 01D] = CONST(jold)
k[HCHO + HV --> H2 + CO] = INPUT(jhcho_m)
k[HCHO + HV --> 2*HO2 + CO] = INPUT(jhcho_r)
k[H202 + HV --> 2*H0] = INPUT(jh2o2)
k[HONO + HV --> OH + NO] = INPUT(jhono)
    = INPUT(t) ; temperature in K
   = INPUT(p) ; pressure in hPa
FLOW = INPUT(dilute); flow into the chamber in m<sup>3</sup>/h
H20 = INPUT(H20) ; mixing ratio of water
************************
```

; FILES:

```
FILES[ENZ] = mcm3.enz

; FACSIMILE PARAMETERS
FACS[HMAX] = 30
FACS[OUTSTEP] = 100000

; INITIALS:
INITIAL[*] = CONST(1.)
INITIAL[$(5H8] =
INITIAL[$(5H8] =
INITIAL[$(1.00] =
I
```

B Tables of Analyzed Experiments

 $(Time_{Light}).$

Table B.1: "Standard experiments" carried out for the characterization of the SAPHIR chamber. During experiments marked with an asterisk *, HCHO was measured with the Hantzsch monitor. They were analyzed for the determination of the water dependence of the SAPHIR chamber HCHO source (q.v. chapter 3.1.3). Listed is the date of the experiment, the finally reached nitrogen oxides (NO_{xFIN}) and ozone (O_{3FIN}) concentrations, the mean NO₂ photolysis frequency $(\overline{J}(NO_2))$, temperature (\overline{T}) , and relative humidity (\overline{RH}) , and the duration of sunlight exposure

Date	NO_{xFIN} [ppb]	O_{3FIN} [ppb]	$ \begin{array}{ c c } \hline J(NO_2) \\ [10^{-3}sec^{-1}] \end{array} $	\overline{T} [K]	$ \overline{RH} $ [%]	$\begin{bmatrix} Time_{Light} \\ [hh:mm] \end{bmatrix}$
2004-06-09 *	1.5	18.9	5.2	305.1	26.1	03:23
2005-02-25	0.1	1.5	2.5	277.7	4.8	05:53
2005-02-27	0.9	6.4	2.8	274.4	46.0	04:48
2005-03-16	1.4	8.0	3.8	295.0	21.9	03:49
2005-05-13 *	0.5	2.1	2.9	289.4	10.6	05:11
2005-06-02	2.2	19.5	3.9	296.2	30.5	05:47
2005-07-17 * a	1.8	8.9	5.7	299.0	22.6	04:00
2005-08-11	0.9	10.1	3.3	294.7	10.9	05:54
2005-09-20	0.8	9.4	4.1	295.7	20.4	04:06
2005-09-28	2.0	7.5	3.5	293.1	24.7	05:20
2006-04-10 *	2.0	9.2	3.0	284.5	47.6	04:21
2006-08-31 b	1.9	7.3	2.7	292.2	29.4	06:31
2006-09-12	3.1	15.1	3.8	301.2	19.1	07:50

^aThe SAPHIR chamber was irradiated for 4 periods, each lasting one hour, followed by an one hour dark phase. During darkness, the relative humidity was increased, so that the mean RH was approximately 0, 10, 30 and 48% for each of the for irradiation phases, respectively.

^bThe PTR-MS and PAN-GC were additionally operated at this day. About 2ppb acetaldehyde and 300ppt PAN were measured at the end of the illumination. It was the first time, the SAPHIR chamber was identified to produce PAN in a standard experiment.

exposure $(Time_{Light})$.

Table B.2: Overview of the isoprene (C5H8), methacrolein (MACR), and methyl vinyl ketone (MVK) \rightarrow ozone experiments. All experiments were analyzed concerning the ozone production in chapter 4. A NO_x gap has been found at the experiments marked with an asterisk *. The additional analysis of the experiments with MACR as initial VOC can be found in chapter 5. Listed are date, starting concentration measured by the GC and name of the initial injected volatile organic compound (VOC_0), mean values of NO_x concentration ($\overline{NO_x}$), NO₂ photolysis frequency ($\overline{J(NO_2)}$), and temperature (\overline{T}) during the time of chamber lighting, measured ozone concentration at the end of

the chamber lightning (O_{3FIN}) , and duration of chamber sunlight

Date		OC_0 ppb]	$\overline{NO_x}$ [ppb]	$ \begin{array}{ c c } \hline J(NO_2) \\ [10^{-3}sec^{-1}] \end{array} $	\overline{T} [K]	O_{3FIN} [ppb]	$\begin{array}{ c c }\hline Time_{Light} & \\ [hh:mm] & \\ \end{array}$
2005-09-	4.5	C5H8	6.8	4.27	294.9	26.4	05:50
21 2005-09- 22	10.4	С5Н8	2.2	4.40	295.9	34.6	05:33
2005-09-	5.3	C5H8	2.5	4.17	298.2	28.1	06:27
2005-09-	9.1	C5H8	2.6	2.80	293.4	27.2	07:47
2005- 10-06 *	12.5	MACR	2.8	2.00	294.1	21.0	09:43
2006-05-	5.4^a	С5Н8	15.4	4.46	300.9	32.8	05:33
2006-05-	8.2	C5H8	1.1	4.84	301.0	36.6	05:50
2006- 05-08 *	11.1	MVK	1.9	4.18	298.2	40.3	06:09
2006-05- 10	10.6	MVK	14.6	4.77	300.3	31.9	06:23
2006-05-	9.9	MVK	1.3	4.84	301.7	43.6	06:34
2006-05-	10.1	MACR	1.0	4.33	302.6	30.5	06:05
2006-05- 15	9.0	MACR	16.5	4.10	300.5	22.7	06:22
2006- 06-12 *	9.3	MVK	2.4	5.34	305.2	66.6	06:57
2006- 06-13 *	8.4	MACR	2.3	5.29	309.4	56.5	06:49
12806- 09-01 *	6.8	MACR	3.0	4.03	300.1	32.9	04:05

C Statistics

χ^2 Goodness-Of-Fit Test

If a measured time series of any parameter M_i is approximated by a fit F_i , the goodness of the fit can be evaluated by the quantity χ^2 . For a time series of N data points and a standard deviation σ_i of each measured data point, M_i is calculated following equation C.1:

$$\chi^{2}(F) = \sum_{i=1}^{N} \left(\frac{F_{i} - M_{i}}{\sigma_{i}}\right)^{2}$$
 (C.1)

The smaller the χ^2 value, the better is the fit, though it can indicate overestimated measure errors σ_i , too. If it is in the same order of magnitude as the number of data points, the fit is still acceptable [153].

Expected Value and Mean

If X_i is a discrete random variable which occurs with the probability p_i ($\sum_i p_i = 1$), then the expected value E(X), also denoted as μ_X is defined as

$$E(X) = \mu_X = \sum_i p_i X_i \tag{C.2}$$

The (arithmetic) mean \bar{X} of a variable X conforms to the average of it:

$$\bar{X} = \frac{1}{n} \cdot \sum_{i=1}^{n} X_i \tag{C.3}$$

For huge samples $n \to \infty$, the mean value matches the expected value $\bar{X} \to E(X)$.

Variance and Standard Deviation

The variance var(X) of a random variable X is defined as the expected value of the square of the deviation of a variable from its own expected value μ_X . It is a measure of how much a variable varies.

$$var(X) = E((X - \mu_X)^2) \tag{C.4}$$

The standard deviation σ is the root of the variance:

$$\sigma(X) = \sqrt{var(x)} \tag{C.5}$$

Covariance

The covariance cov(X, Y) is a measure of how much two random variables X and Y vary together. It is a generalization of the variance as var(X) equals cov(X, X).

$$cov(X,Y) = E((X - \mu_X) \cdot (Y - \mu_Y)) = E(X \cdot Y) - \mu_X \cdot \mu_Y$$
 (C.6)

If the two variables are independent, then their covariance is zero.

Pearson Product-Moment Correlation Coefficient

The correlation coefficient $r_{X,Y}$ corresponds to a weighted covariance. It is defined between two random variables X and Y with expected values μ_X and μ_Y and standard deviations σ_X and σ_Y as:

$$r_{X,Y} = \frac{cov(X,Y)}{\sigma_X \cdot \sigma_Y} \tag{C.7}$$

The standard deviations have to fulfill the precondition that they both are finite and nonzero. The codomain of $r_{X,Y}$ lies between +1 and -1. The value +1 corresponds to an increasing linear relationship, -1 to a decreasing linear relationship between X and Y. If the correlation coefficient is zero, then the variables are independent of each other. In a weighted correlation analysis, the maximum reachable correlation coefficient r_{max} for two ideal (statistically correct error estimates), linear correlated data sets depend on the variance and the mean squared error of each data set. r_{max} converges towards one by rising the variance and/or lowering the mean squared error of the data sets.

Bibliography

- [1] C.F. Schönbein. Beobachtungen über den bei der Elektrolysation des Wassers und dem Ausströmen der gewöhnlichen Electricität aus Spitzen sich entwikkelnder Geruch. Ann. Phys. Chim., 50:616 ff., 1840.
- [2] M.C.M. Alvim-Ferraz, S.I.V. Sousa, M.C. Pereira, and F.G. Martins. Contribution of anthropogenic pollutants to the increase of tropospheric ozone levels in the oporto metropolitan area, portugal since the 19th century. Environmental Pollution, 140(3):516–524, 2006.
- [3] A.J. Haagen-Smit. Chemistry and physiology of Los Angeles Smog. Industrial and Engineering Chemistry, 44(6):1342–1346, 1952.
- [4] S. Chapman. A theory of upper-atmosphere ozone. Mem. Roy. Meteorol. Soc., 3:103–125, 1930.
- [5] S. Chapman. The absorption and dissociative and ionizing effect of monochromatic radiations in an atmosphere on a rotating earth. <u>Proc.</u> Phys. Soc., 43:483, 1931.
- [6] G. M. Dobson. The laminated structure of the ozone in the atmosphere. Quart. J. R. Met. Soc., 99:599–607, 1973.
- [7] The free encyclopedia Wikipedia. Atmospheric chemistry. http://en.wikipedia.org/wiki/Atmospheric_chemistry, 2007.
- [8] Umwelt-und Gesundheitsschutz Zürich (UGZ) and Abteilung Umwelt / Fachbereich Labor. Sommersmog, 2003.
- [9] R. Zellner. Global aspects of atmospheric chemistry, volume 6 of Topics in physical chemistry. Steinkopf Darmstadt, Springer New York; on behalf of Deutsche Bunsen-Gesellschaft für physikalische Chemie, 1999.
- [10] R. Alley, T. Berntsen, N. L. Bindoff, Z. Chen, A. Chidthaisong, P. Friedlingstein, J. Gregory, G. Hegerl, M. Heimann, B. Hewitson, B. Hoskins, F. Joos, J. Jouzel, V. Kattsov, U. Lohmann, M. Manning, T. Matsuno, M. Molina, N. Nicholls, J. Overpeck, D. Qin, G. Raga, V. Ramaswamy, J. Ren, M. Rusticucci, S. Solomon, R. Somerville, T. F. Stocker, P. Stott, R. J. Stouffer, P. Whetton, R.A. Wood, and D. Wratt. Climate change 2007: The physical science basis, summary for policymakers. Technical report, Intergovernmetal Panel on Climate Change (WMO, UNEP), 2007.

- [11] H. Kraus. <u>Die Atmosphäre der Erde</u>. Springer, Berlin Heidelberg, 3rd edition, 2004.
- [12] J.A. Logan. Tropospheric ozone: Seasonal behavior, trends, and anthropogenic influence. <u>Journal of Geophysical Research</u>, 90:10463–10482, 1985.
- [13] S.J. Oltmans and H. Levy. Surface ozone measurements from a global network. <u>Atmospheric Environment Part A - General Topics</u>, 28(1):9–24, 1994.
- [14] U. Ackermann-Liebrich, H.R. Anderson, T. Bellander, J. Brain, B. Brunekreef, A. Cohen, E. Dybing, F. Forastiere, J. Heinrich, U. Heinrich, S.T. Holgate, K. Katsouyanni, F.J. Kelly, M. Lippmann, R. Maynard, J. Pekkanen, A. Peters, R. Rapp, R.O. Salonen, J. Samet, B. Seifert, J. Sunyer, J. Vandenberg, H. Walton, and H.E. Wichmann. Health aspects of air pollution with particulate matter, ozone and nitrogen dioxide. Report on a WHO Working Group, 2003.
- [15] Scientific Committee on Health and Environmental Risks (SCHER). Opinion on "new evidence of air pollution effects on human health and the environment", 2005.
- [16] M. Schaub, P. Jakob, L. Bernhard, J.L. Innes, J.M. Skelly, and N. Kräuchi. Ozone injury database. http://www.ozone.wsl.ch, 2002.
- [17] W.L. Chameides, Li Xingsheng, Tang Xiaoyan, Zhou Xiuji, Luo Chao, C.S. Kiang, J. St John, R.D. Saylor, S.C. Liu, K.S. Lam, T. Wang, and F. Glorgi. Is ozone pollution affecting crop yields in china? <u>Geophysical</u> Research Letters, 26(7):867–70, 1999.
- [18] H.X. Wang, C.S. Kiang, X.Y. Tang, X.J. Zhou, and W.L. Chameides. Surface ozone: A likely threat to crops in yangtze delta of china. Atmospheric Environment, 39(21):3843–3850, 2005.
- [19] European Union. Directive 2002/3/EC of the European parliament and of the council of 12 february 2002 relating to ozone in ambient air. Official Journal of the European Communities, L 67/14, 2002.
- [20] Bundesministerium für Umwelt. Informationen zum Luftschadstoff Ozon (O₃). http://www.umweltbundesamt.de/luft/schadstoffe/archiv/infoblatt_ozon.pdf, 2005.
- [21] R. Atkinson and J. Arey. Gas-phase tropospheric chemistry of biogenic volatile organic compounds: a review. <u>Atmospheric environment</u>, 37:S197–S219, 2003.
- [22] D.S. Lee, I. Kohler, E. Grobler, F. Rohrer, R. Sausen, L. Gallardo-Klenner, J.G.J. Olivier, F.J. Dentener, and A.F. Bouwman. Estimations of global NO_x emissions and their uncertainties. <u>Atmospheric environment</u>, 31(12):1735–1749, 1997.

- [23] S. Beirle, N. Spichtinger, A. Stohl, K. L. Cummins, T. Turner, D. Boccippio, O. R. Cooper, M. Wenig, M. Grzegorski, U. Platt, and T. Wagner. Estimating the NO_x produced by lightning from GOME and NLDN data: a case study in the Gulf of Mexico. <u>Atmospheric Chemistry and Physics</u>, 6(4):1075–1089, 2006.
- [24] R. Atkinson. Atmospheric chemistry of VOCs and NO_x. <u>Atmospheric Environment</u>, 34(12-14):2063–2101, 2000.
- [25] K.Y. Wang, J.A. Pyle, and D.E. Shallcross. Formulation and evaluation of IMS, an interactive three-dimensional tropospheric chemical transport model 1. model emission schemes and transport processes. <u>Journal of</u> Atmospheric Chemistry, 38(2):195–227, 2001.
- [26] K. E. Pickering, A. M. Thompson, J. R. Scala, W. K. Tao, and J. Simpson. Ozone production potential following convective redistribution of biomass burning emissions. J. Atmos. Chem., 14:297–313, 1992.
- [27] L. W. Horowitz. Past, present, and future concentrations of tropospheric ozone and aerosols: Methodology, ozone evaluation, and sensitivity to aerosol wet removal. <u>Journal of Geophysical Research</u>, 111(D22211), 2006.
- [28] N. Toenges-Schuller, O. Stein, F. Rohrer, A. Wahner, A. Richter, J.P. Burrows, S. Beirle, T. Wagner, U. Platt, and C.D. Elvidge. Global distribution pattern of anthropogenic nitrogen oxide emissions: Correlation analysis of satellite measurements and model calculations. <u>Journal of Geophysical Research D: Atmospheres</u>, 111:D05312, 2006.
- [29] G.P. Brasseur, M. Schultz, C. Granier, M. Saunois, M. Botzet, E. Roeckner, and S. Walters. Impact of climate change on the future chemical compositions of the global troposphere. <u>Journal of Climate Special Section</u>, 19(16):3932–3951, 2006.
- [30] C. Warneke, J. A. de Gouw, P. D. Goldan, W. C. Kuster, E. J. Williams, B. M. Lerner, R. Jakoubek, S. S. Brown, H. Stark, M. Aldener, A. R. Ravishankara, J. M. Roberts, M. Marchewka, S. Bertman, D. T. Sueper, S. A. McKeen, J. F. Meagher, and F. C. Fehsenfeld. Comparison of daytime and nighttime oxidation of biogenic and anthropogenic VOCs along the New England coast in summer during New England Air Quality Study 2002. Journal of Geophysical Research, 109, 2004.
- [31] A. Guenther, C.N. Hewitt, D. Erickson, R. Fall, C. Geron, T. Graedel, P. Harley, L. Klinger, M. Lerdau, W.A. Mc Kay, T. Pierce, B. Scholes, R. Steinbrecher, R. Tallaraja, J. Taylor, and P. Zimmermann. A global model of natural volatile organic compound emissions. <u>Journal of Geophysical Research</u>, D, Atmospheres, 100(D5):8873–8892, 1995.

- [32] A. Guenther, C. Geron, T. Pierce, B. Lamb, P. Harley, and R. Fall. Natural emissions of non-methane volatile organic compounds, carbon monoxide, and oxides of nitrogen from north america. <u>Atmospheric Enviroment</u>, 34:2205–2230, 2000.
- [33] G. König, M. Brunda, H. Puxbaum, C.N. Hewitt, S.C. Duckham, and J. Rudolph. Relative contribution of oxygenated hydrocarbons to the total biogenic VOC emissions of selected mid-european agricultural and natural plant species. Atmospheric Environment, 29:861–874, 1995.
- [34] R. Atkinson and J. Arey. Atmospheric chemistry of biogenic organic compounds. Accounts of Chemical Research, 31(9):574–583, 1998.
- [35] D. Simpson, W. Winiwarter, G. Börjesson, S. Cinderby, A. Ferreiro, A. Guenther, C.N. Hewitt, R. Janson, M. A. K. Khalil, S. Owen, T.E. Pierce, H. Puxbaum, M. Shearer, U. Skiba, R. Steinbrecher, L. Tarrasón, and M.G. Öquist. Inventorying emissions from nature in europe. <u>Journal</u> of geophysical research, 104(D7):8113–8152, 1999.
- [36] J.H. Seinfeld, P.G. Risser, J.A. Dutton, and M.G. Wolman. Rethinking the ozone problem in urban and rural air pollution. National Academic Press, Washington D.C., 1991.
- [37] W.P.L. Carter. Computer modeling of environmental chamber measurements of maximum incremental reactivities of volatile organic compounds. Atmospheric Environment, 29(18):2513–2527, 1995.
- [38] W.P.L. Carter, J.A. Pierce, D. Luo, and I.L. Malkina. Environmental chamber study of maximum incremental reactivities of volatile organic compounds. Atmospheric Environment, 29(18):2499–2511, 1995.
- [39] R.G. Derwent, M. E. Jenkin, S.M. Saunders, and M.J. Pilling. Photochemical ozone creation potentials for organic compounds in northwest Europe calculated with a master chemical mechanism. <u>Atmospheric environment</u>, 32(14-15):2429–2441, 1998.
- [40] M.E. Jenkin and G.D. Hayman. Photochemical ozone creation potentials for oxygenated volatile organic compounds: sensitivity to variations in kinetic and mechanistic parameters. <u>Atmospheric Environment</u>, 33(8):1275–1293, 1999.
- [41] J.D. Fuentes, D. Wang, H.H. Neumann, T.J. Gillespie, G. Den Hartog, and T.F. Dann. Ambient biogenic hydrocarbons and isoprene emissions from a mixed deciduous forest. <u>Journal of Atmospheric Chemistry</u>, 25(1):67–95, 1996.
- [42] P. Campuzano-Jost, M.B. Williams, L. D'Ottone, and A.J. Hynes. Kinetics and mechanism of the reaction of the hydroxyl radical with h(8)-isoprene and d(8)-isoprene: Isoprene absorption cross sections, rate coefficients, and the mechanism of hydroperoxyl radical production. <u>Journal</u> of Physical Chemistry A, 108(9):1537–1551, 2004.

- [43] C. Warneke, R. Holzinger, A. Hansel, A. Jordan, W. Lindinger, U. Poschl, J. Williams, P. Hoor, H. Fischer, P.J. Crutzen, H.A. Scheeren, and J. Lelieveld. Isoprene and its oxidation products methyl vinyl ketone, methacrolein, and isoprene related peroxides measured online over the tropical rain forest of surinam in march 1998. <u>Journal of Atmospheric</u> Chemistry, 38:167–185, 2001.
- [44] E.C. Apel, D.D. Riemer, A. Hills, W. Baugh, J. Orlando, I. Faloona, D. Tan, W. Brune, B. Lamb, H. Westberg, M.A. Carroll, T. Thornberry, and C.D. Geron. Measurement and interpretation of isoprene fluxes and isoprene, methacrolein, and methyl vinyl ketone mixing ratios at the prophet site during the 1998 intensive art. no. 4034. <u>Journal of Geophysical Research Atmospheres</u>, 107(D3):4034, 2002.
- [45] C. Plaß-Dülmer and H. Berresheim. Trends von atmosphärischen Kohlenwasserstoffen (VOC) und ihre Klimarelevanz. GAW Brief des Deutschen Wetterdienstes, 27:1–2, 2005.
- [46] R. Atkinson, D.L. Baulch, R.A. Cox, J.N. Crowley, R.F. Hampson, R.G. Hynes, M.E. Jenkin, M.J. Rossi, and J. Troe. Evaluated kinetic and photochemical data for atmospheric chemistry: Volume II gas phase reactions of organic species. <u>Atmospheric Chemistry and Physics</u>, 6:3625–4055, 2006.
- [47] T. Biesenthal, Q. Wu, P.B. Shepson, H.A. Wiebe, K.G. Anlauf, and G.I. Mackay. A study of relationships between isoprene, its oxidation products, and ozone, in the lower fraser valley, bc. <u>Atmospheric Environment</u>, 31(14):2049–2058, 1997.
- [48] Suzanne E. Paulson, Richard C. Flagan, and John H. Seinfeld. Atmospheric photooxidation of isoprene part I: The hydroxyl radical and ground state atomic oxygen reactions. <u>International Journal of Chemical</u> Kinetics, 24:79–101, 1992.
- [49] W.P.L. Carter and R. Atkinson. Development and evaluation of a detailed mechanism for the atmospheric reactions of isoprene and NO_x . International Journal of Chemical Kinetics, 28(7):497–530, 1996.
- [50] C. Wiedinmyer, S. Friedfeld, W. Baugh, J. Greenberg, A. Guenther, M. Fraser, and D. Allen. Measurement and analysis of atmospheric concentrations of isoprene and its reaction products in central texas. Atmospheric Environment, 35(6):1001–1013, 2001.
- [51] T.K. Starn, P.B. Shepson, S.B. Bertman, J.S. White, B.G. Splawn, D.D. Riemer, R.G. Zika, and K. Olszyna. Observations of isoprene chemistry and its role in ozone production at a semirural site during the 1995 Southern Oxidants Study. <u>Journal of Geophysical Research</u>, 103(D17):22425–22435, 1998.

- [52] S. Gilge. Peroxiacetylnitrat ein wichtiger troposphärischer Spurenstoff. GAW Brief des Deutschen Wetterdienstes, 34:1–2, 2006.
- [53] Die freie Enzykopädie Wikipedia. Peroxyacetylnitrat. http://de.wikipedia.org/wiki/Peroxiacetylnitrat, 2006.
- [54] H. Hakola, V. Tarvainen, T. Laurila, V. Hiltunen, H. Hellen, and P. Keronen. Seasonal variation of VOC concentrations above a boreal coniferous forest. Atmospheric Environment, 37(12):1623–1634, 2003.
- [55] J. Williams, J.M. Roberts, F.C. Fehsenfeld, S.B. Bertman, M.P. Buhr, P.D. Goldan, G. Hübler, W.C. Kuster, T.B. Ryerson, M. Trainer, and V. Young. Regional ozone from biogenic hydrocarbons deduced from airborne measurements of PAN, PPN, and MPAN. <u>Geophysical Research</u> Letters, 24(9):1099–1102, 1997.
- [56] J.M. Roberts, J. Williams, K. Baumann, M.P. Buhr, P.D. Goldan, J. Holloway, G. Hübler, W.C. Kuster, S.A. McKeen, T.B. Ryerson, M. Trainer, E.J. Williams, F.C. Fehsenfeld, S.B. Bertram, G. Nouaime, C. Seaver, G. Grodzinsky, M. Rodgers, and V.L. Young. Measurements of PAN, PPN, and MPAN made during the 1994 and 1995 Nashville Intensives of the Southern Oxidant Study: Implications for regional ozone production from biogenic hydrocarbons. <u>Journal of Geophysical Research</u>, 103(D17):22473–22490, 1998.
- [57] S. Rahmstorf and H.J. Schellnhuber. <u>Der Klimawandel</u>. C.H.Beck Wissen. C.H.Beck, München, 4th edition, 2007.
- [58] W.R. Stockwell, F. Kirchner, M. Kuhn, and S. Seefeld. A new mechanism for regional atmospheric chemistry modeling. <u>Journal of Geophysical Research</u>, 102(D22):25847–25879, 1997.
- [59] H. Geiger, I. Barnes, I. Bejan, T. Benter, and M. Spittler. The tropospheric degradation of isoprene: An updated module for the regional atmospheric chemistry mechanism. <u>Atmospheric Environment</u>, 37(11):1503–1519, 2003.
- [60] G.P. Brasseur, D.A. Hauglustaine, S. Walters, P.J. Rasch, J.-F. Muller, C. Granier, and X.X. Tie. MOZART, a global chemical transport model for ozone and related chemical tracers. 1. model description. <u>Journal of</u> Geophysical Research, 103(D21):28265–89, 1998.
- [61] D. A. Hauglustaine, G. P. Brasseur, S. Walters, P. J. Rasch, J.-F. Müller, L. K. Emmons, and M. A. Carroll. MOZART, a global chemical transport model for ozone and related chemical tracers, 1, model results and evaluation. <u>Journal of Geophysical Research</u>, 103:28291–28336, 1998.
- [62] L.W. Horowitz, S. Walters, D.L. Mauzerall, L.K. Emmons, P.J. Rasch, C. Granier, X. Tie, J.-F. Lamarque, M.G. Schultz, G.S. Tyndall, J.J. Orlando, and G.P. Brasseur. A global simulation of tropospheric ozone

- and related tracers: Description and evaluation of MOZART, version 2. Journal of Geophysical Research, 108(D24):4784, 2003.
- [63] P.G. Pinho, C.A. Pio, and M.E. Jenkin. Evaluation of isoprene degradation in the detailed tropospheric chemical mechanism, MCM v3, using environmental chamber data. <u>Atmospheric Environment</u>, 39(7):1303–1322, 2005.
- [64] Webpage of the EUROCHAMP project. http://www.eurochamp.org, 2007.
- [65] M.E. Jenkin and K.C. Clemitshaw. Ozone and other secondary photochemical pollutants: chemical processes governing their formation in the planetary boundary layer. <u>Atmospheric Environment</u>, 34(16):2499–2527, 2000.
- [66] The free encyclopedia Wikipedia. Ultraviolet. http://en.wikipedia.org/wiki/Ultraviolet, 2007.
- [67] M.E. Jenkin, S.M. Saunders, R.G. Derwent, and M.J. Pilling. Development of a reduced speciated VOC degradation mechanism for use in ozone models. Atmospheric Environment, 36(30):4725–4734, 2002.
- [68] P. Giacopelli, K. Ford, C. Espada, and P.B. Shepson. Comparison of the measured and simulated isoprene nitrate distributions above a forest canopy. Journal of Geophysical Research, 110(D1), 2005.
- [69] D.A. Day, M.B. Dillon, P.J. Wooldridge, J.A. Thornton, R.S. Rosen, E.C. Wood, and R.C. Cohen. On alkyl nitrates, O_3 , and the "missing NO_y ". <u>Journal of Geophysical Research-Atmospheres</u>, 108(D16):4501, 2003.
- [70] S. P. Sander, R. R. Friedl, A. R. Ravishankara, D. M. Golden, C. E. Kolb, M. J. Kurylo, M. J. Molina, G.K. Moortgat, H. Keller-Rudek, B. J. Finlayson-Pitts, P. H. Wine, R. E. Huie, and V. L. Orkin. Chemical kinetics and photochemical data for use in atmospheric studies evaluation number 15. JPL Publication, 06-2:1-522, 2006.
- [71] Webpage of NASA/JPL data evaluation. http://jpldataeval.jpl.nasa.gov/index.html, 2004.
- [72] Webpage of the International Council for Science: Committee on Data for Science and Technology (CODATA). http://www.codata.org, 2007.
- [73] R. Atkinson, D.L. Baulch, R.A. Cox, J.N. Crowley, R.F. Hampson, R.G. Hynes, M.E. Jenkin, M.J. Rossi, and J. Troe. Evaluated kinetic and photochemical data for atmospheric chemistry: Volume I gas phase reactions of O_x, HO_x, NO_x and SO_x species. <u>Atmospheric Chemistry and Physics</u>, 4:1461–1738, 2004.

- [74] R. Atkinson, D.L. Baulch, R.A. Cox, J.N. Crowley, R.F. Hampson, R.G. Hynes, M.E. Jenkin, M.J. Rossi, and J. Troe. Evaluated kinetic and photochemical data for atmospheric chemistry: Volume III gas phase reactions of inorganic halogens. <u>Atmospheric Chemistry and Physics</u>, 7:981–1191, 2007.
- [75] Webpage of IUPAC subcommittee for gas kinetic data evaluation. http://www.iupac-kinetic.ch.cam.ac.uk, 2006.
- [76] M.E. Jenkin, S.M. Saunders, and M.J. Pilling. The tropospheric degradation of volatile organic compounds: a protocol for mechanism development. Atmospheric environment, 31(1):81, 1997.
- [77] S.M. Saunders, M.E. Jenkin, R.G. Derwent, and M.J. Pilling. Protocol for the development of the Master Chemical Mechanism, MCM v3 (Part A): tropospheric degradation of non-aromatic volatile organic compounds. Atmospheric Chemistry and Physics, 3:161–180, 2003.
- [78] M.E. Jenkin, S.M. Saunders, V. Wagner, and M.J. Pilling. Protocol for the development of the Master Chemical Mechanism, MCM v3 (Part B): tropospheric degradation of aromatic volatile organic compounds. Atmospheric Chemistry and Physics, 3:181–193, 2003.
- [79] S.M. Saunders, M.E. Jenkin, R.G. Derwent, and M.J. Pilling. Report summary: World wide web side of a master chemical mechanism (MCM) for use in tropospheric chemistry. <u>Atmospheric Environment</u>, 31:1249, 1997.
- [80] A. R. Rickard, M. Pilling, and M. Jenkin. Webpage of the Master Chemical Mechanism MCM. http://mcm.leeds.ac.uk/MCM/home.htt, 2004.
- [81] Webpage of the knowledge transfer project: MCM IUPAC integration. http://www.iupac-kinetic.ch.cam.ac.uk/kt_project.html, 2007.
- [82] M.W. Gery, G.Z. Whitten, J.P. Killus, and M.C. Dodge. A photochemical kinetics mechanism for urban and regional scale computer modeling. Journal of Geophysical Research, 94(D10):12925–56, 1989.
- [83] U. Pöschl, R. von Kuhlmann, N. Poisson, and P.J. Crutzen. Development and intercomparison of condensed isoprene oxidation mechanisms for global atmospheric modeling. <u>Journal of Atmospheric Chemistry</u>, 37:29– 52, 2000.
- [84] W.P.L. Carter. Documentation of the saprc-99 chemical mechanism for voc reactivity assessment. Technical report, Air Pollution Research Center and College of Engineering Center for Environmental Research an Technology University of California Riverside, California 92521, 08.05.2000 2000.
- [85] A Russell and R Dennis. Narsto critical review of photochemical models and modeling. Atmospheric Environment, 34(12-14):2283–2324, 2000.

- [86] J. Bossmeyer, T. Brauers, C. Richter, F. Rohrer, R. Wegener, and A. Wahner. Simulation chamber studies on the NO₃ chemistry of atmospheric aldehydes. Geophysical Research Letters, 33(18), 2006.
- [87] ITT Corporation. IDL The Data Visualization & Analysis Platform. http://www.ittvis.com/idl/index.asp, 2007.
- [88] T. Brauers and F. Rohrer. User's manual: Easy AtmoSpheric chemistrY (ver.2). http://www.fz-juelich.de/icg/icg-2/easy_doc, 1999.
- [89] H. London, Th. Neuwohner, D. Poppe, M. Wallasch, and S. Johanning. ICG 3 Programme zur Auswertung von Feldkampagnen, volume 2648 of Berichte des Forschungszentrums Jülich. Forschungszentrum Jülich, Jülich, 1992.
- [90] R. Bauer. Entwicklung von Softwarewerkzeuten zur Messdatenorganisation und Datenvisualisierung für die Programmierumgebung IDL im Institut für Chemie und Dynamik der Geosphäre des Forschungszentrum Jülich. Berichte des Forschungszentrums Jülich, 3786, 2000.
- [91] B. Bohn and H. Zilken. Model-aided radiometric determination of photolysis frequencies in a sunlit atmosphere simulation chamber. <u>Atmospheric</u> Chemistry and Physics, 5:191–206, 2005.
- [92] B. Bohn, F. Rohrer, T. Brauers, and A. Wahner. Actinometric measurements of NO₂ photolysis frequencies in the atmosphere simulation chamber SAPHIR. Atmospheric Chemistry and Physics, 5:493–503, 2005.
- [93] J. Bossmeyer. Studies of Aldehydes in an Atmosphere Simulation Chamber. Dissertation, Heidelberg, Univ., 2006.
- [94] S. Rodriguez Bares. <u>Untersuchungen zur Ozonolyse einfacher Alkene in der Atmosphären-Simulationskammer SAPHIR</u>. Phd, Forschungszentrum, Zentralbibliothek, 2003.
- [95] M. Karl, T. Brauers, H.P. Dorn, F. Holland, M. Komenda, D. Poppe, F. Rohrer, L. Rupp, A. Schaub, and A. Wahner. Kinetic study of the OHisoprene and O₃-isoprene reaction in the atmosphere simulation chamber, SAPHIR. <u>Geophysical Research Letters</u>, 31(5):5117, 2004.
- [96] M. Karl, H.P. Dorn, F. Holland, R. Koppmann, D. Poppe, L. Rupp, A. Schaub, and A. Wahner. Product study of the reaction of OH radicals with isoprene in the atmosphere simulation chamber SAPHIR. <u>Journal</u> of Atmospheric Chemistry, 55(2):167–187, 2006.
- [97] H. Fuchs. <u>Measurement of Peroxy Radicals using Laser-Induced Fluorescence Technique</u>. Phd, Humboldt Universität, 2006.
- [98] B. Aumont, F. Chervier, and S. Laval. Contribution of HONO sources to the $\rm NO_x/HO_x/O_3$ chemistry in the polluted boundary layer. Atmospheric Environment, 37(4):487–498, 2003.

- [99] B. Vogel, H. Vogel, J. Kleffmann, and R. Kurtenbach. Measured and simulated vertical profiles of nitrous acid Part II. Model simulations and indications for a photolytic source. <u>Atmospheric Environment</u>, 37(21):2957–2966, 2003.
- [100] W. P. L. Carter, R. Atkinson, A. M. Winer, and J. N. Pitts. Evidence for chamber-dependent radical sources: Impact on kinetic computer models for air pollution. Int. J. Chem. Kinet., XIII:735–740, 1981.
- [101] W. P. Carter, R. Atkinson, A. M. Winer, and J. N. Pitts. Experimental investigation of chamber-dependent radical sources. <u>Int. J. Chem. Kinet.</u>, XIV:1071–1103, 1982.
- [102] F. Sakamaki, S. Hatakeyama, and H. Akimoto. Formation of nitrous acid and nitric oxide in the heterogeneous dark reaction of nitrogen dioxide and water vapor in a smog chamber. <u>Int. J. Chem. Kinet.</u>, XV:1013–1029, 1983.
- [103] J. N. Pitts, E. Sanhueza, R. Atkinson, W. P. L. Carter, A. M. Winer, G. W. Harris, and C. N. Plum. An investigation of the dark formation of nitrous acid in environmental chambers. <u>Int. J. Chem. Kinet.</u>, XVI:919– 939, 1984.
- [104] J. Kleffmann, K.H. Becker, and P. Wiesen. Heterogeneous NO₂ conversion process on acid surfaces: Possible atmospheric implications. <u>Atmos.</u> Environ., 32:2721–2729, 1998.
- [105] B.J. Finlayson-Pitts, L.M. Wingen, A.L. Sumner, D. Syomin, and K.A. Ramazan. The heterogeneous hydrolysis of NO₂ in laboratory systems and in outdoor and indoor atmospheres: An integrated mechanism. Physical Chemistry Chemical Physics, 5(2):223–242, 2003.
- [106] F. Rohrer, B. Bohn, T. Brauers, D. Brüning, F.-J. Johnen, A. Wahner, and J. Kleffmann. Characterisation of the photolytic HONO-source in the atmosphere simulation chamber SAPHIR. <u>Atmospheric Chemistry and Physics</u>, 5:2189 2201, 2005.
- [107] M.A. Hutterli, R. Rothlisberger, and R.C. Bales. Atmosphereto-snow-to-firn transfer studies of HCHO at Summit, Greenland. Geophysical-Research-Letters, 26(12):1691–1694, 1999.
- [108] A.L. Sumner and P.B. Shepson. Snowpack production of formaldehyde and its effect on the arctic troposphere. Nature, 398(6724):230–233, 1999.
- [109] M. Karl. <u>Modellierung atmosphärisch-chemischer Reaktionen in der Tageslicht- Atmosphären-Simulationskammer SAPHIR</u>. Phd, Forschungszentrum, 2004.
- [110] F. Rohrer. Personal communication, 2007.

- [111] K.C. Clemitshaw. review of instrumentation and techniques ground-based measurement for and airborne field studies tropospheric of gas-phase chemistry. Critical-Reviews-in-Environmental-Science-and-Technology, 34(1):1-108, 2004.
- [112] B. A. Ridley, F. E. Grahek, and J. G. Walega. A small, high-sensitivity, medium-response ozone detector suitable for measurements from light aircraft. J. Atmos. Oceanic Technol., 9:142–148, 1992.
- [113] E. Schlosser, B. Bohn, T. Brauers, H.P. Dorn, H. Fuchs, R. Häseler, A. Hofzumahaus, F. Holland, F. Rohrer, L.O. Rupp, M. Siese, R. Tillmann, and A. Wahner. Intercomparison of two hydroxyl radical measurement techniques at the atmosphere simulation chamber SAPHIR. Journal of atmospheric chemistry, 56(2):187–205, 2007.
- [114] M. Hausmann, U. Brandenburger, T. Brauers, and H.-P. Dorn. Detection of tropospheric OH radicals by long-path differential-optical-absorption spectroscopy: Experimental setup, accuracy, and precision. <u>Journal of</u> Geophysical Research, 102:16,011–16,022, 1997.
- [115] H.-P. Dorn, U. Brandenburger, T. Brauers, and M. Hausmann. A new in-situ laser long-path absorption instrument for the measurement of tropospheric OH radicals. <u>Journal of Atmospheric Sciences</u>, 52:3373— 3380, 1995.
- [116] F. Holland, M. Hessling, and A. Hofzumahaus. In-situ measurement of tropospheric OH radicals by laser-induced fluorescence - a description of the KFA instrument. <u>Journal of the Atmospheric Sciences</u>, 52:3393–3401, 1995.
- [117] F. Holland, A. Hofzumahaus, H.-J. Schäfer, A. Kraus, and H. W. Pätz. Measurements of OH and HO₂ radical concentrations and photolysis frequencies during BERLIOZ. <u>Journal of Geophysical Research</u>, 108(D4):8246, 2003.
- [118] W. Lindinger, A. Hansel, and A. Jordan. On-line monitoring of volatile organic compounds at pptv levels by means of proton-transfer-reaction mass spectrometry (PTR-MS) medical applications, food control and environmental reasearch. <u>International Journal of Mass Spectrometry</u>, <u>Ion Processes</u>, 173:191–241, 1998.
- [119] D. Klemp, K. Mannschreck, and B. Mittermaier. Comparison of two different HCHO measurement techniques: TDLAS and a commercial Hantzsch monitor - results from long-term measurements in a city plume during the EVA-experiment. In <u>Annual report 2002 of the EUROTRAC subproject GENEMIS / International Scientific Secretariat, GSF</u>, Munich, 2002.

- [120] F. Rohrer and D. Brüning. Surface NO and NO₂ mixing ratios measured between 30-degrees-N and 30-degrees-S in the atlantic region. <u>Journal of Atmospheric Chemistry</u>, 15(3-4):253–267, 1992.
- [121] J. Heland, J. Kleffmann, R. Kurtenbach, and P. Wiesen. A new instrument to measure gaseous nitrous acid (HONO) in the atmosphere. Environmental science & technology, 35(15):3207–3212, 2001.
- [122] J. E. Lovelock. A sensitive detector for gas chromatography. <u>Journal of Chromatography A</u>, 1:35–46, 1958.
- [123] A. Volz-Thomas, I. Xueref, and R. Schmitt. An automatic gas chromatograph and calibration system for ambient measurements of PAN and PPN. <u>Environmental science and pollution research</u>, 9(Special 4):72 76, 2002.
- [124] F.M. Flocke, A.J. Weinheimer, A.L. Swanson, J.M. Roberts, R. Schmitt, and S. Shertz. On the measurement of PANs by gas chromatography and electron capture detection. <u>Journal of Atmospheric Chemistry</u>, 52(1):19–43, 2005.
- [125] A. Hofzumahaus, A. Kraus, and M. Müller. Solar actinic flux spectroradiometry: a technique for measuring photolysis frequencies in the atmosphere. Applied Optics, 38(21):4443–4460, 1999.
- [126] A. Kraus and A. Hofzumahaus. Field measurements of atmospheric photolysis frequencies for O₃, NO₂, HCHO, CH₃CHO, H₂O₂, and HONO by UV spectroradiometry. <u>Journal of Atmospheric Chemistry</u>, 31(1-2):161–180, 1998.
- [127] B. Bohn. Solar spectral actinic flux and photolysis frequency measurements in a deciduous forest. <u>Journal of Geophysical Research D:</u> Atmospheres, 111:D15303, 2006.
- [128] M.E. Jenkin, T.J. Davies, and J.R. Stedman. The origin and day-of-week dependence of photochemical ozone episodes in the UK. <u>Atmospheric</u> Environment, 36(6):999–1012, 2002.
- [129] C. Bloss, V. Wagner, A. Bonzanini, M.E. Jenkin, K. Wirtz, M. Martin-Reviejo, and M.J. Pilling. Evaluation of detailed aromatic mechanisms (MCM v3 and MCM v3.1) against environmental chamber data. Atmospheric Chemistry and Physics Discussions, 4:5683–5731, 2004.
- [130] C. Bloss, V. Wagner, M. E. Jenkin, R. Volkamer, W. J. Bloss, J. D. Lee, D. E. Heard, K. Wirtz, M. Martin-Reviejo, G. Rea, J. C. Wenger, and M. J. Pilling. Development of a detailed chemical mechanism (MCM v3.1) for the atmospheric oxidation of aromatic hydrocarbons. Atmospheric Chemistry and Physics Discussions, 4:5733-5788, 2004.

- [131] W.P.L. Carter, D. Luo, I.L. Malkina, and D. Fitz. The University of California, Riverside environmental chamber data base for evaluating oxidant mechanisms: Indoor chamber experiments through 1993. Technical report, United States Environmental Protection Agency, 1996.
- [132] F. Rohrer. Personal communication, 2005.
- [133] R. Wegener. Personal communication, 2006.
- [134] M.C. Dodge. Chemical oxidant mechanisms for air quality modeling: critical review. Atmospheric Environment, 34(12-14):2103–2130, 2000.
- [135] N. Bell, D.E. Heard, M.J. Pilling, and A.S. Tomlin. Atmospheric lifetime as a probe of radical chemistry in the boundary layer. <u>Atmospheric Environment</u>, 37(16):2193–2205, 2003.
- [136] T.A. Kovacs, W.H. Brune, H. Harder, M. Martinez, J.B. Simpas, G.J. Frost, E. Williams, T. Jobson, C. Stroud, V. Young, A. Fried, and B. Wert. Direct measurements of urban OH reactivity during Nashville SOS in summer 1999. <u>Journal of Environmental Monitoring</u>, 5(1):68–74, 2003.
- [137] P. Di Carlo, W.H. Brune, M. Martinez, H. Harder, R. Lesher, X.R. Ren, T. Thornberry, M.A. Carroll, V. Young, P.B. Shepson, D. Riemer, E. Apel, and C. Campbell. Missing OH reactivity in a forest: Evidence for unknown reactive biogenic VOCs. <u>SCIENCE</u>, 304(5671):722–725, 2004.
- [138] L.I. Kleinman, P.H. Daum, J.H. Lee, Yin-Nan Lee, L.J. Nunnermacker, S.R. Springston, L. Newman, J. Weinstein-Lloyd, and S. Sillman. Dependence of ozone production on NO and hydrocarbons in the troposphere. Geophysical Research Letters, 24(18):2299–2302, 1997.
- [139] P.H. Daum, L.I. Kleinman, D. Imre, L.J. Nunnermacker, Y.-N. Lee, S.R. Springston, L. Newman, J. Weinstein-LLoyd, R.J. Valente, R.E. Imhoff, R.L. Tanner, and J.F. Meagher. Analysis of O₃ formation during a stagnation episode in central Tennessee in summer 1995. <u>Journal of Geophysical Research</u>, 105(D7):9107-9119, 2000.
- [140] F. Rohrer and H. Berresheim. Strong correlation between levels of tropospheric hydroxyl radicals and solar ultraviolet radiation. <u>Nature</u>, 442(7099):184–7, 2006.
- [141] A.B. Guenther, P.R. Zimmermann, P.C. Harley, R.K. Monson, and R. Fall. Isoprene and monoterpene emission rate variability - model evaluations and sensitivity analyses. <u>Journal of Geophysical Research atmospheres</u>, 98(D7):12609–12617, 1993.

- [142] W. Grabmer, J. Kreuzwieser, A. Wisthaler, C. Cojocariu, M. Graus, H. Rennenberg, D. Steigner, R. Steinbrecher, and A. Hansel. VOC emissions from Norway spruce (Picea abies L. [Karst]) twigs in the field - Results of a dynamic enclosure study. <u>Atmospheric Environment</u>, 40:S128–S137, 2006.
- [143] I. Filella and J. Penuelas. Daily, weekly, and seasonal time courses of VOC concentrations in a semi-urban area near Barcelona. <u>Atmospheric</u> Environment, 40(40):7752–7769, 2006.
- [144] IUPAC Subcommittee on Gas Kinetic Data Evaluation Data Sheet HOx_VOC15 : $HO + CH_2 = C(CH_3)CHO \rightarrow products$. http://www.iupac-kinetic.ch.cam.ac.uk, 11th October 2005.
- [145] J.J. Orlando, G.S. Tyndall, and S.E. Paulson. Mechanism of the OH-initiated oxidation of methacrolein. Geophysical Research Letters, 26(14):2191–2194, 1999.
- [146] E.C. Tuazon and R. Atkinson. A product study of the gas-phase reaction of methacrolein with the OH radical in the presence of NO_x. <u>International</u> Journal of Chemical Kinetics, 22:591–602, 1990.
- [147] IUPAC Subcommittee on Gas Kinetic Data Evaluation Data Sheet P9: $CH_2=C(CH_3)CHO + h\nu \rightarrow products$. http://www.iupac-kinetic.ch.cam.ac.uk, 16th May 2002.
- [148] IUPAC Subcommittee on Gas Kinetic Data Evaluation Data Sheet $Ox_VOC9: O_3 + CH_2 = C(CH_3)CHO \rightarrow products.$ http://www.iupac-kinetic.ch.cam.ac.uk, 21th October 2002.
- [149] IUPAC Subcommittee on Gas Kinetic Data Evaluation Data Sheet NO3_VOC16: NO₃ + CH_2 = $C(CH_3)CHO \rightarrow products$. http://www.iupac-kinetic.ch.cam.ac.uk, 21th October 2002.
- [150] E.S.C. Kwok, S.M. Aschmann, J. Arey, and R. Atkinson. Product formation from the reaction of the NO₃ radical with isoprene and rate constants for the reactions of methacrolein and methyl vinyl ketone with the NO₃ radical. <u>International Journal of Chemical Kinetics</u>, 28(12):925–934, 1996.
- [151] A.A. Chew, R. Atkinson, and S.M. Aschmann. Kinetics of the gas-phase reactions of NO₃ radicals with a series of alcohols, glycol ethers, ethers and chloroalkenes. <u>Journal of the chemical Society Faraday Transactions</u>, 94:1083, 1998.
- [152] C.E. Canosa-Mas, S. Carr, M.D. King, D.E. Shallcross, K.C. Thompson, and R.P. Wayne. A kinetic study of the reactions of NO₃ with methyl vinyl ketone, methacrolein, acrolein, methyl acrylate and methyl methacrylate. Physical chemistry chemical physics, 1(18):4195–4202, 1999.

[153] W.H. Press, S.A. Teukolsky, W.T. Vetterling, and B.P. Flannery. Numerical Recipes in C, The Art of Scientific Computing. Cambirdge University Press, Cambridge, 2nd edition, 1992.

Danksagung

Bei Prof. Dr. Andreas Wahner möchte ich mich für die Betreuung der Arbeit und die am ICG 2 des Forschungszentrum Jülich zur Verfügung gestellte Möglichkeit bedanken, mit den benötigten Mitarbeitern und der nötigen Zeit an der SAPHIR Kammer meine Experimentvorschäge in die Tat umsetzen zu lassen.

Prof. Dr. Michael Kerschgens danke ich für die Übernahme des Koreferats. Meinem Betreuer Dr. Franz Rohrer möchte ich nicht nur für die jedes mal sehr fruchtbaren Diskussionen und Anregungen, die stark zum Gelingen dieser Arbeit beigetragen haben, besonders danken, sondern auch, zusammen mit Dr. Theo Brauers und Rolf Häseler für die Bedienung der Kammer und zusammen mit Peter Müsgen für die experimentellen NO_{x} und O_{3} Daten.

Für die tolle Zusammenarbeit während der SAPHIR Messkampagnen und das zur Verfügung Stellen weiterer experimenteller Daten möchte ich mich bedanken bei Dr. Hans-Peter Dorn und Dr. Eric Schlosser (DOAS, OH und HCHO), Rolf Häseler (LOPAP, HONO), Dr. Birger Bohn (SR, Photolysefrequenzen), Dr. Robert Wegener (Perkin-Elmer und Chrompack GC, VOCs und OVOCs), Ralf Tillmann (Hantzsch, HCHO und PTR-MS, VOCs) und Dr. Andreas Volz-Thomas, Norbert Houben, Marcel Berg und Hans-Werner Pätz (GC-ECD, PAN und MPAN).

Für die schnelle Hilfe bei Computerproblemen oder bei Installationswünschen möchte ich mich bei Helga London und Thomas Heil bedanken.

Klaus Peter Müller danke ich für das gute Klima in unserem Büro und Brigitte Berger für ihre Sorgfalt und die immer rechtzeitigen Hinweise auf Terminvorgaben von Formalitäten, die für Doktorandinnen am FZJ bestehen.

Meiner Fahrgemeinschaft danke ich nicht nur für die gesparten Fahrtkosten, sondern vor allem für die gute Unterhaltung.

Nicht zuletzt möchte ich mich bei meiner Familie und vor allem bei meinem Freund Ulrich Breidenbach für die Unterstützung, das Vertrauen, die benötigte Ablenkung und die Toleranz für eine Doktorandin in der Endphase bedanken.

Schriften des Forschungszentrums Jülich Reihe Energie & Umwelt / Energy & Environment

 Einsatz von multispektralen Satellitenbilddaten in der Wasserhaushaltsund Stoffstrommodellierung – dargestellt am Beispiel des Rureinzugsgebietes

von C. Montzka (2008), XX, 238 Seiten

ISBN: 978-3-89336-508-1

2. Ozone Production in the Atmosphere Simulation Chamber SAPHIR

by C. A. Richter (2008), XIV, 147 pages

ISBN: 978-3-89336-513-5

